Title
Flocks of Artificially Intelligent Swimming micro-Robots with Long-range Hydrodynamic Interaction and Objectives

Author
Mirzakhanloo, Mehdi

Publication Date
2020

Peer reviewed|Thesis/dissertation

Flocks of Artificially Intelligent Swimming micro-Robots with Long-range Hydrodynamic Interaction and Objectives

by

Mehdi Mirzakhanloo

A dissertation submitted in partial satisfaction of the

requirements for the degree of

Doctor of Philosophy

in

Engineering – Mechanical Engineering

in the

Graduate Division

of the

University of California, Berkeley

Committee in charge:

Professor Mohammad-Reza Alam, Chair
Professor Masayoshi Tomizuka
Professor Jon Wilkening

Fall 2020

Flocks of Artificially Intelligent Swimming micro-Robots
with Long-range Hydrodynamic Interaction and Objectives

Abstract

Flocks of Artificially Intelligent Swimming micro-Robots
with Long-range Hydrodynamic Interaction and Objectives

by

Mehdi Mirzakhanloo

Doctor of Philosophy in Engineering – Mechanical Engineering

University of California, Berkeley

Professor Mohammad-Reza Alam, Chair

This dissertation addresses various aspects of realizing a three-dimensional (3D) controlled flock of swimming micro-robots that operate in, and cooperatively influence, viscous fluid environments. A systematic approach is then presented to equip the agents with an adaptive decision-making intelligence, so as to enable flocks of these artificially intelligent swimming micro-robots to achieve various objectives in the presence of flow-mediated interactions.

In the first part of this dissertation, we introduce a versatile swimming robot with full 3D maneuverability in viscous environments. The experimental realization of this artificial low-Reynolds swimmer is then reported, and a hierarchical control strategy is implemented to perform various swimming maneuvers. The major challenge, which makes the swarm-control of swimming micro-robots substantially different from other well-studied swarms, is the presence of long-range flow-mediated (i.e. hydrodynamic) interactions. Therefore, the second part of this dissertation is devoted to the investigation of swarm hydrodynamics, including mutual interactions between these micro-swimmers, and their behavior in vicinity of solid boundaries. In particular, we unveil orbital topologies of interacting micro-swimmers, and report diverse families of attractors including dynamical equilibria, bound orbits, braids, and pursuit-evasion games. The third part of this dissertation is focused on optimal swarm-control strategies for swimming micro-robots to achieve various objectives in the presence of flow-mediated interactions. We show that micro-swimmers can form a concealed swarm through synergistic cooperation in suppressing one another's disturbing flows. Various control schemes are then demonstrated for the concealed swarming and stealthy maneuvers of swimming micro-robots. We also discuss how state-of-the-art reinforcement learning algorithms can be used to realize flocks of artificially intelligent swimming micro-robots. Specifically, a systematic approach is presented to equip the swimming micro-robots with an adaptive decision-making intelligence in response to non-linearly varying hydrodynamic loads. Flocks of these artificially intelligent micro-swimmers are then deployed to actively cloak swimming targets in a crowded environment. This study provides a road-map toward engineering cooperative flocks of smart micro-swimmers capable of accomplishing a new class of group-objectives. We, therefore, hope that it will spur further research on this field at the intersection of fluid mechanics, robotics and artificial intelligence.

Acknowledgments

My doctoral study at UC Berkeley has been a unique and unforgettable journey, and I owe it to my advisor, professors, colleagues, friends and family.

First and foremost, I would like to thank my incredible advisor, Professor Mohammad-Reza Alam, for his endless support throughout this journey. Reza is a true sample of a smart, insightful, and inspiring advisor who reshaped my perspective on scientific research. I am greatly indebted to Reza for teaching me how to always look for meaningful projects, giving me the courage to tackle hard problems, and helping me to become an independent researcher. I could not imagine having a better advisor and will be always grateful to him.

I would like to also express my sincere gratitude to the members of my dissertation committee, Professor Masayoshi Tomizuka and Professor Jon Wilkening, for generously offering their time, support, and good will throughout this journey. I was also fortunate to have Professor Tomizuka as the co-PI of my doctoral project, and I am thankful for his insightful suggestions and invaluable advice that helped shaping this research project.

This scientific journey was further enriched thanks to many others in the department of Mechanical Engineering, as well as Mathematics and Computer Science departments, at the University of California, Berkeley. Therefore, my gratitude further extends to Professor Stephen Morris, Professor James Sethian, and Professor Pieter Abbeel, for all that I learned from them. I am also thankful to Dr. Mir Abbas Jalali, and all other collaborators and friends in the Theoretical and Applied Fluid Dynamics laboratory. Many other thanks to all of my friends who made this journey an even more joyful experience.

I would like to dedicate this dissertation to my parents for their unconditional love, for their never-ending patience, understanding, and support. It is because of you that I have made it this far in life, and I will always be indebted to you. Thank you!

Contents

List of Figures

Chapter 1

Introduction

The science and engineering of multi-agent systems have significantly evolved over the past two decades in the communities of statistical physicists [e.g., 1], applied mathematicians [e.g., 2], and robotics engineers [e.g., 3, 4]. However, little is understood about how environmental disturbances induced by individual animals/robots (hereafter referred to as 'agents') affect their associates, preys or predators. For the agents swimming through fluid media, such environment-mediated interactions are known as *hydrodynamic* interactions, which have a long-range nature when viscous drags dominate inertial forces [5] – that is when the corresponding Reynolds number is small. Here we address various aspects of realizing a three-dimensional (3D) controlled flock of swimming micro-robots that operate in, and cooperatively influence, such viscous fluid environments.

The world of micro-scale swimming agents (hereafter referred to as 'micro-swimmers') is the one associated with low Reynolds condition ($\mathrm{Re} \ll 1$). Life in such viscosity dominated regimes is different from what has shaped our intuition [6]. In particular, dynamics of the incompressible flow around the agents swimming at low Reynolds is governed by the Stokes equation which has no explicit time-dependency [5]. This along with its linearity, makes the Stokes equation of motion invariant under time-reversal. As a result, body deformations (i.e. swimming strokes) that are reciprocal (i.e. invariant under time-reversal), can not generate a net propulsion at the Stokes regime – this is known as the *scallop* theorem [6]. Therefore, typical swimming strategies deployed by larger animals (such as fish, birds, or insects) are not effective at micro-scales. Motile microorganisms have evolved alternative propulsion mechanisms to break the time-symmetry, while retaining periodicity of their swimming strokes in time. These swimming strategies often exploit the drag anisotropy on a slender body in Stokes regime, and include the cork-screw propulsion of bacteria, the flexible-oar mechanism of spermatozoa, and the asymmetric beats of bi-flagellate algae [6].

Inspired by the propulsion strategies deployed by natural micro-swimmers, several design concepts have been proposed for *artificial* low-Reynolds-number swimmers, such as the multiple-link mechanisms [see e.g., 6], linked spheres [see e.g., 7], and the swimmers with helical propellers [see e.g., 8]. Among these systems, linked spheres are relatively hard to manufacture – especially the three-dimensional (3D) ones, because they need assemblies of

linear actuators with relatively long stroke lengths. Helical swimmers are the easiest to realize using 3D printers that use two-photon polymerization [9]. However, their locomotion strategy is restricted only to one degree of freedom, and this drastically limits their path planning. Multiple-linked mechanisms are relatively easy to fabricate and operate (as they need only rotary actuators), but their motion is confined to the planar (2D) space – as to the best of our knowledge, swimmers with 3D linkages have not been introduced.

In chapter 2 of this dissertation, we introduce a highly-controllable swimming robot (called 'Quadroar') with full 3D maneuverability at low Reynolds number regimes. This versatile swimming robot can be controlled to track any desired path in a 3D space, and can be used either as a biomedical swimming micro-robot in biological fluids or a mm-scale mobile robot performing inspection missions in highly viscous fluid environments. We then describe the swimmer's geometry and kinematics, followed by the mechatronic design and fabrication process of a mm-scale Quadroar. A supervisory control scheme is also presented in this chapter, to achieve an accurate trajectory tracking for swimmer's actuators and to realize various swimming maneuvers. A systematic experimental study is then conducted to evaluate the swimmer's performance and validate the behaviors predicted by our theoretical modeling. In particular, two primary modes of swimming – i.e. the forward translation and the planar reorientation modes – have been tested and compared with our numerical simulations. The results of this chapter were mainly presented in Ref. [10].

The major challenge, which makes the swarm-control for these swimming micro-robots substantially different from other well-studied swarms, is the presence of long-range flow-mediated (i.e. hydrodynamic) interactions. In fact, the motion of each swimming robot (in such low Reynolds number regimes) induces disturbing flows that strongly affect all nearby swimmers (even those many body lengths away), and thus alters dynamics of the entire system. Therefore, to control a collaborative flock of swimming micro-robots operating in realistic environmental/biological setups, one needs to have a clear understanding about: (i) the mutual hydrodynamic interactions between these micro-swimmers, and (ii) their behavior in vicinity of solid boundaries – that is significantly affected by the presence of swimmer-wall hydrodynamic interactions. Here, we will show rigorously that the presence of hydrodynamic interactions makes formulating the problem of locomotion, the group behavior of micro-swimmers and their active control a unique challenge.

In chapter 3, we unveil orbital topologies of interacting micro-swimmers using our artificial swimming micro-robot, i.e. the Quadroar. Depending on the initial conditions of the micro-swimmers, we find diverse families of attractors including dynamical equilibria, bound orbits, braids, and pursuit-evasion games. We show that two propelling micro-swimmers may fall into an equilibrium state at which they both remain stagnant indefinitely. This so-called 'dynamic equilibrium' is a result of hydrodynamic interactions between the two micro-swimmers, and is obtained through the formation of a nested saddle-shaped flow field near the swimmers. We also observe a hydrodynamic slingshot effect: a system of two hydrodynamically interacting micro-swimmers moving along 'braids' (i.e. tightly woven trajectories) can advance in space faster than non-interacting swimmers that have the same actuation parameters and initial conditions as the interacting ones. Our findings suggest

existence of complex collective behaviors of micro-swimmers, ranging from equilibrium to rapidly streaming states. The results of this chapter were mainly presented in Ref. [11].

In chapter 4, we investigate the behavior of our model micro-swimmer (whose flow field resembles that of the green algae, *Chlamydomonas reinhardtii*) near solid boundaries. In particular, we show that through hydrodynamic interaction, these micro-swimmers can feel and escape solid boundaries without the need for any physical contact with the wall. This finding is then further generalized, pointing out a hydrodynamic nature for the surface-scattering process of micro-swimmers with flow characteristics of bi-flagellate algae – i.e. those that induce an oscillatory flow field with anterior, side and posterior vortices. The results of this chapter were mainly presented in Ref. [12].

The rest of this dissertation is focused on optimal swarm-control strategies for swimming micro-robots to achieve various group objectives in the presence of flow-mediated interactions. As mentioned earlier, our findings in chapter 3 reveal that a pair of interacting micro-swimmers can boost each other's swimming speed while traveling through an ambient fluid. This phenomenon – termed as 'hydrodynamic slingshot effect' – implies that by forming a swarm, swimming micro-robots can collaborate and travel faster as a group than single individuals. An intriguing question is then whether by forming a swarm, micro-swimmers can be able to smartly cancel out each other's disturbing effects to the surrounding fluid environment. In other words, is it possible to form a stealth swarm minimally disturbing the ambient fluid? And if so, to what extent such cooperation between the agents can be effective in stifling the swarm's hydrodynamic signature? The answer will inspire an even more intriguing question, that is whether micro-swimmers can be actively cloaked, so as to remain undetectable (generating no trace) when passing through a host medium? Is there a way to realize an artificially intelligent flock of swimming micro-robots that not only can remain stealth, but also can be deployed to actively cloak randomly swimming targets?

In chapter 5, we show that micro-swimmers can form a *concealed* swarm through synergistic cooperation in suppressing one another's disturbing flows. We then demonstrate how such a concealed swarm can remain stealth while actively gathered around a favorite spot, pointing toward a target, or tracking a desired trajectory in space. Our findings provide a clear road map to control and lead flocks of swimming micro-robots in *stealth* versus *fast* modes, tuned through their active collaboration in minimally disturbing the host medium. The results of this chapter were mainly presented in Ref. [13].

In chapter 6, we demonstrate how state-of-the-art machine learning algorithms can be utilized to realize an artificially intelligent flock of swimming micro-robots. In particular, a systematic methodology is presented to actively cloak swimming objects within any arbitrarily crowded suspension of micro-swimmers. Our approach is to conceal the target swimmer throughout its motion using cooperative flocks of swimming agents equipped with adaptive decision-making intelligence. Through a reinforcement learning algorithm, the cloaking agents experientially learn an optimal adaptive behavior policy in the presence of flow-mediated interactions. This artificial intelligence enables them to dynamically adjust their swimming actions, so as to optimally form and robustly retain any desired arrangement around a moving object without disturbing it from its original path. Therefore, the

presented active cloaking approach not only is robust against disturbances, but also is non-invasive to motion of the cloaked object. We then further generalize the proposed approach and demonstrate how our cloaking agents can be readily used, in any region of interest, to realize hydrodynamic invisibility cloaks around any number of arbitrarily moving intruders. The results of this chapter were mainly presented in Ref. [14].

At the end, we summarize the main findings of this dissertation, discuss their potential impacts/applications, and provide concluding remarks in chapter 7.

Chapter 2

Quadroar: a Versatile Swimming micro-Robot with 3D Maneuverability

The motion of swimming micro-robots – similar to that of motile microorganisms such as bacteria or spermatozoa – is governed by different physical rules than what we experience in our day-to-day life. This is particularly due to the low-Reynolds-number condition of swimming at micro-meter scales. The *Quadroar*, a swimmer with three-dimensional maneuverability, is introduced for moving in these extreme conditions: either as a biomedical micro-robot swimming in biological fluids or a mm-scale swimming robot performing inspection missions in highly viscous fluid environments. In this chapter, we first briefly describe the Quadroar swimmer's geometry and kinematics. Then, the mechatronic design and fabrication of the mm-scale Quadroar is presented. In particular, we describe the design methodology and component selection of the system based on the required performance. A supervisory control scheme is also presented that is deployed to achieve an accurate trajectory tracking for all the swimmer's actuators. Finally, we conduct an experimental study to validate the predicted behaviors. In particular, the two primary modes of swimming – i.e. forward translation and planar reorientation – have been tested and compared with our theoretical model.

2.1 Introduction

Although the physical laws of motion are universally governed by Newton's equation, environment plays a crucial role in developing the locomotory functions of animals and organisms. Locomotion is a result of gaining reaction forces from an environmental entity by the continuous movements of body parts. In walking or running, a reaction force is generated at the contact point with ground by pushing the Earth backwards, while in swimming and flying, animals self-propel by displacing their environmental fluid. In all these known types of locomotion, the center of mass of the moving object and its environment remains at rest because there are no external forces involved. Although the flying of birds and swimming of fish involve periodic movements of their body parts, displacing the environmental fluid

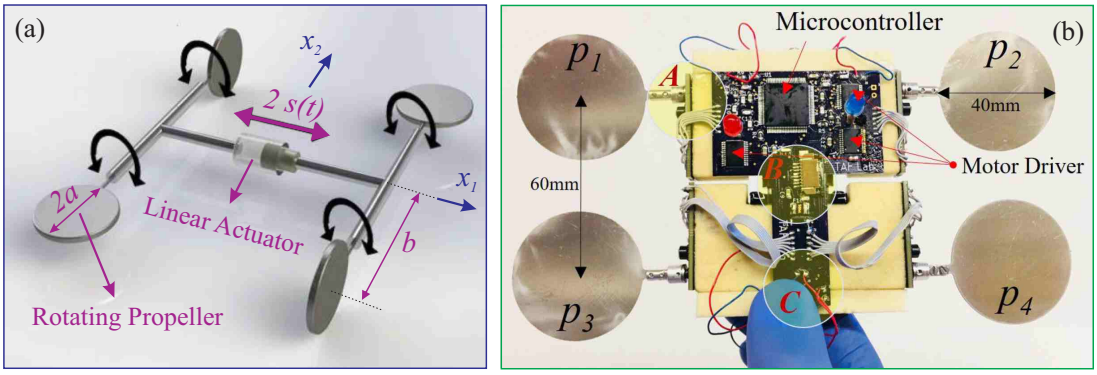

Figure 2.1: Schematic representation of the Quadroar swimmer (a) versus its mm-scale realization (b). The swimmer consists of four rotary disks (called the 'paddles'), and a linear actuator along its chassis. The expansion-contraction of the telescopic component in conjunction with the step-wise or continuous rotation of the paddles provides the swimmer with full 3D maneuverability, such that it can track any prescribed path in space.

becomes harder when viscous forces overwhelm inertial ones. Specifically, in the limit of zero Reynolds number ($\mathrm{Re} \ll 1$), when the motion of the background fluid is governed by the Stokes equation, reciprocal movements of the body parts will not propel the organism [6, 5]. The same problem exists for robotic swimmers in these extreme conditions.

Several designs can be found for artificial low-Reynolds-number swimmers in the literature: multiple-link mechanisms [e.g. 6], linked spheres [e.g. 7], swimmers with helical propellers [e.g. 8], and the Quadroar swimmer (Fig. 2.1) introduced by our team [e.g. 15, 10]. Among these systems, linked spheres are hard to manufacture (especially three-dimensional ones) because they need assemblies of linear actuators with relatively long stroke lengths. Helical swimmers are the easiest to realize using 3D printers that use two-photon polymerization [9], but they have only one degree of freedom, and thus path planning with internal control – as one may need to realize smart swarms [see e.g. 13, 14] – for them is not feasible. Multiple-linked mechanisms are relatively easy to manufacture and operate as they need only rotary actuators, but their motion is confined to 2D space – to the best of our knowledge, swimmers with 3D linkages have not been introduced.

One of the major advantages of the Quadroar as an artificial micro-swimmer is that it consists of rotary paddles and only one reciprocating actuator (see Fig. 2.1). This remarkably simplifies experimental realization of the Quadroar – as linear actuators (in all scales) are hard to fabricate and assemble. In nano-scales, the science and engineering of making molecular rotary units have leapt forward and claimed the Nobel prize in Chemistry in 2016 [16]. Molecular-scale linear actuators can also, in principle, be made of certain proteins [15]. The Quadroar is highly controllable and has full three-dimensional maneuverability. It can therefore track any prescribed spatial path [see e.g. 10]. This feature addresses some of the current challenges in the design of biomedical micro-robots [17], and thereby makes a sub-

millimeter-scale Quadroar a suitable candidate for various biological applications, such as drug delivery or autonomous surgery [18, 17]. The Quadroar swimmer can also be used as a model micro-swimmer to study the behavior of motile microorganisms (see e.g. chapters 3 and 4). In fact, even without actuating the chassis, the Quadroar swimmer can propel along an straight line and induce a flow structure [see e.g. 19, 11, 12] similar to that of green algae *Chlamydomonas reinhardtii*, which take breast strokes to swim. In macro scales, on the other hand, Quadroar swimmers can be deployed to perform autonomous robotic inspection missions in highly viscous fluid reservoirs [20] – such as oil tanks.

In this chapter, the Quadroar swimmer's geometry and kinematics is briefly introduced. We then report the design, fabrication and control of a mm-scale Quadroar. Finally, behavior of the experimentally realized prototype is studied for two primary modes of operation: (i) forward translation; and (ii) planar reorientation (see Fig. 2.2).

2.2 The Swimmer's Geometry and Kinematics

The Quadroar (*Quadru + oar*) swimmer consists of an I-shaped frame including two axles and a middle telescopic link as shown schematically in Fig. 2.1. Disks of radii a are placed at each end of the rear and front axles, and can rotate around their supporting flange link. Orientation of the i$^{\text{th}}$ propeller (i.e. the disk i$\in \{1, 2, 3, 4\}$) with respect to the main frame (or the swimmer's chassis) is denoted here by the angle variable ϑ_i, and the length of each axle is $2b$. The telescopic link (with a linear actuator in the middle) has a variable length $2l + 2s\,(t)$, where $s\,(t)$ is the contribution of the expansion/contraction of the linear actuator. At any given instant of time, the swimmer's orientation is quantified by the roll-pitch-yaw sequence of the Euler's angles ($\boldsymbol{\alpha}$), and its motion is tracked by the position of its geometric center, $\boldsymbol{X}_c$. Throughout the calculations presented in this chapter, a local frame of reference is considered with its origin fixed to the geometric center of the swimmer, so that the I-frame lies in the $x_1 - x_2$ plane, and x_1-axis is along the main link of the chassis (as shown in Fig. 2.1). We also consider a global stationary Cartesian coordinate system (X_i), which relates to the body-fixed local coordinates (x_i) through the rotation matrix ($\mathcal{R}$) defined based on the Euler's angles (ϕ, θ, ψ) representing the swimmer's orientation.

As a micro-robot swimming in biological fluids (or a mm-scale mobile robot performing inspection missions in highly viscous fluid environments), the Quadroar swimmer is a low-Reynolds-number swimmer (i.e. Re $\ll 1$). In the low-Reynolds regime, inertia is negligible and viscous drags primarily govern dynamics of the system. Therefore, hydrodynamics of these swimming micro-robots can be well-described by the Stokes equations,

$$\nabla P = \mu\, \nabla^2 \boldsymbol{u} + \boldsymbol{F}, \quad \nabla \cdot \boldsymbol{u} = 0, \tag{2.1}$$

subject to boundary conditions imposed by their swimming stroke. Here, μ is the dynamic viscosity of surrounding fluid, P denotes the pressure field, $\boldsymbol{u}$ is the velocity field, and $\boldsymbol{F}$ represents the external body force per unit volume.

In an otherwise stationary fluid of viscosity μ, the ith paddle (i.e. disk) of the swimmer experiences a drag force/torque while translating/rotating. These forces/torques depend on the dynamic viscosity (μ) of the ambient fluid, the disk geometry, and the linear/angular velocity of its motion – denoted by $\boldsymbol{v}_i$ and $\boldsymbol{\omega}_i$, respectively. The drag force and torque acting on the paddle i – which by the Newton's third law, cause reactions of the same magnitude from the paddle to ambient fluid – can be mathematically expressed as:

$$\boldsymbol{f}_i = \mu\ \mathscr{K}_i \cdot \boldsymbol{v}_i, \quad \boldsymbol{\tau}_i = \mu\ \mathscr{G} \cdot \boldsymbol{\omega}_i, \tag{2.2}$$

where all geometric properties of the disk are gathered in two tensors: (i) the translation tensor, $\mathscr{K}_i$, and (ii) the isotropic rotation tensor, $\mathscr{G}$, represented as [15]:

$$\mathscr{K}_i = \frac{8}{3}\ a \begin{bmatrix} 5-\cos(2\vartheta_i) & 0 & \sin(2\vartheta_i) \\ 0 & 4 & 0 \\ \sin(2\vartheta_i) & 0 & 5+\cos(2\vartheta_i) \end{bmatrix}, \quad \mathscr{G} = \frac{32}{3}a^3\boldsymbol{I}. \tag{2.3}$$

Note that $\boldsymbol{I}$ denotes the identity tensor. Here, for simplicity, we have assumed that paddles of the Quadroar swimmer are distant enough such that effects of the disturbing flows induced by other propellers can be neglected in calculating hydrodynamics of each single paddle. In chapters 3-4, we relax this assumption and consider the complete coupled hydrodynamic interactions between the swimmer's paddles. We also assume that cross section of the swimmer's I-frame is negligibly small compared to the effective area of its paddles, and thus drag forces on the swimmer's chassis are neglected. A self-propelled swimmer in Stokes regime is force-free and torque-free. Therefore, for a freely swimming Quadroar one must have

$$\sum_{i=1}^{4} \boldsymbol{f}_i = \mu \sum_{i=1}^{4} \mathscr{K}_i \cdot \boldsymbol{v}_i = 0 \tag{2.4}$$

$$\sum_{i=1}^{4} \boldsymbol{\tau}_i = \mu \sum_{i=1}^{4} \left(\mathscr{G} \cdot \boldsymbol{\omega}_i + \boldsymbol{r}_i \times \mathscr{K}_i \cdot \boldsymbol{v}_i\right) = 0, \tag{2.5}$$

where $\boldsymbol{r}_i = \pm\left[l + s(t)\right]\boldsymbol{e}_1 \pm b\boldsymbol{e}_2$ is the position vector of disk i with respect to the body-fixed frame of reference. Note that the linear and angular velocities of each disk (i.e. $\boldsymbol{v}_i$ and $\boldsymbol{\omega}_i$) in such a local frame of reference are calculated based on the velocity of the swimmer's center of mass, $\boldsymbol{V}_c$, and the angular velocity of its chassis, $\boldsymbol{\Omega}$. To be more specific:

$$\boldsymbol{v}_i = \mathcal{R}\boldsymbol{V}_c \pm \dot{s}(t)\boldsymbol{e}_1 + \boldsymbol{\Omega} \times \boldsymbol{r}_i, \quad \boldsymbol{\omega}_i = \boldsymbol{\Omega} + \dot{\vartheta}_i\boldsymbol{e}_2\ . \tag{2.6}$$

Therefore, the force- and torque-balance equations can be combined and expressed as

$$\begin{bmatrix} \mathscr{A}_{11} & \mathscr{A}_{12} \\ \mathscr{A}_{21} & \mathscr{A}_{22} \end{bmatrix} \begin{pmatrix} \boldsymbol{V}_c \\ \boldsymbol{\Omega} \end{pmatrix} = \begin{pmatrix} \mathscr{B}_1 \\ \mathscr{B}_2 \end{pmatrix}, \tag{2.7}$$

where components of the resistance matrices, $\mathscr{A}_{mn} = \mathcal{A}_{mn,jk}\ \boldsymbol{e}_j\boldsymbol{e}_k$ (m,n $\in \{1,2\}$), and elements of the forcing vectors, $\mathscr{B}_m = \mathcal{B}_{m,j}\boldsymbol{e}_j$ (m $\in \{1,2\}$), read as [see e.g. 15]

$$\mathscr{A}_{11} = \sum_{i=1}^{4} \mathscr{K}_i\mathcal{R}, \quad \mathcal{A}_{12,jk} = \sum_{i=1}^{4} \mathcal{K}_{i,jl} r_{i,p}\varepsilon_{plk},$$
$$\mathcal{A}_{21,jk} = \sum_{i=1}^{4} \varepsilon_{jpl} r_{i,p}\mathcal{K}_{i,lq}\mathcal{R}_{qk}, \quad \mathcal{A}_{22,jk} = \sum_{i=1}^{4} \left(\frac{32}{3}a^3\delta_{jk} + \varepsilon_{jpl}\varepsilon_{qkt} r_{i,p} r_{i,t}\mathcal{K}_{i,lq}\right),$$
$$\mathcal{B}_{1,j} = -\sum_{i=1}^{4} \mathcal{K}_{i,j1}\dot{l}_i, \quad \mathcal{B}_{2,j} = -\sum_{i=1}^{4} \left(\frac{32}{3}a^3\delta_{2j}\dot{\vartheta}_i + \dot{l}_i r_{i,k}\mathcal{K}_{i,l1}\varepsilon_{jkl}\right).$$

Here, $\mathscr{K}_i = \mathcal{K}_{jk}\ \boldsymbol{e}_j\boldsymbol{e}_k$ is the translation tensor (as defined in Eq. 2.3) corresponding to the paddle i, and $i \in \{1,2,3,4\}$ is the paddle indicator. Also, $\dot{l}_i = +\dot{s}(t)$ for $i \in \{1,2\}$ and $-\dot{s}(t)$ for $i \in \{3,4\}$. Note that Eq. 2.7 represents a set of non-linear ordinary differential equations, with parametric and external excitation. Once this non-linear system of equations is solved for $\boldsymbol{V}_c$ and $\boldsymbol{\Omega}$, one can track the position ($\boldsymbol{X}_c$) as well as the orientation ($\boldsymbol{\alpha}$) of the Quadroar swimmer (in time) by integrating

$$\dot{\boldsymbol{X}}_c = \boldsymbol{V}_c, \quad \dot{\boldsymbol{\alpha}} = T^{-1}\cdot\boldsymbol{\Omega}, \quad T = \begin{bmatrix} 1 & 0 & -\sin\theta \\ 0 & \cos\phi & \cos\theta\sin\phi \\ 0 & -\sin\phi & \cos\theta\cos\phi \end{bmatrix}. \tag{2.8}$$

In this chapter, we focus on the primary modes of propulsion (i.e. swimming strokes) in a planar space. Note that in a two-dimensional (2D) space, the forward translation combined with the ability to reorient (in-place) toward any desired direction, makes the swimming robot able to track any prescribed path. The sequences of step-wise control inputs (the so-called 'swimming cycles') which result in these two primary modes of planar motion are presented in Fig. 2.2. Specifically, harmonic oscillation of the linear actuator while keeping the rear disks normal (parallel) to the I-frame, and the front disks parallel (normal) to the I-frame, during the expansion (contraction), results in the 'forward translation' mode. A similar swimming cycle, except with disks $\{1,4\}$ normal (parallel) to, and disks $\{2,3\}$ parallel (normal) to the swimmer's I-frame during expansion (contraction), leads to the in-place counter-clockwise rotation of the swimmer, called the 'planar reorientation' mode. In general, behavior of the Quadroar swimmer is controlled by five control inputs: rotation rate of the four paddles and motion of the linear actuator. Through these five degrees of freedom, the swimming robot is able to move along transverse or forward straight lines, and can perform full re-orientation maneuvers about any of its body-fixed local axes [see 15, 11]. As a result, the swimmer has a full 3D maneuverability and is able to track any prescribed path in space by means of step-wise control strategies. This may potentially address some of the main challenges that biological micro-robots are facing today [17].

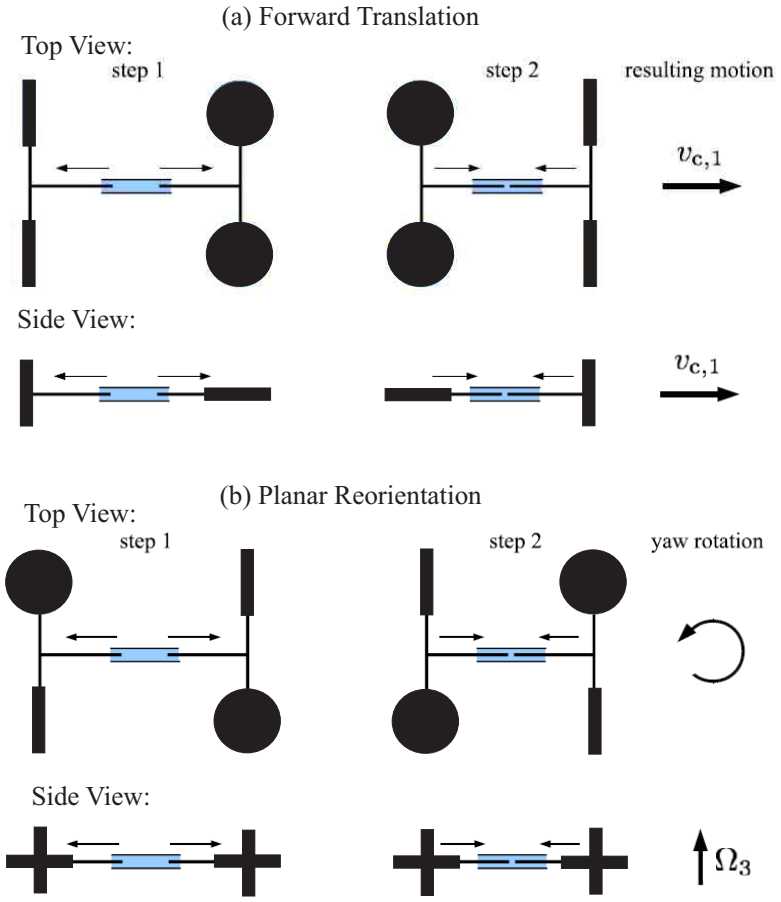

Figure 2.2: Schematic representation of stroke cycles leading to forward translation (a) and planar reorientation (b) of the Quadroar swimmer.

2.3 Experimental Realization of the mm-Scale Quadroar Swimmer

In this section, we report the designed and fabrication a mm-scale swimmer system according to the proposed Quadroar architecture. We then test it when swimming in the highly viscous silicone oil, so as to assure the low-Reynolds-number condition for such a mm-scale Quadroar. The swimmer system is composed of four rotary disks attached at the ends of its front and rear axles. These axles are located on a variable length chassis (see Fig. 2.3). Five mm-size brushed DC geared motors are used to spin the disks relative to the swimmer body, and to achieve linear expansion/contraction between the front and rear parts of the chassis. Additionally, a sensory system is used to measure the paddle angles and the chassis displacement to implement various modes of operation (i.e. 'swimming strokes'). An on-

board micro-controller is utilized to obtain trajectory tracking for all five actuators. In what follows, we briefly present the design and fabrication of the main mechanical and electrical components used in the Quadroar swimmer system.

2.3.1 Main Body and Chassis

The main body of the swimmer consists of two rectangular-shape sections (front and rear). Since most of the components installed on the swimmer (such as DC motors, magnetic encoders, lead-screw mechanism, etc.) have a density higher than that of silicone oil, a low-density machinable foam with a density of about 0.2 gr/cm^3 is used to fabricate the body of the swimmer. The net density of the fabricated Quadroar swimmer is approximately 0.95 gr/cm^3, suitable for submerging in the silicone oil. A lead-screw mechanism with two guide rails, as well as a small geared DC motor to turn the lead-screw, are deployed to achieve linear expansion/contraction between the front and rear sections (see Fig. 2.3).

2.3.2 Motors and Motor Drivers

In Stokes regimes, the required torque τ_{max} to turn a thin circular disk of radius a in an otherwise stationary ambient fluid with dynamic viscosity of μ can be calculated as $\tau_{max} = 6\mu a^3\omega$ [5], where ω is the angular velocity of the disk. Based on this estimation, in order to achieve a maximum angular speed of 25 rad/s, for a thin disk of diameter 4 cm, in a liquid with dynamic viscosity of 5000 cP, one needs a 6 N.mm torque. Considering this maximum required torque as well as other practical complexities in driving [1], cost and compactness, a geared DC motor is selected (see Fig. 2.3) which has a 6 mm diameter, 19 mm length and can provide 6 N.mm torque consuming 180 mA at 5V.

Three dual H-bridge DC motor controllers (TB6612FNG from Toshiba) are also used to control these motors in both directions. Each driver works with a 5V electric power supply, and is capable of applying a maximum continuous current up to 1.2A. Motor angular speed can be controlled through a pulse width modulation (PWM) signal where the duty ratio determines the angular speed of the motor.

2.3.3 Sensory System

Accurate tracking of the angular position of the swimmer paddles, as well as the phase lag between these paddles and the chassis' expansion/contraction, is crucial for the Quadroar swimmer to perform various modes of propulsion (i.e. swimming strokes) through the ambient fluid. Therefore, an effective sensory system is necessary to measure the relative angles between each paddle and the swimmer's body, as well as the chassis' expansion length. Here, we used the AS5048A rotary magnetic encoder chip (see Fig. 2.3), which consists of four

[1]For example, brush-less DC motors require a complex driver system while brushed DC motors can be driven simply by applying a voltage difference.

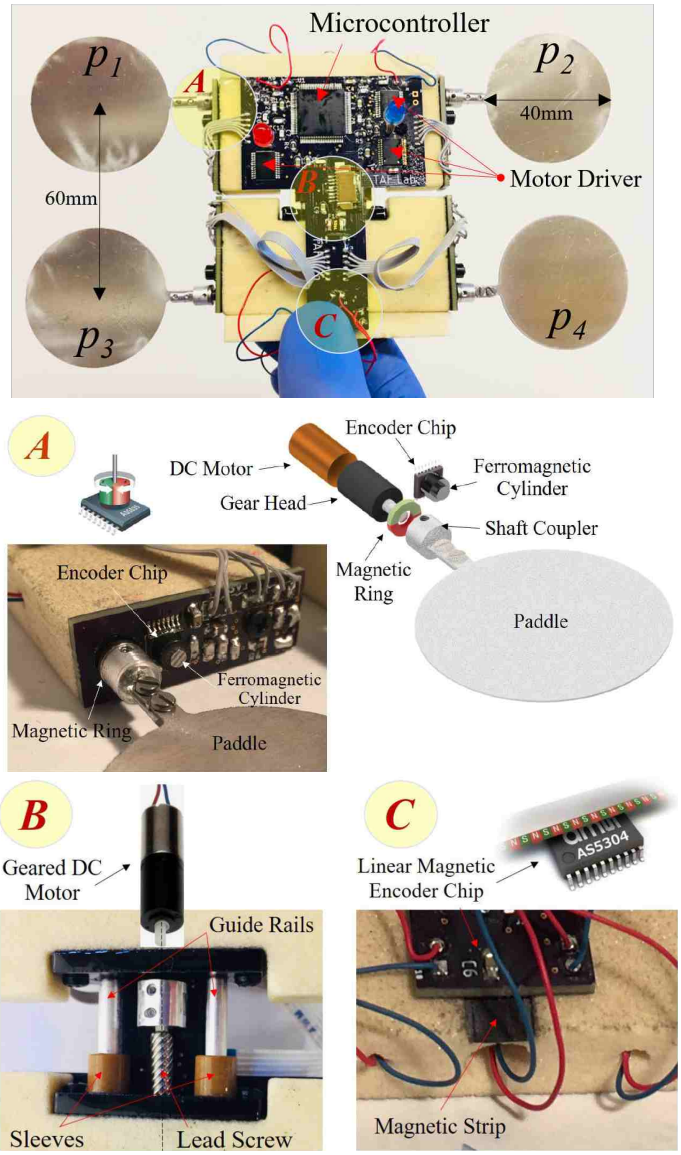

Figure 2.3: The mm-scale realization of the Quadroar swimmer for viscous environments. A) The angle measurement system: a magnetic encoder is used to measure the paddles' angles. A ring magnet is attached to the paddle shaft, so as to induce a magnetic field in the ferromagnetic cylinder which is installed on top of the magnetic encoder chip. B) The linear actuator as an expansion/contraction mechanism: a lead-screw mechanism is used to generate the expansion/contraction motion between the front and rear sections of the swimmer. C) The expansion/contraction measurement system.

Hall effect sensors located at its corners, and measures the absolute position of the magnet's rotation angle. This magnetic encoder has a resolution of 14 bit per revolution (i.e. 0.02 degree) and benefits from a small package size ($4 \times 6 \times 1$ mm).

To measure the paddle angle, a magnetic ring (to be radially magnetized) needs to be attached to the paddle shaft while the encoder chip is in front of, and centered with, the ring. However, in our swimmer system, it is not possible to attach a magnetic ring to the paddle shaft ends such that it faces the encoder chip. Therefore, the chip has to be placed with an offset (of 8 mm) from the ring (see Fig. 2.3). Such an offset, in turn, will disable the encoder from measuring the correct angle of the paddle. To circumvent this practical issue, a small ferromagnetic cylinder is attached to the encoder chip, so that the magnetic ring on the paddle shaft induces a magnetic field inside the cylinder. While the paddle shaft and magnetic ring combination is being turned, the magnetic encoder chip can then indirectly estimate the paddle angle by measuring the induced field in the ferromagnetic cylinder.

Similarly, a combination of a linear magnetic encoder (AS5304) and a multi-pole magnetic strip is used to measure the expansion/contraction of the chassis (see Fig. 2.3). The linear magnetic encoder is installed on the rear section of the chassis, while the magnetic strip is attached to the front one. Expansion/contraction of the chassis generates a square wave pulse. By counting the number of pulses with the on-board micro-controller, the instantaneous length of the chassis can be measured. Considering the linear magnetic encoder resolution (160 pulses per pole pair interval) and the pole interval on the magnetic strip (4 mm), the resolution of the chassis expansion measurement is equal to 0.025 mm.

2.3.4 Micro-Controller

An on-board micro-controller is used to perform low-level control algorithms, calculate the command signals for the actuators, and measure the sensory values. Considering factors including the number of I/O ports necessary for the system, as well as processor speed and availability, the Atmega 2560 (from Atmel) is selected for on-board control of the Quadroar swimmer. It has an 8-bit processor and can run with a maximum clock frequency of 16 MHz. A unique board is designed and fabricated for installing this micro-controller as well as other electronic components such as motor drivers, voltage regulators and linear encoders. The fully assembled micro-swimmer system is shown in Fig. 2.3.

2.4 Hierarchical Control Strategy

The sampling rate between the micro-controller and sensors/actuators is more than 300 Hz, while the communication rate between the micro-controller and the computer (attached via USB cable) is only 50 Hz. Therefore, a hierarchical control scheme (c.f. [21]) is used here to improve the performance of the trajectory tracking (see Fig. 2.4). The two-level control structure introduced in this chapter, includes a multi-rate system with the higher level controller (i.e. Simulink) updating the reference signal at 50 Hz, and the lower level

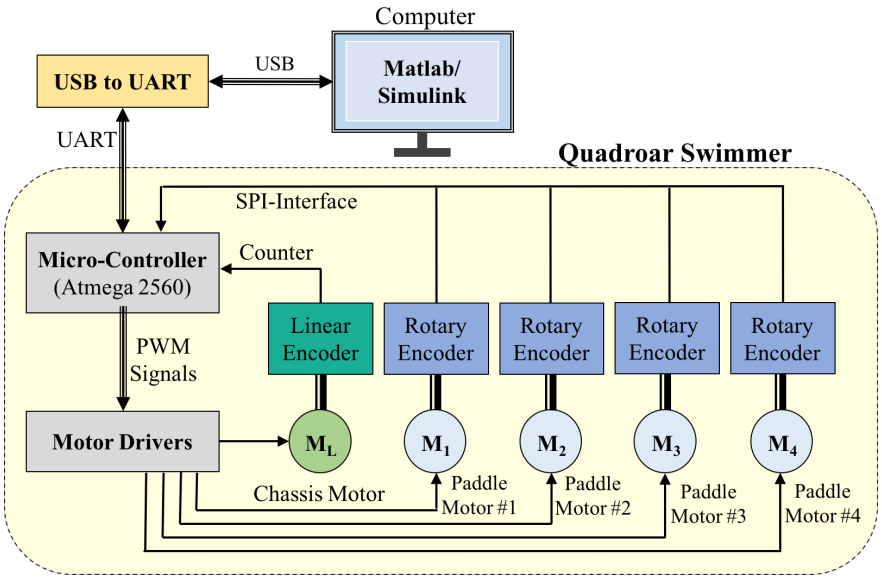

Figure 2.4: Block diagram presenting interconnections between different components of the swimmer system. A two-level control strategy is used where the sampling rate between the micro-controller and sensors/actuators is more than 300 Hz, while the communication rate between the micro-controller and the computer (attached via USB cable) is only 50 Hz.

controller (i.e. on-board micro-controller) closing the loop at 300 Hz [22]. This control architecture further improves the system performance through a fast and accurate tracking of the paddle angles and chassis expansion/contraction.

The low-level controller is composed of a feedback and a feed-forward loop. The feed-forward portion is obtained by an open-loop calibration test that is performed on each motor individually. The calibration is mainly done to find and remove the dead-zone in the motor control command. It is also needed to find a linear input/output model for each actuator. The feedback portion is a proportional–integral–derivative (PID) controller that has been tuned based on the motor model, as well as the hydrodynamic interaction between the paddles rotating in the ambient fluid. The performance of this controller for trajectory tracking (here a square wave) is shown in Fig. 2.5 for a sample case. This two-level control scheme is then implemented on the swimmer to test various modes of operation in silicone oil where each mode is composed of a unique sequence of paddles/chassis actuation profile. The results of these experimental tests are presented in the next section.

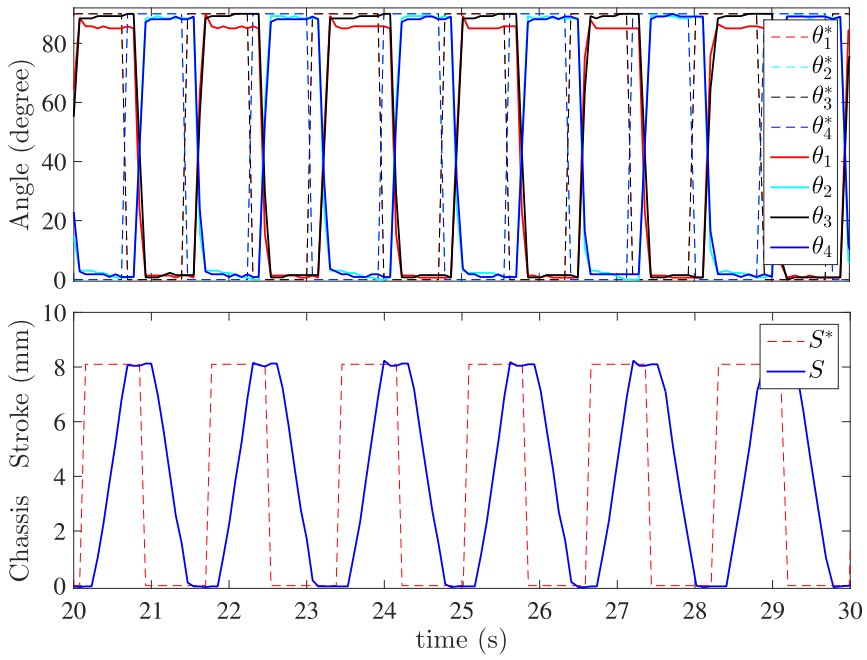

Figure 2.5: Trajectory tracking by paddles and the chassis, for a benchmark test case of square wave signals. Here the paddles rotate between 0 and 90^o, while the chassis expands/contracts between 0 and 8.1 mm.

2.5 Experimental Results and Discussion

After identifying and resolving minor mechanical and electrical issues in the system, the Quadroar swimmer is submerged and tested in a tank of silicone oil. Experimental sample tests for the two primary modes (i.e. the forward translation and the planar reorientation) have been conducted (see e.g. Fig. 2.6), and the dynamic behavior of the swimmer system is compared (Fig. 2.7) to that predicted by the theoretical model developed in section 2.2.

As a benchmark, snapshots of the forward translation experiment are shown in Fig. 2.6, where red and blue LEDs are used on the swimmer to enable us determining its position and orientation in the tank through the video processing toolbox in MATLAB. A sequence of paddles' angles and chassis' stroke similar to that presented in Fig. 2.2 is applied on the swimmer to achieve translation and reorientation motions. The Reynolds number corresponding to these test cases can be calculated as $Re = \rho v D/\mu$, where ρ and μ are the density and dynamic viscosity of the surrounding fluid (here 1000 Kg/m^3 and 5000 cP, respectively); v is the maximum chassis expansion/contraction speed (here 10.5 mm/s); and D is the paddle diameter (here 40 mm). Therefore, the Reynolds number corresponding to these experiments is ~ 0.1, which matches our assumption for low-Reynolds-number condition (i.e. $Re \ll 1$). The results of these two tests are then compared (in Fig. 2.7) with

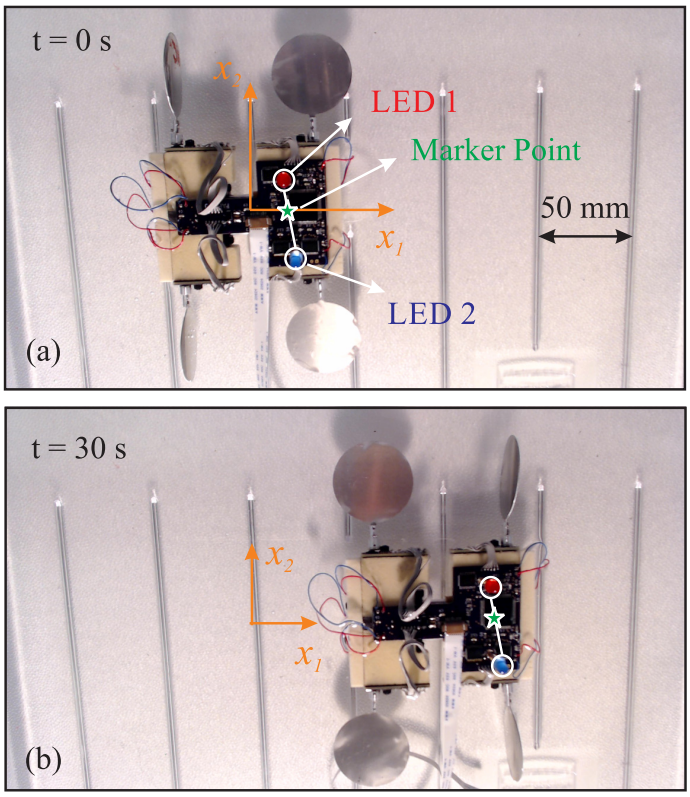

Figure 2.6: The Quadroar swimmer performing the swimming stroke that generates forward translation (see Fig. 2.2a) in the silicone oil tank. Two LEDs are placed on the swimmer chassis, so as to precisely track the location and orientation of the swimmer through video processing. The stroke and linear velocity of the chassis' expansion/contraction (in the presented test case) are 21.6 mm and 10.5 mm/s, respectively.

those achieved by our simplified theoretical model. The experimental results match well with the theoretical prediction for both the forward translation and planar reorientation modes. The slight difference between the experimental and theoretical results can mainly be due to neglecting the following factors in the theoretical model: (i) the swimmer's actual frame size which generates additional drag force on the body; (ii) effects of the tank's confining walls and bottom surface (c.f. chapter 4); and (iii) the tension generated in the data/power cable connected to the actual fabricated swimmer.

More experimental tests have also been performed to further investigate the effects of chassis stroke on forward translation and planar reorientation. Specifically, three different chassis strokes are used for each mode of operation: 8.1, 13.5 and 21.6 mm. As shown in Fig. 2.7, the chassis stroke does not affect the average linear velocity of the swimmer. This is also in agreement with our theoretical prediction, which shows that the swimmer linear speed only depends on the chassis expansion/contraction rate (i.e. speed), but not its stroke. In

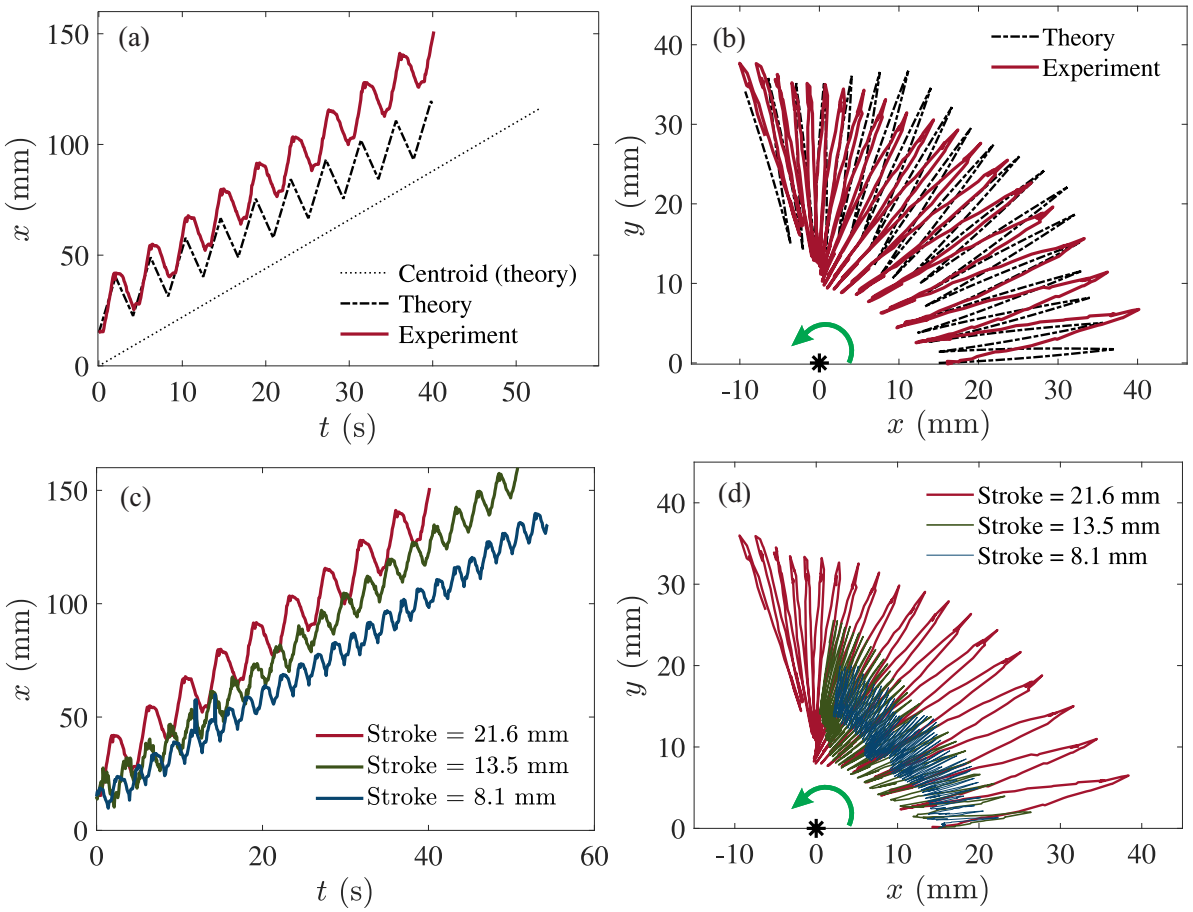

Figure 2.7: (a)-(b): Comparison between the behavior predicted by our simplified theoretical model and the experimental results obtained for sample tests conducted on the forward translation (a) and the planar reorientation (b) modes. Solid and dashed lines represent trace of the marker on the swimmer in experiments and theoretical modeling, respectively. Theoretical position of the centroid in panel (b) is shown by an asterisk, and the green arrow shows direction of the performed reorientation. For the benchmark test presented in panels (a) and (b), the stroke and linear velocity of chassis' expansion/contraction are 21.6 mm and 10.5 mm/s, respectively. We also further explore experimental results for the forward translation (c) and the planar reorientation (d) modes, when the swimmer uses various strokes. The Quadroar swimmer is translating forward along x_1 direction (c.f. Fig. 2.2a) in panel (c); and it is reorienting counter-clockwise in $x_1 - x_2$ plane (c.f. Fig. 2.2b) in panel (d). Solid lines represent trace of the marker on the Quadroar swimmer (see Fig. 2.6).

planar reorientation, note that the presented trajectories belong to the marker point (Fig. 2.6), since motion of the swimmer's centroid is negligible in our experiments – that is the in-place reorientation as predicted by our theoretical model.

The promising match observed between predicted behaviors and the experimental results, opens up a new avenue toward designing more advanced control algorithms to obtain complex trajectory tracking in real time. This is the main topic of our future work, where we will design and implement a passive velocity field control (PVFC) algorithm to navigate the Quadroar swimmer along any prescribed trajectory through a viscous fluid environment with several solid obstacles to be avoided.

2.6 Concluding Remarks

In this chapter, we reported the design, fabrication, control strategy, and experimental testing of the first swimming robot with full 3D maneuverability in viscous environments. This low-Reynolds-number swimmer (called Quadroar) is composed of four independent rotary paddles and a chassis capable of expanding and contracting. The swimmer body is made with a machinable foam to make it neutrally buoyant in the ambient fluid (here e.g. silicone oil). A two-level supervisory control scheme was designed and implemented on the swimmer to perform two primary modes of propulsion (i.e. swimming strokes), namely the forward translation and planar reorientation. The supervisory controller (i.e. the computer/Simulink) provides high-level commands by calculating the sequence of paddles' angles and chassis expansion/contraction mode, so as to obtain the desired motion. The on-board micro-controller, on the other hand, implements feedback algorithms to track such angles and strokes by the paddles and chassis, respectively.

Performance of the mm-scale Quadroar swimmer has then been experimentally evaluated in silicone oil, where it satisfies the low-Reynolds-number condition (Re ~ 0.1). The two primary modes of propulsion – i.e. the forward translation and the planar reorientation – have been tested and compared with our theoretical models. Experimental results match well with the behavior predicted theoretically. Nevertheless, some minor deviations were observed due to factors such as non-negligible drag force on the chassis, hydrodynamic interactions with solid boundaries, and tension in the data/power cable, which were not considered in the simplified theoretical model. Potential future steps include the design and implementation of a passive velocity field control (PVFC) algorithm to navigate the swimming robot along a predefined trajectory such that it avoids solid obstacles on its motion path.

Acknowledgments

This work is supported by the National Science Foundation grant CMMI-1562871.

Chapter 3

Mutual Interactions and Hydrodynamic Choreographies

In this chapter, we unveil orbital topologies of interacting micro-swimmers using an artificial swimming micro-robot, called *Quadroar*. Depending on the initial conditions of the micro-swimmers, we find diverse families of attractors including dynamical equilibria, bound orbits, braids, and pursuit–evasion games. We also observe a hydrodynamic slingshot effect: a system of two hydrodynamically interacting swimmers moving along braids can advance in space faster than non-interacting swimmers that have the same actuation parameters and initial conditions as the interacting ones. Our findings suggest existence of complex collective behaviors of micro-swimmers, ranging from equilibrium to rapidly streaming states.

3.1 Introduction

Natural micro-swimmers (known as 'microorganisms') including all species of bacteria, protozoa, and also some of algae, are playing an important role in recycling nutrients in the earth's ecosystems [23, 24]. A recent report by National Science Foundation (NSF) estimates the presence of about one trillion species right now on the earth, that only one-thousandth of one percent of which have been studied [25]. This fact has put the investigation of natural, as well as artificial, micro-swimmers under the spotlight [26].

Swimming microorganisms in nature nearly always come in groups, and understanding their collective behaviors in the presence of hydrodynamic interactions requires multi-scale models [27, 28]. The main challenge in developing statistical and continuum models is how we deal with collisional and relaxation processes, which are basically determined by two-body interactions [29]. This is exacerbated by the long range nature of hydrodynamic interactions at low Reynolds number conditions that makes the investigation of the swarm dynamics of micro-swimmers substantially different from other well-studied swarms. Specifically, swimmers at small scales strongly affect (at distances several body-length away) their fluidic environment and hence their nearby swimmers (compare this with, say, Quadcopters whose

influence on nearby copters is limited to a fraction of their body length). An interesting example, showing the significance of hydrodynamic interactions, is that they may trigger the locomotion of otherwise non-swimming reciprocal swimmers [30, 31].

Prior observations have revealed a glimpse of complex behaviors emerged from hydrodynamic interactions. For instance, the parallel motion of two flagella-driven bacteria have been shown to be unstable [32], two nematodes tied to a wall from one end eventually get entangled [33], and two Paramecia avoid each other solely due to hydrodynamic interactions [34]. To addressed two-body dynamics for micro-scale swimmers, several studies have proposed using simple minimal model swimmers and have been able to report few basic behaviors. For example, two puller-type squirmers are shown to experience a significant change in their orientations after an encounter [35], which together with the swimmers' inertial effects, causes hydrodynamic attraction [36]. For spherical swimmers with spatially confined circular trajectories, the reported long-time cell-cell interaction is either an attraction or a repulsion [37], whereas two rigid helices are shown not to attract or repel each other while rotating in-phase [38]. Another example is a system of two linked-sphere swimmers [7] that may converge, diverge oscillate or stay parallel to each other [39].

Recent experiments, nevertheless, uncover more complex flow fields around flagellated microorganisms [40]. Specifically, flagellated microorganisms such as *Chlamydomonas reinhardtii* induce an oscillatory flow field that alternates between the flow fields of basic puller- and pusher-type swimmers [41, 40], complicating the nature of two- or multi-body interactions of such microorganisms. To gain insight into the two- and three-dimensional interactions of microorganisms, we simulate them using the Quadroar swimmer whose flow field [19] is similar to that of *C. reinhardtii* [41]. One of the major advantages of the Quadroar as an artificial micro-swimmer is that it consists of rotary disks and only one reciprocating actuator. This remarkably simplifies the realization of the Quadroar as linear actuators (in all scales) are hard to fabricate and assemble. In nano-scales, the science and engineering of making molecular rotary units have leapt forward and claimed the Nobel prize in Chemistry in 2016 [16], and molecular-scale linear actuators can, in principle, be made of certain proteins [15]. The Quadroar is highly controllable and has full three-dimensional maneuverability. It can therefore track any prescribed spatial path [15]. This has been a challenge in the design of medical micro-robots [17] that makes a sub-millimeter-scale Quadroar also a suitable candidate for various biological applications, such as drug delivery or autonomous surgery [18, 17]. In macro scales, the Quadroar can be deployed as a robotic swimmer for inspection missions in highly viscous fluid reservoirs [20].

In this chapter, we use the Quadroar swimmer to unveil the rich two-body dynamics associated with hydrodynamic interactions of two micro-swimmers in the Stokes regime. Unlike other existing theoretical models that try to simulate the swimming mechanism of specific microorganisms [see e.g. 42], the Quadroar is designed to induce an oscillatory flow field with anterior, side and posterior vortices in its surrounding [19]. Therefore, complex interactions that we find in the phase-space of two swimmers are generic characteristics of microorganisms generating anterior, side and posterior vortices.

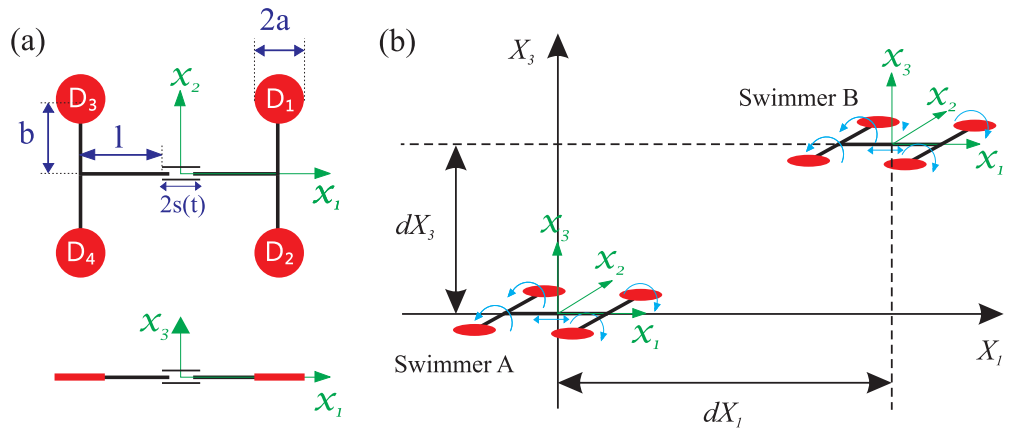

Figure 3.1: Quadroar, a swimming micro-robot whose induced flow field resembles that of the green algae *C. reinhardtii*. (a) Geometry of the Quadroar swimmer. (b) Relative initial positions of two planar swimmers considered in this study.

3.2 Kinematics and Numerical Framework

The Quadroar consists of an I-shaped frame including an active chassis and two axles of length $2b$ (see Figure 3.1). Each axle (at its two ends) is connected to two disks of radii a. The length of the chassis is variable and is equal to $2l + 2s(t)$ where $s(t)$ is the contribution from the expansion/contraction of a linear actuator installed in the middle of the chassis. The angular position of each disk D_n $(n = 1, \ldots, 4)$ with respect to the leg of its axle is denoted by $-\pi \leq \vartheta_n \leq \pi$. We define a body-fixed Cartesian coordinate system (x_1, x_2, x_3) with its origin at the geometrical center of the frame. The (x_1, x_2)-plane lies in the plane of the swimmer and the x_1-axis is along the chassis. We also define a global Cartesian coordinate system (X_1, X_2, X_3) as is shown in Figure 3.1(b). The body-fixed coordinates x_i are related to the global coordinates X_i $(i = 1, 2, 3)$ through a transformation matrix $\boldsymbol{R}$ that depends on three orientation (Euler's) angles of the swimmer.

We assume that the influence of each disk on its surrounding environment can be modeled as a point force and a point torque [43]. For each of the two swimmers, $j = A, B$, and for each of their four disks $n = 1, \cdots, 4$, the point forces $(\boldsymbol{f}_{jn})$ and torques $(\boldsymbol{\tau}_{jn})$, expressed in the global coordinate frame are given by [19]

$$\boldsymbol{f}_{jn} = \mu \boldsymbol{R}_j^T \cdot \boldsymbol{K}_{jn} \cdot \boldsymbol{R}_j \cdot (\boldsymbol{v}_{j,c} + \boldsymbol{v}_{jn} - \boldsymbol{u}_{jn}) \,, \tag{3.1}$$

$$\boldsymbol{\tau}_{jn} = \mu \mathbf{G} \cdot (\boldsymbol{\omega}_{j,\text{body}} + \boldsymbol{\omega}_{jn} - \boldsymbol{\Omega}_{jn}) \,, \tag{3.2}$$

where μ denotes dynamic viscosity of the surrounding fluid; $\boldsymbol{v}_{jn}$ and $\boldsymbol{\omega}_{jn}$ are the linear and angular velocities of each disk with respect to the swimmer's hydrodynamic center and body-fixed coordinate frame, respectively; $\boldsymbol{v}_{j,c}$ is the absolute velocity of the hydrodynamic center and $\boldsymbol{\omega}_{j,\text{body}}$ is the angular velocity of the jth swimmer expressed in terms of Euler's angles;

$\boldsymbol{u}_{jn}$ and $2\boldsymbol{\Omega}_{jn}$ are the velocity and vorticity fields of the fluid at the center of each disk; $\boldsymbol{G}$ is the isotropic rotation tensor and $\boldsymbol{K}_{jn}$ is the translation tensor corresponding to disk n of swimmer j. These tensors are mathematically defined as [15]:

$$\mathbf{G} = \frac{32}{3}a^3\boldsymbol{I}, \quad \boldsymbol{K}_{jn} = \frac{8}{3}a\begin{bmatrix} 5-cos\left(2\vartheta_{jn}\right) & 0 & sin\left(2\vartheta_{jn}\right) \\ 0 & 4 & 0 \\ sin\left(2\vartheta_{jn}\right) & 0 & 5+cos\left(2\vartheta_{jn}\right) \end{bmatrix}. \tag{3.3}$$

A self-propelled swimmer in the Stokes regime is force-free and torque-free. Therefore,

$$\sum_{n=1}^{4}\boldsymbol{f}_{jn} = 0, \quad \sum_{n=1}^{4}\left[\left(\boldsymbol{R}_j^T\cdot\boldsymbol{r}_{jn}\right)\times\boldsymbol{f}_{jn}+\boldsymbol{\tau}_{jn}\right] = 0, \tag{3.4}$$

for swimmers $j = A, B$. These four sets of vectorial equations (i.e. a set of two vectorial equations for each of the swimmers) require the values of velocities $\boldsymbol{u}_{jn}$ and spins $\boldsymbol{\Omega}_{jn}$ (at the position of disk n of swimmer j) to be complete and solvable for $\boldsymbol{v}_c$ and $\boldsymbol{\omega}_{\text{body}}$. Considering only the point-force contribution of each propeller in an infinite fluid domain, the Stokes equation describing dynamics of the induced flow can be written as:

$$\nabla P = \eta\,\nabla^2\boldsymbol{u} + \boldsymbol{f}\delta(\boldsymbol{r}), \quad \nabla\cdot\boldsymbol{u} = 0, \tag{3.5}$$

where $\delta\left(\boldsymbol{r}\right)$ is Dirac delta function. The point-force is exerted at $\boldsymbol{x}_0$, and for a generic point $\boldsymbol{x}$ in space $\boldsymbol{r} = \boldsymbol{x} - \boldsymbol{x}_0$ with $r = |\boldsymbol{r}|$. Equation (3.5) can be analytically solved in several ways [see e.g. 44], and the resultant velocity field is known as Stokeslet:

$$\boldsymbol{u}\left(\boldsymbol{r},t\right) = \frac{\boldsymbol{f}}{8\pi\eta}\cdot\left(\frac{\boldsymbol{I}}{r}+\frac{\boldsymbol{r}\boldsymbol{r}}{r^3}\right). \tag{3.6}$$

The contribution of a point-torque $\boldsymbol{\gamma}$ exerted at a point $\boldsymbol{x}_0$ in an infinite fluid, on the other hand, is derived from the following set of equations [44]:

$$\nabla P = \eta\,\nabla^2\boldsymbol{u} + \nabla\times\left(\boldsymbol{\gamma}\delta(\boldsymbol{r})\right), \quad \nabla\cdot\boldsymbol{u} = 0. \tag{3.7}$$

The exact solution to Eq. (3.7) is also available [see e.g. 44], and is called a rotlet:

$$\boldsymbol{u}\left(\boldsymbol{r},t\right) = \frac{1}{8\pi\eta}\left(\frac{\boldsymbol{\gamma}\times\boldsymbol{r}}{r^3}\right). \tag{3.8}$$

In the case of two interacting swimmers, the linear nature of the Stokes equation then allows us to invoke superposition and obtain:

$$\begin{aligned}\boldsymbol{u}_{jn} = \frac{1}{c_0}\sum_{k=1,k\neq n}^{4}&\left(\frac{\boldsymbol{f}_{jk}}{z_{kn,j}}+\frac{\boldsymbol{f}_{jk}\cdot\boldsymbol{X}_{kn,j}}{z_{kn,j}^3}\boldsymbol{X}_{kn,j}+\frac{\boldsymbol{\tau}_{jk}\times\boldsymbol{X}_{kn,j}}{z_{kn,j}^3}\right)\\ +\frac{1}{c_0}\sum_{k=1}^{4}&\left(\frac{\boldsymbol{f}_{ik}}{z_{kn,ij}}+\frac{\boldsymbol{f}_{ik}\cdot\boldsymbol{X}_{kn,ij}}{z_{kn,ij}^3}\boldsymbol{X}_{kn,ij}+\frac{\boldsymbol{\tau}_{ik}\times\boldsymbol{X}_{kn,ij}}{z_{kn,ij}^3}\right),\end{aligned} \tag{3.9}$$

and

$$2\boldsymbol{\Omega}_{jn} = \boldsymbol{\nabla} \times \boldsymbol{u}_{jn}, \tag{3.10}$$

where $c_0 = 8\pi\mu$, and

$$\boldsymbol{X}_{kn,j} = \boldsymbol{R}_j^T \cdot (\boldsymbol{r}_{jn} - \boldsymbol{r}_{jk}), \tag{3.11}$$

$$\boldsymbol{X}_{kn,ij} = (\boldsymbol{X}_{c,j} + \boldsymbol{R}_j^T \cdot \boldsymbol{r}_{jn}) - (\boldsymbol{X}_{c,i} + \boldsymbol{R}_i^T \cdot \boldsymbol{r}_{ik}). \tag{3.12}$$

The scalars $z_{kn,j}$ and $z_{kn,ij}$ are the magnitudes of the vectors $\boldsymbol{X}_{kn,j}$ and $\boldsymbol{X}_{kn,ij}$, respectively, and $\boldsymbol{r}_{jn}$ denotes the position vector of the nth disk in the swimmer j's local coordinate frame. In all expressions we have $i, j = A, B$ with the condition $i \neq j$ in each expression.

In this chapter, we also assume that disks D_n $(n = 1, \ldots, 4)$, of each swimmer $j = A, B$ are spinning with angular velocities $\dot{\vartheta}_{j1} = \dot{\vartheta}_{j2} = c_0\ \omega_s$ and $\dot{\vartheta}_{j3} = \dot{\vartheta}_{j4} = -c_0\ \omega_s\ + \delta\omega$ where $\delta\omega$ is a detuning parameter, and the length of the linear actuator at the middle of the chassis varies according to $s(t) = s_0 [1 - \cos(\omega_s t)]/2$.

Throughout our simulations, in this chapter, we set $a = 1$, $b/a = 4$, $l/a = 4$, $s_0/l = 1/2$, and $\omega_s = 1$. The characteristic time scale of the two-body system is $T_s = 2\pi/\omega_s$. The parameter c_0 affects both the swimmer's dynamics and flow field around it. For $c_0 \approx 0.5$, it has been shown [19] that the flow field induced by the Quadroar closely resembles that of C. reinhardtii alga [41]. Our numerical experiments show that the resemblance holds for almost any $c_0 \geq 1$. The similarity in behaviors for this broad range of c_0, which even includes the single-frequency case (i.e., $c_0 = 1$), adequately addresses the concern about whether any of emerging dynamical regimes is affected by the presence of two different frequencies. This further highlights the significance of having an oscillatory flow field. To speed up numerical simulations, we set $c_0 = 50$. For individual swimmers, non-zero values of $\delta\omega$ significantly increase the number of orbital families, and in some cases lead to densely interwoven quasi-periodic rosette-shaped trajectories capable of inducing chaotic mixing in the surrounding environment [19]. Here, to focus on the basics of mutual interactions, we consider $\delta\omega$=0. The results of this study are still valid for small $\delta\omega$, but start to deviate and become more involved as $\delta\omega$ increases. Note that $a = 1\mu m$ leads to a Quadroar of $\sim$ 8-12μm, which is similar to the size of a *C. reinhardtii* cell. Moreover, setting $c_0 = 50$ results in the frequency of $50Hz$ for the disks, reminiscent of the flagella beat frequency for a *C. reinhardtii* cell [41]. For a more detailed description of an isolated Quadroar swimmer's dynamics and induced flow fields, the reader is referred to chapters 2 and 4.

3.3 Results and Discussion

Two of our swimmers, depending on their relative initial locations $(\mathrm{d}X_1, \mathrm{d}X_3)$ portray a range of various trajectories as a result of their mutual hydrodynamic interactions. These trajectories range from converging, diverging, and oscillatory motions (which are also seen in other artificial micro-swimmers [e.g. 39]), to forming *braids* (Fig.3.2b), and even *dynamical*

equilibria (Figs 3.2e and 3.5b) which, to the best of our knowledge, have never been observed in low-Reynolds-number swimming. We also report capture into *bound orbits* (Fig. 3.5c) for two interacting micro-swimmers swimming in an infinite unbounded fluid.

In order to systematically study different possibilities of two-swimmer choreographies, induced by hydrodynamic interactions, we consider the effects of relative swimming directions and initial locations which, in turn, also covers phase shift effects. To illustrate the latter, note that since there is no explicit time dependency in the Stokes regime, swimmers with an arbitrary phase shift between them (as a result of being launched at different times) can be considered as two in-phase swimmers with initial locations described at the moment that the second swimmer is turned on. For simplicity, through this chapter we focus on interaction dynamics in the planar phase space. Nevertheless, our findings can be inherently generalized to a three-dimensional (3D) space. Our study is also conventionally arranged into two general categories: (i) the two swimmers are released in the same direction such that their initial x_3-axes are parallel and both aligned with the positive X_3-axis (cf. Fig.3.1), and (ii) the two swimmers are initially facing opposite directions such that at $t = 0$ the following conditions hold: $\hat{\boldsymbol{x}}_{3A} \cdot \hat{\boldsymbol{X}}_3$=1, and $\hat{\boldsymbol{x}}_{3B} \cdot \hat{\boldsymbol{X}}_3$=-1, where the hat sign denotes unit vector. The resulting parameter space for each of these general cases is still valid for small perturbations. For larger perturbations, however, the parameter space starts to deviate from the presented plot and gradually tends to that of the other extreme. For example, by changing the relative angle between the swimmers' initial x_3-axes from zero to π, the corresponding parameter space diagram will gradually transform from Fig. 3.2a (swimming in the same direction) to Fig. 3.5a (swimming in opposite directions).

The parameter space for the trajectories of two swimmers released parallel and in the same direction [case (i)] is displayed in Fig. 3.2(a) with sample trajectories demonstrated in Figures 3.2(b)-(e). In these figures, the swimmers would follow dashed lines in the absence of hydrodynamic interactions. If the two swimmers are released close to each other, and depending on their relative locations, they form a variety of braids with different shapes (Fig. 3.2b). Interestingly, we find that forward translational motion along a braid is faster, sometimes by a factor of two, than the motion of individual swimmers in the absence of hydrodynamic interactions. This phenomenon, which we refer to as *hydrodynamic slingshot effect*, can be easily deduced from Fig.3.2(b): two hydrodynamically interacting swimmers advance along braids, and therefore in space (motion along colored lines), faster than non-interacting swimmers (moving along dashed lines) whose actuation parameters and initial conditions exactly match those of the interacting ones. The slingshot effect is caused by a synergistic process: each swimmer induces an advection field that sums with the relative velocity of its companion swimmer with respect to the background fluid, boosting the absolute velocity of the companion swimmer. A snapshot of the flow field induced by the system of two swimmers advancing along a braid-like trajectory, as well as the corresponding streamlines, are presented in Fig. 3.3. It illustrates how each swimmer induces an advection field at the geometric center of the other swimmer, boosting its absolute translational velocity. The net flow field could also be described as a constructive interference of the two swimmers' flow fields (see Fig. 3.3). Thus, the resultant net flow field is similar to the one induced by a

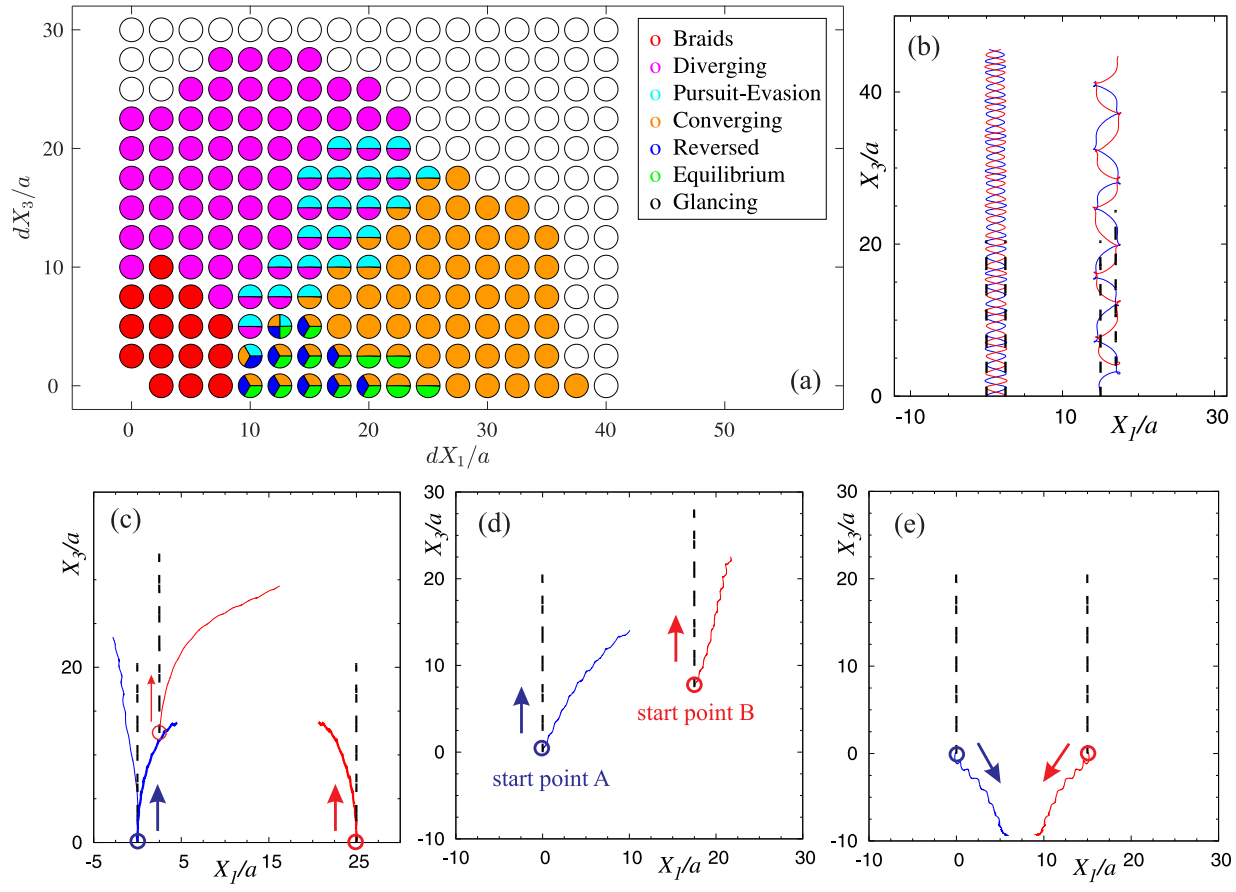

Figure 3.2: Coupled dynamics of two initially co-moving micro-swimmers as a function of their initial relative positions. (a) The orbital/trajectory structure in the parameter space $(\mathrm{d}X_1, \mathrm{d}X_3)$. Trajectories belong to two general families: braids (b) and non-orbiting paths such as diverging (thin lines) and converging (thick lines) (c), pursuit-evasion (d), and reversed motion that ends up at a dynamical equilibrium state (e). Orbits corresponding to the initial conditions marked as "glancing" in panel (a) exhibit small drifts from straight paths. All simulations have been performed over the time span of $[0, 10T_s]$. The trajectories of the swimmers have been plotted in blue and red colors. The launch direction of each swimmer and also the starting positions of swimmers A and B are marked in panels (c)-(e). The swimmers would move on dashed lines in the absence of hydrodynamic interactions, i.e. when swimming alone. Since simulation times are identical, the longer the traveled distances, the faster the swimmers' motions.

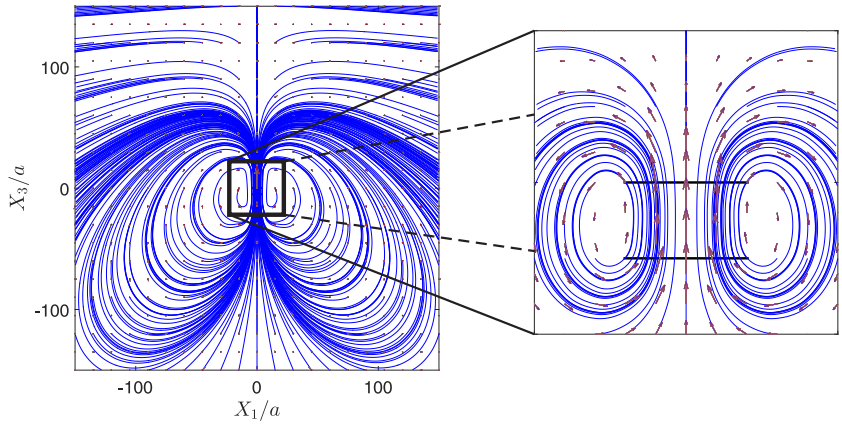

Figure 3.3: Streamlines of the flow field induced by two micro-swimmers boosting each other's swimming speed via the hydrodynamic slingshot effect. The swimmers have initial velocities of the same magnitude and swimming in the same direction. The presented snapshot at $t/T_s = 0.05$, and relative initial positions are $\mathrm{d}X_1/a = 0$ and $\mathrm{d}X_3/a = 5$, which correspond to the braid-like trajectories. Simulation parameters are the same as the ones used in Fig. 3.2. Rectangular selection (magnified in the right panel) shows the area near the two swimmers, and black bars in the right panel are the swimmers' chassis.

single Quadroar swimmer [15], yet with a more powerful propellers (i.e. higher values of c_0).

Other families of trajectories that we observe for interacting swimmers belong to a general family of non-orbiting paths including diverging and converging trajectories (Fig. 3.2c). Non-orbiting paths may occur as pursuit-evasion games when one of the swimmers chases the other one (Fig. 3.2d). The most interesting non-orbiting path that we have found happens when the swimmers get in a reverse motion (Fig. 3.2e, colored dark blue in Fig. 3.2a), eventually reaching to a *dynamical equilibrium*. In dynamical equilibrium states, the swimmers' propellers are working continuously and their flow fields form a saddle structure (Fig. 3.4). The net flow of the saddle structure is zero, so follows the equilibrium state. In the space between the swimmers, fluid is pumped out in a direction almost parallel to the chassis of both swimmers, and is sucked back normal to the chassis. Four prominent vortices are formed around the propellers of the swimmers. These vortices are enclosed by a large-scale hyperbolic structure. Our long-term simulations show that dynamical equilibria are stable to small perturbations. This is a counter-intuitive property because the existence of hyperbolic structures usually implies local instability. The existence of dynamical equilibria for $N > 2$ swimmers is an unsolved problem, whose solution can sharpen our understanding of bacterial clustering and motile cell accumulations.[45, 46]

If the initial distance of the swimmers is large enough, their hydrodynamic interaction will be very small, drifting the swimmers slightly off their straight trajectories. We have

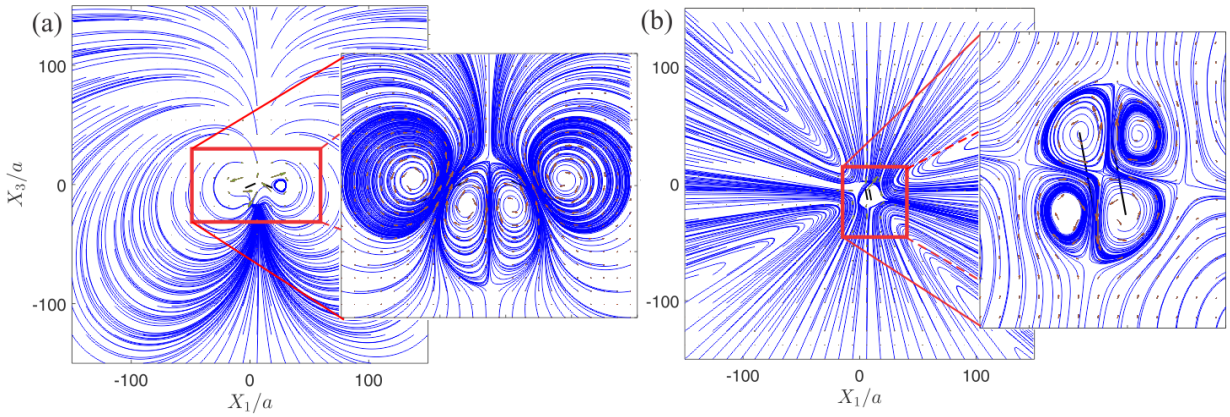

Figure 3.4: Snapshots of the flow field induced by two micro-swimmers representing the reversed converging behavior that leads to a dynamical equilibrium – see the panel (e) in Fig. 3.2. The swimmers have initial velocities of the same magnitude and in the same direction. Their relative initial positions are $\mathrm{d}X_1/a = 15$ and $\mathrm{d}X_3/a = 0$. Snapshots have been taken at $t/T_s = 1$ (a) and $t/T_s = 40$ (b), and the blue lines represent streamlines of the induced flow fields. At full equilibrium state, corresponding to $t/T_s = 40$, four vortices have been formed by the swimmers. Simulation parameters are same as the ones used in Fig. 3.2. Thick solid black bars represent the side views of the chassis, and the area near the two swimmers have been magnified in right panels.

also observed a switch between different trajectories as the two-body system evolves. For instance, a converging motion may end up in an equilibrium state, or pursuit-evasion game may bifurcate to either of converging or diverging paths. In the parameter space, we have marked these cases with two or more colors (Fig. 3.2a).

Two swimmers starting their motions in opposite directions [case (ii)] exhibit different orbital topologies from what we observed for co-directional ones. Their two-body dynamics depends on the impact parameter dX_1 (Fig. 3.5a). When the impact parameter is relatively small ($dX_1/a \lesssim 5$) and the swimmers initially move towards each other, $\mathrm{d}X_3 > 0$, we always obtain an equilibrium state (Fig. 3.5b). Similar to the equilibria of case (i), the actuators of the swimmers are operational at the equilibrium state and energy is consumed only for flow generation (and not translation). For large impact factors, $\mathrm{d}X_1/a \gtrsim 15$, trajectories are deflected similar to the lensing/refraction of light rays (Fig. 3.5d). Our results are in agreement with the angle-preserving behavior reported in the confrontation of two T-dual swimmers [47]. For intermediate impact factors, we observe a *capture* phenomenon as the micro-swimmers begin to orbit each other after a translational phase (Fig. 3.5c). It is to be noted that capture into a quasi-periodic orbit is a transitional state between dynamical equilibria and deflecting trajectories. Such transitional states fill a complex fractal-shaped region of the parameter space, showing high degree of sensitivity to initial conditions [see the zoomed-in box in Fig. 3.5(a)] with the dominant length-scale of a disk radius. This

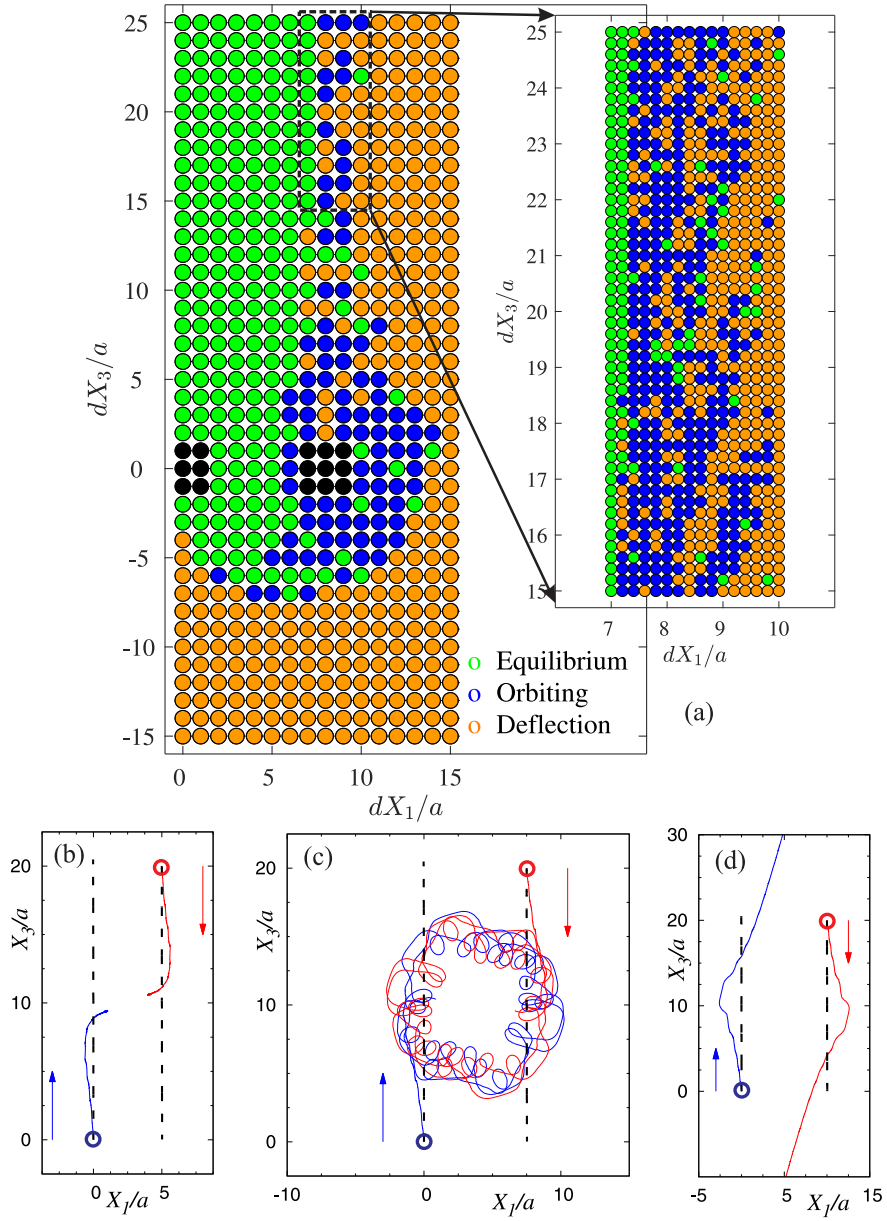

Figure 3.5: Coupled dynamics of two swimmers initially moving in opposite directions. (a) The parameter space of possible trajectories. We have used finer grids in the zoomed area. (b) Moving towards an equilibrium state. (c) Capture into a bound quasi-periodic orbit. (d) Deflection of trajectories after a close encounter. In panels (b)-(d), the trajectories of the swimmers have been shown by blue and red solid lines. The arrows denote the launch directions of the swimmers, and the circles mark their starting positions. The swimmers would follow dashed lines in the absence of hydrodynamic interactions.

result suggests the existence of highly chaotic N-body systems of micro-swimmers. Although details of trajectories in an orbiting motion can be complex, the bounded nature of the overall two-body motion in an infinite fluid domain is a unique physical process, for which many applications can be sought. Examples include mixing by micro-swimmers and trapping microorganisms by artificial swimming micro-robots.

3.4 Other Notes

3.4.1 On the Numerical Approach

At each time step of the presented numerical modeling, we first substitute expressions describing point-forces and -torques (4.12 and 4.6) into the force and torque balance equations. Then, together with mathematical expressions describing velocity and vorticity fields (presented in 3.9 and 3.10), the system is solved for the 20 vectorial (i.e. 60 scalar in 3D) unknowns; i.e. $\boldsymbol{v}_{j,c}$, $\boldsymbol{\omega}_{j,\text{body}}$, $\boldsymbol{u}_{jn}$ and $\boldsymbol{\Omega}_{jn}$ ($j = A, B$; $n = 1, \ldots, 4$). We then find the position and orientation of each swimmer by integrating $\boldsymbol{v}_{j,c}$ and $\boldsymbol{\omega}_{j,\text{body}}$ in time. The angular velocity of each swimmer, denoted by $\boldsymbol{\omega}_{j,\text{body}}$, is then related to the yaw-pitch-roll sequence of the Euler's angles, $\boldsymbol{\alpha} = (\phi, \theta, \psi)$, through

$$\dot{\boldsymbol{\alpha}}_j = \boldsymbol{T}_j^{-1} \cdot \boldsymbol{\omega}_{j,\text{body}}, \quad T = \begin{bmatrix} 1 & 0 & -sin\,(\theta) \\ 0 & \cos(\phi) & \cos(\theta)\sin(\phi) \\ 0 & -\sin(\phi) & \cos(\theta)\cos(\phi) \end{bmatrix}. \tag{3.13}$$

It is worth noting that there is a coordinate-type singularity in T when $\theta = \pm\pi/2$. Therefore, here all computations have been carried out in the space of unit quaternions, $\boldsymbol{q}$, and then outputs are mapped back onto the space of Euler's angles $\boldsymbol{\alpha}$ [19]:

$$\dot{\boldsymbol{q}}_j = \frac{1}{2} \begin{bmatrix} 0 & -\omega_1 & -\omega_2 & -\omega_3 \\ \omega_1 & 0 & \omega_3 & -\omega_2 \\ \omega_2 & -\omega_3 & 0 & \omega_1 \\ \omega_3 & \omega_2 & -\omega_1 & 0 \end{bmatrix} \boldsymbol{q}_j, \quad \boldsymbol{\omega}_{j,\text{body}} = (\omega_1, \omega_2, \omega_3). \tag{3.14}$$

3.4.2 Three-dimensional Beads Model Simulation

In order to further validate the employed model based representing the disks with point-forces and -torques, here we develop a full three-dimensional beads realization of the disks [48, 49]. To this end, we first briefly explain the concept of beads model using Fig. 3.6(a), then compare the results of our numerical method with those of a beads model simulation.

A single spherical bead, moving with velocity v_0, in Stokes regime induces a well-known velocity field in the surrounding fluid. For an arbitrary point in cylindrical coordinate system, this velocity field in radial and tangential directions is given by:

$$v_r = \left(\frac{3R_0}{2r} - \frac{R_0^3}{2r^3}\right) v_0\ cos\theta, \quad v_\theta = -\left(\frac{3R_0}{4r} + \frac{R_0^3}{4r^3}\right) v_0\ sin\theta, \tag{3.15}$$

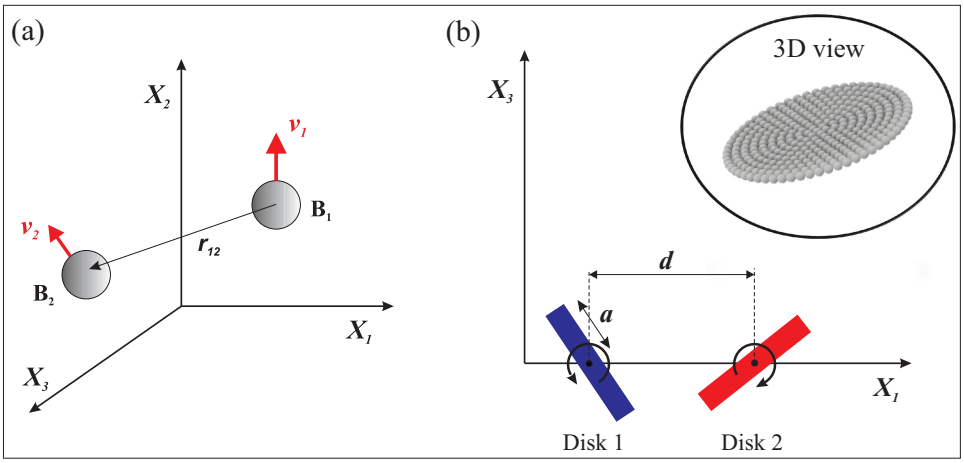

Figure 3.6: (a) Schematic representation for the basic idea of beads model. Beads B_1 and B_2 are moving with absolute velocities v_1 and v_2 with respect to the stationary reference frame fixed to the fluid at infinity. (b) Schematics of the three-dimensional (3D) beads model realization of two nearby interacting disks of radius a and distance d apart. The inset shows the 3D view of a single disk composed of 331 spherical beads.

where R_0 is the radius of the bead, and $r\boldsymbol{e}_r$ is the position vector of the arbitrary point with respect to the bead's center. Let us consider two beads, B_1 and B_2, moving with absolute velocities v_1 and v_2, in the stationary frame, as shown in Fig. 3.6(a). With respect to the background fluid, B_1 (or B_2) has a hydrodynamic velocity $\boldsymbol{v}_{1H}$ (or $\boldsymbol{v}_{2H}$), and thus induces a velocity field $\boldsymbol{v}_{1H,2}$ (or $\boldsymbol{v}_{2H,1}$) at the position of B_2 (or B_1). Therefore, the hydrodynamic velocity of each bead is given by the following implicit formula:

$$\boldsymbol{v}_{1H} = \boldsymbol{v}_1 - \boldsymbol{v}_{2H,1}, \quad \boldsymbol{v}_{2H} = \boldsymbol{v}_2 - \boldsymbol{v}_{1H,2}. \tag{3.16}$$

Generalization of this simple idea, in order to formulate hydrodynamics of a system composed of N beads, results in the following system of linear algebraic equations:

$$\boldsymbol{v}_{iH} + \sum_{j=1, j\neq i}^{N} \boldsymbol{v}_{jH,i} = \boldsymbol{v}_i, \quad i \in \{1, \cdots, N\}. \tag{3.17}$$

The fluid velocity $\boldsymbol{v}_{jH,i}$, represents the flow induced at the position of bead B_i due to the motion of bead B_j and follows from equation (3.15) as:

$$v_{r-jH,i} = \left(\frac{3R_0}{2r_{ji}} - \frac{R_0^3}{2r_{ji}^3}\right) v_{jH}\ cos\theta_{ji}, \tag{3.18}$$

$$v_{\theta-jH,i} = -\left(\frac{3R_0}{4r_{ji}} + \frac{R_0^3}{4r_{ji}^3}\right) v_{jH}\ sin\theta_{ji}, \tag{3.19}$$

where $r_{ji} = |\boldsymbol{r}_i - \boldsymbol{r}_j|$; $\boldsymbol{r}_i$ and $\boldsymbol{r}_j$ are position vectors of beads B_1 and B_2; and θ_{ji} is defined by $cos\theta_{ji} = (\boldsymbol{r}_{ji} \cdot \boldsymbol{v}_{jH}) \,/\, (r_{ji} v_{jH})$. To put the system of equations (3.17) into the standard format of $\mathscr{A}X = \mathscr{B}$, the general hydrodynamic relations between beads is defined here as:

$$\boldsymbol{v}_{m,n} = \boldsymbol{A}_{mn} \boldsymbol{v}_m, \quad \{m, n\} \in \{1, \cdots, N\}, \tag{3.20}$$

$$\boldsymbol{A}_{mn} = [S^{(1)}_{3\times1}, S^{(2)}_{3\times1}, S^{(3)}_{3\times1}], \tag{3.21}$$

where $S^{(k)}_{3\times1}$ for each $k \in \{1, 2, 3\}$ is a column vector given by:

$$S^{(1)}_{3\times1} = \left(\frac{3R_0}{2r_{mn}} - \frac{R_0^3}{2r_{mn}^3}\right) \begin{bmatrix} x^2 \\ xy \\ xz \end{bmatrix} - \left(\frac{3R_0}{4r_{mn}} + \frac{R_0^3}{4r_{mn}^3}\right) \sqrt{\frac{r_{mn}^2 - x^2}{y^2 + z^2}} \begin{bmatrix} -(y^2 + z^2) \\ xy \\ xz \end{bmatrix}, \tag{3.22}$$

$$S^{(2)}_{3\times1} = \left(\frac{3R_0}{2r_{mn}} - \frac{R_0^3}{2r_{mn}^3}\right) \begin{bmatrix} yx \\ y^2 \\ yz \end{bmatrix} - \left(\frac{3R_0}{4r_{mn}} + \frac{R_0^3}{4r_{mn}^3}\right) \sqrt{\frac{r_{mn}^2 - y^2}{x^2 + z^2}} \begin{bmatrix} yx \\ -(x^2 + z^2) \\ yz \end{bmatrix}, \tag{3.23}$$

$$S^{(3)}_{3\times1} = \left(\frac{3R_0}{2r_{mn}} - \frac{R_0^3}{2r_{mn}^3}\right) \begin{bmatrix} zx \\ zy \\ z^2 \end{bmatrix} - \left(\frac{3R_0}{4r_{mn}} + \frac{R_0^3}{4r_{mn}^3}\right) \sqrt{\frac{r_{mn}^2 - z^2}{x^2 + y^2}} \begin{bmatrix} zx \\ zy \\ -(x^2 + y^2) \end{bmatrix}, \tag{3.24}$$

Note that here $\boldsymbol{r}_{mn} = \boldsymbol{r}_n - \boldsymbol{r}_m = (x, y, z)$. Applying this representation to the general formulation of the system of N beads presented in equation (3.17), leads to the following implicit system of linear equations:

$$\begin{bmatrix} I_{3\times3} & A_{21} & \cdots & A_{N1} \\ A_{12} & I_{3\times3} & \cdots & A_{N2} \\ \vdots & \vdots & \vdots & \vdots \\ A_{1N} & A_{2N} & \cdots & I_{3\times3} \end{bmatrix}_{3N\times3N} \begin{bmatrix} \boldsymbol{v}_{1H} \\ \boldsymbol{v}_{2H} \\ \vdots \\ \boldsymbol{v}_{NH} \end{bmatrix}_{3N\times1} = \begin{bmatrix} \boldsymbol{v}_1 \\ \boldsymbol{v}_2 \\ \vdots \\ \boldsymbol{v}_N \end{bmatrix}_{3N\times1}. \tag{3.25}$$

This system of equations can then be solved using standard linear algebra methods. The inputs of the system are absolute velocities, $\boldsymbol{v}_i$, which are assigned to individual beads that assemble a rigid body, and outputs are hydrodynamic velocities.

To further validate the presented results (obtained through a simplified singularity method that models influence of each disk using a pair of point-force and point-torque), we compare them against those obtained by simulating the real geometry of the swimmers' disks using the described beads model. Specifically, we compare our simplified numerical method of modeling hydrodynamic interactions, against a 3D beads model realization of two nearby rotating disks, where each disk is composed of a large number of beads (see Fig. 3.6b).

Schematics of the problem setup are presented in Fig. 3.6(b), where two disks of radius a located at a distance of d from each other, are rotating with angular velocities ω_1 and ω_2, respectively. The interaction of these two disks is modeled using: (i) our singularity-based method using the point-force and point-torque models, and (ii) the full three-dimensional (3D) beads simulation. For the latter approach, the optimum number of beads required

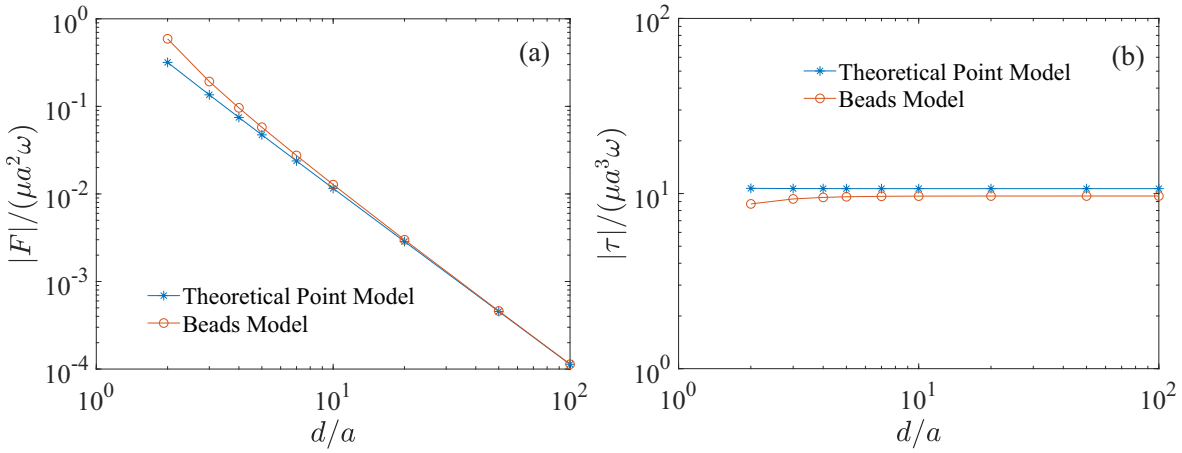

Figure 3.7: Comparison between the results obtained from the theoretical singularity-based method (i.e. the ones based on point forces and torques) with those obtained from the 3D beads model simulation. The panels demonstrate magnitudes of the total force (a) and torque (b) exerted on two interacting rotary disks of radius a as a function of their distance. The schematics of our setup has been shown in Fig. 3.6(b). We have set $\omega = |\omega_1| = |\omega_2| = 0.5\omega_s$. Stars and circles respectively correspond to the results of our theoretical singularity-based (i.e. point forces and torques) and the 3D beads-based simulation, respectively.

to model each disk is determined through the convergence of numerical results. For the case presented in Fig. 3.6(b), as an example, the optimum number of beads is 331, which corresponds to $R_0/a = 1/21 \approx 0.05$. It should be noted that the thickness ($2R_0$) of each disk can be neglected compared to its diameter ($2a$), as expected by the swimmer model. For the beads model simulation, the set of equations (3.25) must be solved for the entire system of the beads. Drag element exerted on each bead ce be then determined by multiplying the translational drag coefficient, $6\pi\mu R_0$, to the bead's consequent hydrodynamic velocity. At the end, we compare the results of this 3D beads-based simulation to numerical results obtained for the singularity-based model using point forces and torques. Our results displayed in Fig. 3.7 show a good agreement between the two models, even for small distances as $d = 2a$ between the disks. In particular, we monitor (in Fig. 3.7) magnitudes of the total force and torque exerted on the disks as a function of their distance. Here the disks are counter-rotating with $|\omega_1| = |\omega_2| = 0.5\omega_s$, and the total exerted force and torque (on each) are computed instantaneously for different distances between them.

3.5 Concluding Remarks

In this chapter, we revealed that two micro-swimmers in Stokes regime can stop each other by forming a dynamic equilibrium in an infinite fluid domain. Furthermore, depending on

where the two interacting micro-swimmers are released, they may also get trapped into bounded orbits and revolve about each other indefinitely. We then systematically studied the entire phase space of a hydrodynamically interacting two-swimmer system in Stokes regime, and identified the basins of dynamical equilibria and periodic orbits in the parameter space. We also found other diverse sets of orbits including closely winding braids, and pursuit–evasion dynamics. Sensitivity to initial conditions, slingshot effect for motions along braids, dynamical equilibria, and capture into bound orbits, as demonstrated in this study, can have unexpected implications to motion of micro-swimmers. Our findings also provide a new insight into the emergence of turbulence and energy budget in active fluids: two-body dynamical equilibria, and if exist, N-body equilibria, dissipate the energy injected into actuators without causing any directional streaming in the active particle phase (fluid of micro-swimmers). This suggests that non-local models of passive and active stresses due to hydrodynamic and steric interactions need modifications as diffusion in the phase space cannot be modeled only as a function of macroscopic streaming velocity.

Acknowledgments

This work is supported by the National Science Foundation grant CMMI-1562871.

Chapter 4

Near Wall Behavior and Purely Hydrodynamic Scattering

In this chapter, we conduct a systematic investigation on the near-wall behavior of a model micro-swimmer whose flow field resembles that of bi-flagellate green algae, *Chlamydomonas reinhardtii*. In particular, we show that the scattering of these micro-swimmers from a wall can be purely hydrodynamic and that no mechanical force is needed for sensing and escaping solid boundaries. Our findings further suggest a hydrodynamic nature for the surface-scattering process of micro-swimmers with flow characteristics of bi-flagellate algae – i.e. those that induce an oscillatory flow field with anterior, side and posterior vortices.

4.1 Introduction

Interaction of swimming microorganisms with solid boundaries is vital to numerous biological processes ranging from fertilization [50] to biofilm formation [51]. While the significance of such interactions have been acknowledged extensively [e.g. 52, 53], the underlying mechanism is yet a matter of dispute. Specifically, there is an unresolved debate over whether it is the *short-range steric* or the *long-range hydrodynamic* that primarily rule micro-swimmers interactions with solid boundaries. For microorganisms with rear-mounted flagella ('pushers', such as *Escherichia coli* bacteria and human spermatozoa), recent studies finally put an end to the debate in support of the hydrodynamic interactions [54, 55]. However, for the other major group of microorganisms ('pullers', i.e. those with front-mounted flagella such as *C. reinhardtii*) the primary mechanism of surface scattering has still remained unsettled.

Few recent theoretical and numerical studies [e.g. 56, 57] have shown that specific puller-type swimmers (such as deformable swimmers with amoeboid motion) can undergo purely hydrodynamic scattering in a channel (termed as 'navigation swimming' [56]). Whereas, for the case of *C. reinhardtii* (widely known as the paradigm of puller-type swimmers), it has been believed that the scattering process is mainly governed by contact/flagellar forces rather than hydrodynamic interactions. Experiments have shown that *C. reinhardtii* cells

can feel and escape a boundary after getting close enough to the wall [see e.g. 58]. Based on a series of visual observations, it has been claimed that contact forces exerted by flagella to the wall drives the interaction. The observation has been further generalized, suggesting that surface scattering of swimming eukaryotes is primarily steric rather than hydrodynamic [58]. More recent experimental observations [59], nevertheless, do not support this claim: in scattering of *C. reinhardtii* cells from a curved surface, there exist some cases in which the flagella do not even touch the wall [59].

Here, we consider a model micro-swimmer designed in such a way that its flow field closely resembles that of a *C. reinhardtii* [19]. Specifically, it induces an oscillatory flow field with anterior, side and posterior vortices in the surrounding fluid. These are characteristics of the flow field generated by the green alga *C. reinhardtii* [41]. Through direct computation, we show that this model swimmer can feel and escape the wall similar to *C. reinhardtii*, without the need for a physical contact with the wall; hence, the scattering is purely hydrodynamic.

C. reinhardtii is usually categorized under the puller-type swimmers, mainly because it induces the flow field of a contractile force dipole in the far field during its effective stroke. However, the flow field induced by this motile cell in its *close* vicinity, which is of particular importance in the swimmer-wall interactions, is not just a simple puller- or pusher-type: it is an oscillatory flow field that includes side, anterior, and posterior vortices (see e.g. [41, 60]). To mimic this complex flow field, we use the proposed *Quadroar* micro-swimmer. As discussed in chapter 2, the swimmer consists of two pairs of counter-rotating disks whose distance is periodically varied (Fig. 4.1a). When all motions (reciprocating and rotating) have the same frequency and there is no phase difference, the model swimmer moves along a straight line in the x_3 direction, and induces an oscillatory flow field with side, anterior and posterior vortices (Fig. 4.1c). This flow field closely resembles the flow field of a *C. reinhardtii* cell [19, 41]. Specifically, oscillation of the linear actuator creates the oscillatory flow field between puller and pusher types, and the counter-rotation of disks contributes to the emergence of anterior, posterior, and side vortices. Via varying the relative frequency of propellers, or by imposing phase-differences between them, a full three dimensional reorientation maneuvers and tumblings can be obtained [15, 19].

4.2 Mathematical Formulation

Here, we consider a single swimmer moving near a no-slip solid boundary. The global frame of reference is fixed to the wall such that its X_3-axis is normal to the wall and points toward the semi-infinite fluid (Fig. 4.1b). The swimmer's local frame of reference is attached to its geometric center so that its frame lies in (x_1, x_2)-plane, and x_1-axis is along the reciprocating chassis (Fig. 4.1a). In our modelings, the length of each disk axle is denoted by $2b$, and reciprocating chassis' length is $2l + 2s\,(t)$ where $s\,(t) = s_m\,[1 - cos\,(\omega_s t)]\,/2$, in which s_m is the amplitude and ω_s is the frequency of oscillations. Angular velocities of the disks on left and right axles are $c_0\omega_s$ and $-c_0\omega_s$, where c_0 is a constant. We choose $b/a = l/a = 4$ and $s_m/a = 2$, and by choosing $\omega_s = 1$, all frequencies in the problem are normalized by ω_s.

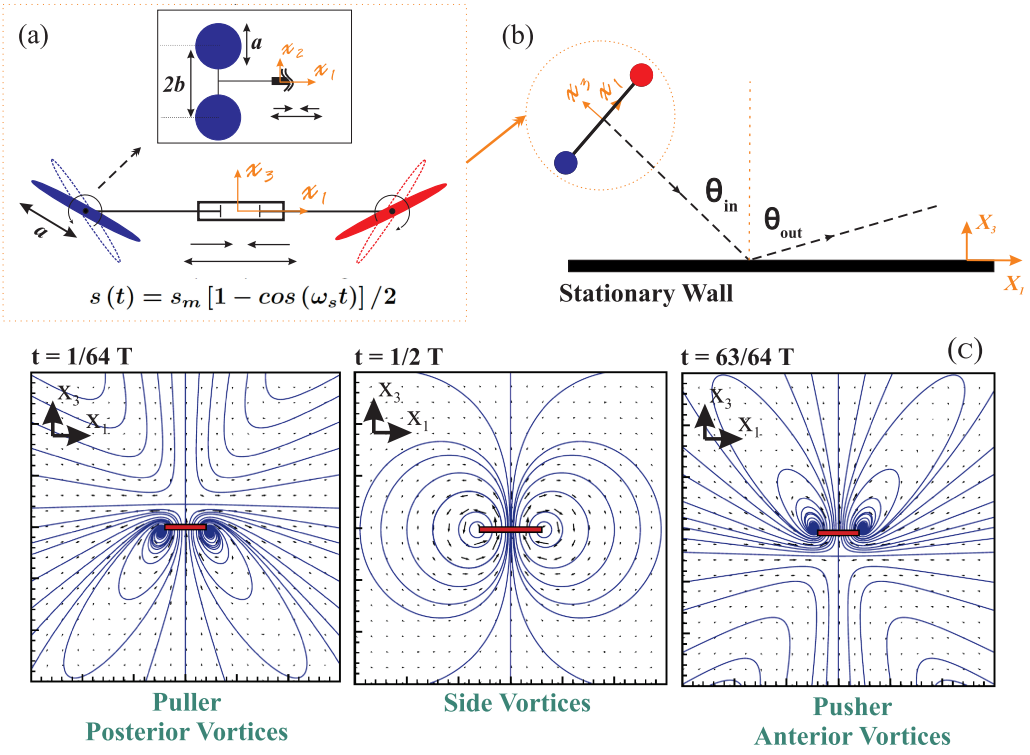

Figure 4.1: (a) Schematic of the model swimmer, which combines harmonic oscillation of its body length with counter-rotation of propellers. (b) Schematic representation of the model swimmer scattering off a stationary solid wall. θ_{in} and θ_{out} are defined with respect to the axis normal to the wall. (c) Snapshots of the oscillatory flow field induced by a single model swimmer in an infinite fluid [19], which mimics the flow field around a *C. reinhardtii* cell [41]. The red thick bar represents chassis of the swimmer, blue lines demonstrate the induced streamlines, and the time scale is $T = 2\pi/\omega_s$.

Throughout this chapter, unless otherwise noted, $c_0 = 50$ which is reminiscent of the flagella beat frequency of a *C. reinhardtii* cell (that is $\sim 50\ Hz$).

4.2.1 Model swimmer in an infinite fluid: singularity solution

Due to the micro-scale size of the swimmer, the corresponding Reynolds number is very small (i.e. $Re \ll 1$). Therefore, the effect of inertia is negligibly small compared to viscous effects, and Navier-Stokes equation of motion can be simplified to the Stokes equation:

$$\nabla P = \eta\, \nabla^2 \boldsymbol{u} + \boldsymbol{F}, \quad \nabla \cdot \boldsymbol{u} = 0, \tag{4.1}$$

where P is the pressure filed, $\boldsymbol{u}$ is the velocity field, η is dynamic viscosity of the ambient fluid, and $\boldsymbol{F}$ is the body force per unit volume.

The model swimmer has four propellers (disks of radii a) which are placed at the ends of its left and right axles. Contribution of each disk to background streaming can be modeled as a combination of point-force ($\boldsymbol{f}$) and point-torque ($\boldsymbol{\gamma}$) flow fields. The force and torque acting on each disk i is given by

$$\boldsymbol{f}_i = \eta\ \mathscr{K}_i \cdot (\boldsymbol{v}_i - \boldsymbol{u}_i)\,, \tag{4.2}$$

$$\boldsymbol{\gamma}_i = \eta\ \mathscr{G} \cdot (\boldsymbol{\omega}_i - \boldsymbol{\Omega}_i)\,, \tag{4.3}$$

where $\boldsymbol{v}_i$ and $\boldsymbol{\omega}_i$ are absolute linear and angular velocities of disk i; $\boldsymbol{u}_i$ and $2\boldsymbol{\Omega}_i$ are velocity and vorticity fields of the background fluid at the position of disk i, and η is dynamic viscosity. The geometry of disks are hidden in $\mathscr{K}_i$,$\mathscr{G}$, which are tensors of rank two. Specifically, $\mathscr{K}_i$ is the translation tensor corresponding to disk i, and $\mathscr{G}$ is isotropic rotational tensor of a circular disk rotating about its diameter, with the forms given by [61]:

$$\mathscr{K}_i = \tfrac{8}{3}a \begin{bmatrix} 5 - cos\,(2\alpha_i) & 0 & sin\,(2\alpha_i) \\ 0 & 4 & 0 \\ sin\,(2\alpha_i) & 0 & 5 + cos\,(2\alpha_i) \end{bmatrix}, \tag{4.4}$$

$$\mathscr{G} = \tfrac{32}{3}a^3\boldsymbol{I}, \tag{4.5}$$

where $\boldsymbol{I}$ is the identity tensor, a is radius of each disk, and α_i denotes the angle that disk i makes with (x_1, x_2)-plane of the swimmer. Considering only the point-force contribution of each propeller in an infinite fluid domain, the governing equation can be written as:

$$\nabla P = \eta\ \nabla^2\boldsymbol{u} + \boldsymbol{f}\delta(\boldsymbol{r}), \quad \nabla \cdot \boldsymbol{u} = 0, \tag{4.6}$$

where $\delta\,(\boldsymbol{r})$ is Dirac delta function. The point-force is exerted at $\boldsymbol{x}_0$, and for a generic point $\boldsymbol{x}$ in space $\boldsymbol{r} = \boldsymbol{x} - \boldsymbol{x}_0$ with $r = |\boldsymbol{r}|$. Equation (4.6) can be analytically solved in several ways (see e.g. [44]), and the resultant velocity field is known as Stokeslet:

$$\boldsymbol{u}\,(\boldsymbol{r}, t) = \frac{\boldsymbol{f}}{8\pi\eta} \cdot \left(\frac{\boldsymbol{I}}{r} + \frac{\boldsymbol{r}\boldsymbol{r}}{r^3}\right). \tag{4.7}$$

The contribution of a point-torque $\boldsymbol{\gamma}$ exerted at a point $\boldsymbol{x}_0$ in an infinite fluid, on the other hand, is derived from the following set of equations [44]:

$$\nabla P = \eta\ \nabla^2\boldsymbol{u} + \nabla \times (\boldsymbol{\gamma}\delta(\boldsymbol{r}))\,, \quad \nabla \cdot \boldsymbol{u} = 0. \tag{4.8}$$

The exact solution to (4.8) is also available (see e.g. [44]), and is called a rotlet:

$$\boldsymbol{u}\,(\boldsymbol{r}, t) = \frac{1}{8\pi\eta}\left(\frac{\boldsymbol{\gamma} \times \boldsymbol{r}}{r^3}\right). \tag{4.9}$$

Linearity of Stokes equation allows us to invoke the principle of superposition. As a result, the net contribution of each disk (when placed in an unbounded fluid domain) to background streaming, can be modeled as the combination of a Stokeslet and a rotlet:

$$\boldsymbol{u}\,(\boldsymbol{r}, t) = \frac{\boldsymbol{f}}{8\pi\eta} \cdot \left(\frac{\boldsymbol{I}}{r} + \frac{\boldsymbol{r}\boldsymbol{r}}{r^3}\right) + \frac{1}{8\pi\eta}\left(\frac{\boldsymbol{\gamma} \times \boldsymbol{r}}{r^3}\right). \tag{4.10}$$

The velocity field that the model swimmer induces in its surrounding (when swimming in an infinite fluid domain) is then the sum of contributions from all of its disks:

$$\boldsymbol{u}\left(\boldsymbol{x},t\right)=\frac{1}{8\pi\eta}\sum_{k=1}^{4}\left(\frac{\boldsymbol{f}_k}{r_k}+\frac{\boldsymbol{f}_k\cdot\boldsymbol{r}_k}{r_k^3}\boldsymbol{r}_k+\frac{\boldsymbol{\gamma}_k\times\boldsymbol{r}_k}{r_k^3}\right), \tag{4.11}$$

where $\boldsymbol{x}$ is the position vector of a generic point in space, and $\boldsymbol{r}_k$ is the vector connecting geometric center of disk k to this point. To calculate the induced vorticity field, one needs to then take curl of the velocity field ($2\boldsymbol{\Omega}=\nabla\times\boldsymbol{u}$):

$$2\boldsymbol{\Omega}\left(\boldsymbol{x},t\right)=\frac{1}{8\pi\eta}\sum_{k=1}^{4}\left[\frac{2\boldsymbol{f}_k\times\boldsymbol{r}_k}{r_k^3}+\frac{3(\boldsymbol{\gamma}_k\cdot\boldsymbol{r}_k)\boldsymbol{r}_k-r_k^2\boldsymbol{\gamma}_k}{r_k^5}\right]. \tag{4.12}$$

4.2.2 Model swimmer in vicinity of a solid boundary

As discussed in previous section, contribution of each disk to the background streaming is modeled here as a combination of a point-force and a point-torque. Therefore, our model swimmer involves four pairs of singularities. In the vicinity of a no-slip solid boundary, to satisfy the no-penetration and no-slip boundary conditions on the wall, a specific arrangement of singularities – called image systems [62, 63] – is placed at each singularity's image location. The image systems of a Stokeslet ($\boldsymbol{f}$) that is parallel to and at a distance h from a wall is a combination of a Stokeslet ($-\boldsymbol{f}$), Stokes-doublet ($2h\boldsymbol{f}$), and a source-doublet ($-4\eta h^2\boldsymbol{f}$). For a rotlet($\boldsymbol{\gamma}$) at a distance h and parallel to a wall the image system includes a rotlet ($-\boldsymbol{\gamma}$), a stresslet ($16\pi\eta\boldsymbol{\gamma}$), and a source-doublet ($8\pi h\boldsymbol{\gamma}$). For a rotlet ($\boldsymbol{\gamma}$) that is normal to a wall the image system is just a single rotlet ($-\boldsymbol{\gamma}$), but for a Stokeslet ($\boldsymbol{f}$) normal to a wall the image system includes a Stokeslet ($-\boldsymbol{f}$), a Stokes-doublet ($-2h\boldsymbol{f}$), and a source-doublet ($4\eta h^2\boldsymbol{f}$). Stokes-doublet, characterized by a strength tensor of rank two (D_{jk}), is (see e.g. [63, 64]):

$$u_i=\frac{D_{jk}}{8\pi\eta}\left[\left(-\frac{r_i\delta_{jk}}{r^3}+\frac{3r_ir_jr_k}{r^5}\right)+\left(\frac{r_k\delta_{ij}-r_j\delta_{ik}}{r^3}\right)\right]. \tag{4.13}$$

In the case of a force dipole which is symmetric and contributes no net torque to the surrounding fluid, the solution is called stresslet and can simply be defined as the symmetric part of a Stokes-doublet (first term on the right-hand-side of equation (4.13)):

$$u_i^{sym}=\frac{D_{jk}}{8\pi\eta}\left(-\frac{r_i\delta_{jk}}{r^3}+\frac{3r_ir_jr_k}{r^5}\right). \tag{4.14}$$

On the other hand, the skew-symmetric part of a Stokes-doublet (4.13) represents the net torque contribution of a force dipole. Thus, it is equivalent to the rotlet solution:

$$u_i^{skew}=\frac{D_{jk}}{8\pi\eta}\left(\frac{r_k\delta_{ij}-r_j\delta_{ik}}{r^3}\right)\equiv\frac{1}{8\pi\eta}\frac{(\boldsymbol{\gamma}\times\boldsymbol{r})_i}{r^3},$$

where $\gamma_i = -\epsilon_{ijk} D_{jk}$. Finally, the flow field due to a point-source with outward mass flux M is $u_i = (M/4\pi)(r_i/r^3)$. Therefore, the velocity field induced by a source-doublet reads as:

$$u_i = \frac{M_j}{4\pi}\left(-\frac{\delta_{ij}}{r^3} + \frac{3r_i r_j}{r^5}\right). \tag{4.15}$$

Using (4.7), (4.13), and (4.15) as the elements of our image system for a Stokeslet, velocity field due to a point-force near a stationary no-slip wall is obtained as [62]:

$$\begin{aligned} u_i^f = &\frac{f_j}{8\pi\eta}\left[\left(\frac{\delta_{ij}}{r} + \frac{r_i r_j}{r^3}\right) - \left(\frac{\delta_{ij}}{\bar{r}} + \frac{\bar{r}_i \bar{r}_j}{\bar{r}^3}\right)\right] \\ &+ \frac{2h f_j}{8\pi\eta}\left(\delta_{jm}\delta_{mk} - \delta_{j3}\delta_{3k}\right)\frac{\partial}{\partial \bar{r}_k}\left[\frac{h\bar{r}_i}{\bar{r}^3} - \left(\frac{\delta_{i3}}{\bar{r}} + \frac{\bar{r}_i \bar{r}_3}{\bar{r}^3}\right)\right], \end{aligned} \tag{4.16}$$

where η is dynamic viscosity and δ_{ij} is Kronecker delta. The point-force $\boldsymbol{f}$ is exerted at $\boldsymbol{x}_0 = (\xi, \zeta, h)$, and the image point of $\boldsymbol{x}_0$ with respect to the stationary wall is given by $\bar{\boldsymbol{x}}_0 = \boldsymbol{x}_0 - 2\left(\boldsymbol{x}_0 \cdot \boldsymbol{e}_3\right)\boldsymbol{e}_3$, where $\boldsymbol{e}_3$ is the unit vector normal to the wall. Position of a generic point in space is denoted by vector $\boldsymbol{x}$, and $\boldsymbol{r} = \boldsymbol{x} - \boldsymbol{x}_0$. Similarly, relative position of a generic point $\boldsymbol{x}$ from the image point $\bar{\boldsymbol{x}}_0$ is defined as $\bar{\boldsymbol{r}} = \boldsymbol{x} - \bar{\boldsymbol{x}}_0$. Here $m \in \{1, 2\}$, and the expression $\delta_{jm}\delta_{mk} - \delta_{j3}\delta_{3k}$ is non-zero only if $j = k$. Then it is equal to -1 if $j = k = 3$, and equal to $+1$ if $j = k = 1$ *or* $j = k = 2$. Equation (4.16) can be also written in the familiar form of:

$$\boldsymbol{u}^f = \boldsymbol{G} \cdot \boldsymbol{f}, \tag{4.17}$$

where $G_{ij}\left(\boldsymbol{r}, \bar{\boldsymbol{r}}\right)$ stands for the free space Green's function of the Stokes equation:

$$\begin{aligned} G_{ij}\left(\boldsymbol{r}, \bar{\boldsymbol{r}}\right) = &\frac{1}{8\pi\eta}\left[\left(\frac{\delta_{ij}}{r} + \frac{r_i r_j}{r^3}\right) - \left(\frac{\delta_{ij}}{\bar{r}} + \frac{\bar{r}_i \bar{r}_j}{\bar{r}^3}\right)\right] + \frac{1}{8\pi\eta}\left[2h^2\left(1 - 2\delta_{j3}\right)\left(\frac{\delta_{ij}}{\bar{r}^3} - \frac{3\bar{r}_i \bar{r}_j}{\bar{r}^5}\right)\right] \\ &+ \frac{1}{8\pi\eta}\left[2h\left(1 - 2\delta_{j3}\right)\left(\frac{\bar{r}_j \delta_{i3}}{\bar{r}^3} + \frac{3\bar{r}_i \bar{r}_j \bar{r}_3}{\bar{r}^5} - \frac{\bar{r}_3 \delta_{ij}}{\bar{r}^3} - \frac{\bar{r}_i \delta_{j3}}{\bar{r}^3}\right)\right]. \end{aligned} \tag{4.18}$$

Similarly, upon substituting (4.9), (4.14), and (4.15) into the image system of a rotlet, the expression representing flow field induced by a point-torque in the vicinity of a stationary no-slip wall is then derived as [63]:

$$\begin{aligned} u_i^\gamma = &\frac{1}{8\pi\eta}\left[\frac{\left(\boldsymbol{\gamma} \times \boldsymbol{r}\right)_i}{r^3} - \frac{\left(\boldsymbol{\gamma} \times \bar{\boldsymbol{r}}\right)_i}{\bar{r}^3}\right] \\ &+ \frac{1}{8\pi\eta}\left[2h\epsilon_{kj3}\gamma_j\left(\frac{\delta_{ik}}{\bar{r}^3} - \frac{3\bar{r}_i \bar{r}_k}{\bar{r}^5}\right) + 6\epsilon_{kj3}\frac{\gamma_j \bar{r}_i \bar{r}_k \bar{r}_3}{\bar{r}^5}\right]. \end{aligned} \tag{4.19}$$

To sum up, for our model swimmer when swimming in vicinity of a solid boundary, the contribution of each propeller (p) to background streaming is given by:

$$\boldsymbol{u}_p\left(\boldsymbol{r}, \bar{\boldsymbol{r}}, t\right) = \boldsymbol{u}_p^f\left(\boldsymbol{r}, \bar{\boldsymbol{r}}, t\right) + \boldsymbol{u}_p^\gamma\left(\boldsymbol{r}, \bar{\boldsymbol{r}}, t\right), \tag{4.20a}$$

$$2\boldsymbol{\Omega}_p\left(\boldsymbol{r}, \bar{\boldsymbol{r}}, t\right) = \nabla \times \left[\boldsymbol{u}_p^f\left(\boldsymbol{r}, \bar{\boldsymbol{r}}, t\right) + \boldsymbol{u}_p^\gamma\left(\boldsymbol{r}, \bar{\boldsymbol{r}}, t\right)\right], \tag{4.20b}$$

where $\boldsymbol{u}^f$ and $\boldsymbol{u}^\gamma$ are given by (4.17) and (4.19). Note that the velocity (vorticity) field at the position of propeller n, which in turn determines $\boldsymbol{f}_n$ or $\boldsymbol{\gamma}_n$, is the sum of contributions from all other propellers:

$$\boldsymbol{u}_n = \sum_{k=1,k\neq n}^{4} \left(\boldsymbol{u}_k^f + \boldsymbol{u}_k^\gamma \right), \quad 2\boldsymbol{\Omega}_n = \nabla \times \boldsymbol{u}_n, \tag{4.21}$$

where $2\boldsymbol{\Omega}_n$ is the vorticity field at the center of disk n. The force-free ($\sum_{k=1}^{4} \boldsymbol{f}_k = 0$) and torque-free ($\sum_{k=1}^{4} (\boldsymbol{r}_k \times \boldsymbol{f}_k + \boldsymbol{\gamma}_k) = 0$) conditions in low-Reynolds-number regime, combined with velocity and vorticity fields presented in (4.21), provide us with a closed system of thirty coupled equations and thirty unknowns that must be solved at each time step. Integrating linear and angular velocities in time, using RK78 method [65], will then provide the swimmer's position and orientation as a function of time.

4.3 Results and Discussion

In our numerical experiments, the model swimmer is launched toward the wall with various incidence angles θ_{in} (c.f. Fig. 4.1b). Scattering angle θ_{out} corresponding to each θ_{in} is then measured with respect to the normal vector to the solid boundary after steady state is reached. We show samples of behavior of the micro-swimmer for $\theta_{in} = 0^o$, 5^o, 15^o, 30^o, 60^o, and 85^o in figure 4.2, in which the trajectory of the swimmer is shown by a black dashed line, chassis of the swimmer is denoted by a black thick bar, and the blue (red) filled circles represents propellers initially on the left (right) side of the swimmer. Without even touching the wall, the swimmer feels the solid wall in all cases, and escapes the boundary similar to what has been observed experimentally for a *C. reinhardtii* cell [58, 59]. Note that sensing and escaping the boundary here is purely hydrodynamic, as there is no contact/flagellar force defined for the model swimmer.

The only exception in which the swimmer feels the boundary but cannot escape it, happens when a swimmer approaches the wall with $\theta_{in} = 0$ (i.e. exactly normal to the wall). As theoretically required by the symmetry of our ideal numerical experiment, for $\theta_{in} = 0$ the swimmer can not choose any direction over the other one. For a typical puller-type swimmer, far-field analysis predicts a head-on collision with the wall for this situation. But, here the swimmer has a complex oscillatory flow field in its close vicinity, which saves it from hitting the wall. Surprisingly, the swimmer stops swimming forward after getting close enough to the boundary (Fig. 4.2a). This state is, in fact, a *dynamic* equilibrium: the swimmer is still struggling to swim forward with exactly the same stroke cycle as before and energy is getting wasted continuously through the propellers, but the time-averaged position of its geometric center has come to a halt . Note that on very short length scales, there is an intrinsic oscillation in the trajectory of the model swimmer that originates from the oscillatory nature of its flow field. These small-amplitude ($\Delta Z/a \approx 0.1$) up-and-down oscillations (also reported for swimming *C. reinhardtii* cells as the '*zigzagging motion*' [66])

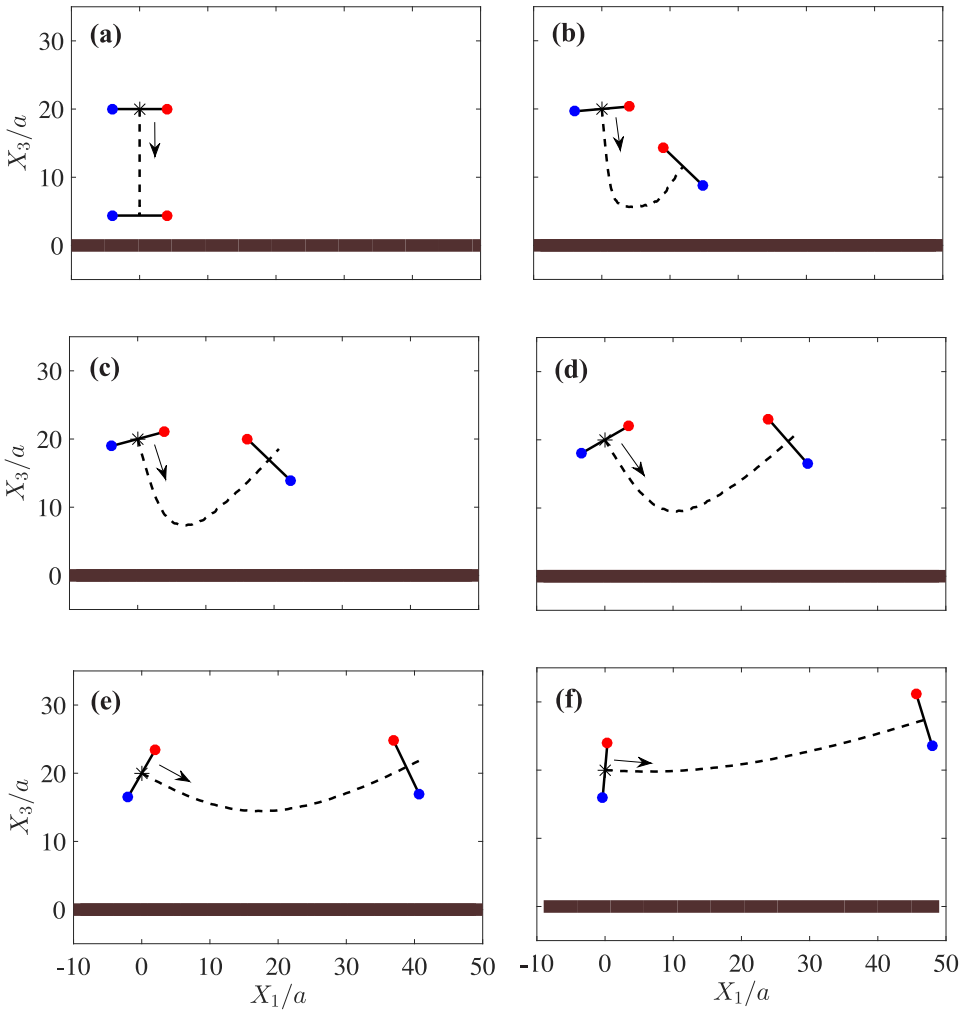

Figure 4.2: Samples of the hydrodynamic sensing and escaping behavior of micro-swimmers swimming near a solid boundary (denoted by the thick brown solid line at $X_3 = 0$). The swimmers initially swim toward the wall with different incidence angles: $\theta_{in} = 0^o$ (a), 5^o (b), 15^o (c), 30^o (d), 60^o (e), and 85^o (f). The initial and final (after scattering) states of each case are shown. In each panel, the black thick bar represents the swimmer's body (c.f. Fig. 4.1a), trajectory of the swimmer is shown by a dashed line, the start points are denoted by asterisks, and arrows represent the initial direction.

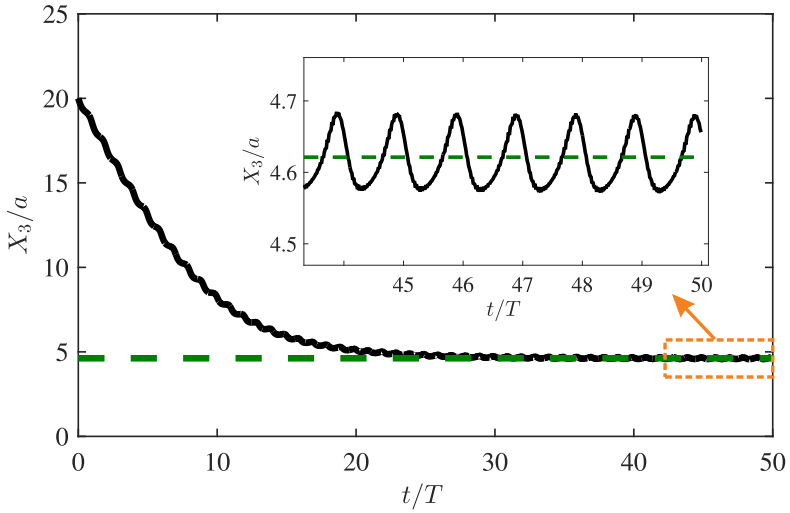

Figure 4.3: Time variation of the vertical position of a model swimmer approaching the wall with $\theta_{in} = 0$, i.e. exactly normal to the wall. Inset is the zoomed view of the tail, which represents the very small-amplitude up-and-down oscillations.

will still be present in the dynamic equilibrium phase (see the inset of figure 4.3). However, there will be no net translation over time for the swimmer in this phase (see Fig. 4.3).

To gain a better insight into the hydrodynamic scattering process, we also present (in figure 4.4) snapshots of the flow field generated by the model micro-swimmer launched toward the wall with $\theta_{in} = 30^o$. The flow field and its corresponding streamlines are denoted in the panels by purple arrows and green solid lines respectively. As the swimmer approaches the wall, the induced flow field and the generated vortices gradually rotate the swimmer and turn it away from the wall (see Fig. 4.4). This enables the swimmer to scatter off the solid boundary without physically touching the wall.

Hydrodynamic scattering of our model micro-swimmer presented in the space of (θ_{out}, θ_{in}), is in a good agreement with recent set of experimental data reported [59] on scattering of a real wild-type *C. reinhardtii* cell from a solid boundary (see figure 4.5). The only expected exception happens at $\theta_{in} = 0$ for which a perfect normal incidence (numerically easily achievable) results in a dynamic equilibrium, whereas such equilibrium has not been reported in the experiments, clearly due to extremely low probability of actual microorganisms approach the wall at the exact zero angle, and in a perfectly symmetric setup.

The numerical results presented in figure 4.5 correspond to the case of $c_0 = 50$ which is reminiscent of the flagellar beat frequency of green alga *C. reinhardtii*. Our numerical experiments show that the scattering behavior of the model swimmer will remain the same for different values of c_0. Changing the value of c_0 will only change swimming speed of the swimmer, and thus the time required for its scattering. The swimmer's scattering angle

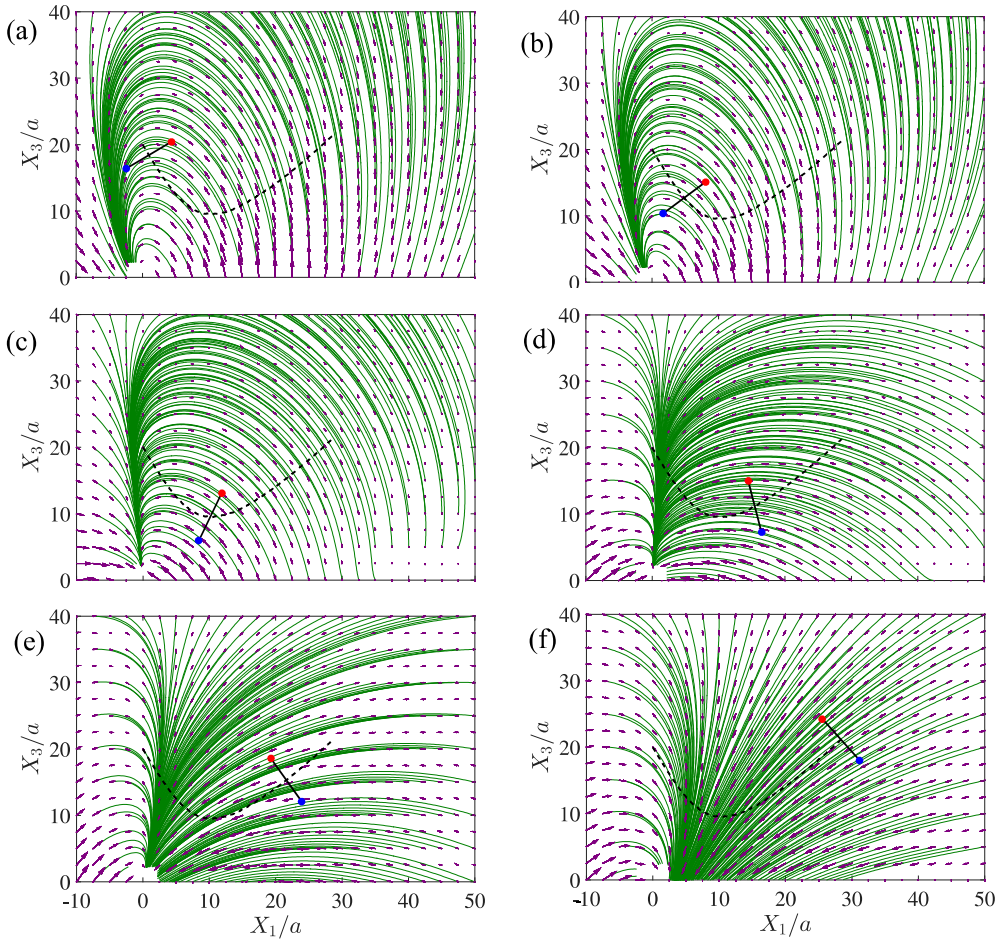

Figure 4.4: Snapshots of the flow field generated by the model swimmer during scattering process off a solid boundary. The incidence angle is $\theta_{in} = 30^o$ and panels correspond to $t = T$ (a), $5T$ (b), $10T$ (c), $15T$ (d), $20T$ (e), and $25T$ (f). Purple arrows represent the flow field, and green solid lines demonstrate the corresponding streamlines. Trajectory of the swimmer during $t \in [0\ ,\ 25T]$ is shown by a black dashed line, chassis of the swimmer is denoted by a black thick bar, and the blue (red) filled circles represents propellers initially on the left (right) side of the swimmer.

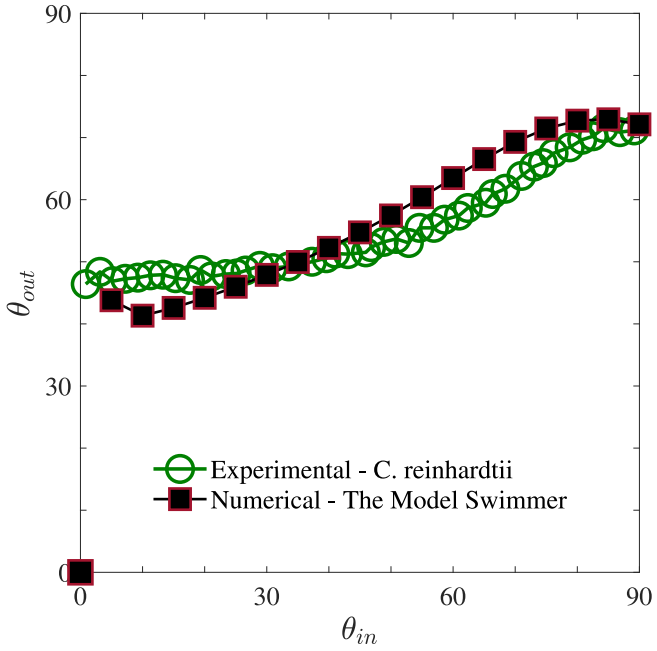

Figure 4.5: Comparison between the scattering angles (θ_{out}) resulted from purely hydrodynamic numerical simulations of the model micro-swimmer (black filled squares), and the experimental data (green circles) reported by Contino et al. [59] for wild-type *C. reinhardtii* cells. The scattering angles are presented in degrees.

(θ_{out}) and its minimum distance (d_{min}) from the wall, as a function of its incidence angle (θ_{in}), are presented in figure 4.6(a) for different values of c_0. The results further confirm similarity of the behavior for swimmers with different propeller speeds. A similar effect has been also reported for amoeboid swimmers [56, 67], where swimming stroke frequency does not change the navigation behavior.

Moreover, in the presented numerical experiments throughout this chapter, we have considered (as a benchmark) a model swimmer with $s_m/a = 2$ so that $a = 1\ \mu m$ provides us with the body size of $8 - 12\ \mu m$ similar to that of a *C. reinhardtii* cell [68]. To explore the effect of body size on the scattering behavior of the swimmer, figure 4.6(b) represents the scattering angles (θ_{out}) and minimum distances from the wall (d_{min}) of swimmers with different values of s_m. Qualitative and quantitative similarity of the scattering results observed for swimmers with different values of s_m, further highlights the primary role of flow characteristics (i.e. oscillatory nature of the flow combined with side, posterior, and anterior vortices) rather than body size of the swimmer.

Lastly, we also present the scattering results of the swimmer when launched toward the boundary with different initial distances (h_0) from the wall (figure 4.6c). Note that by increasing the incidence angle (θ_{in}), the effect of initial distance becomes more clear. In its extreme case, for $\theta_{in} = 90^o$ (i.e. when the model swimmer initially swims parallel to the

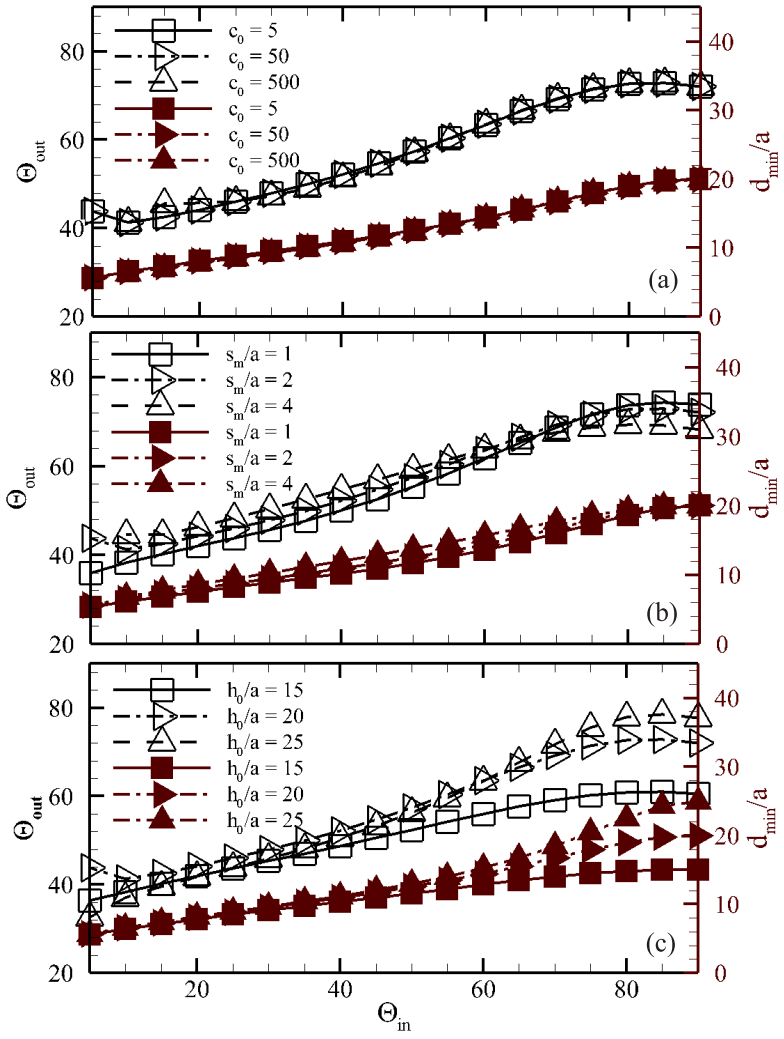

Figure 4.6: Exploring the parameter space for the model micro-swimmer's surface scattering process. In particular, here the scattering angle (θ_{out}) of the model micro-swimmer and its minimum distance (d_{min}) from the wall are presented as a function of the swimmer's incidence angle (θ_{in}), its propulsion characteristics (a-b), and its initial distance from the wall (c). The black (brown) axis on the left (right) measures the scattering angles (minimum distances from the wall). For each incidence angle, the scattering angle (minimum distance from the wall) of the swimmer is shown by a black unfilled (brown filled) square, right-triangle, and up-triangle for: (a) $c_0 = 5$, 50, and 500, respectively; (b) $s_m/a = 1$, 2, and 4, respectively; and (c) $h_0/a = 15$, 20, and 25, respectively. The reference case (as also presented in Fig. 4.5) corresponds to $c_0 = 50$, $s_m/a = 2$, and $h_0/a = 20$.

wall) the minimum distance is equal to h_0 itself, which here ie set to different values. As we get closer to the other extreme (i.e. swimming normal to the wall), quantitative difference between the results fades out both for the case of scattering angles and minimum distances from the wall (see figure 4.6c).

4.4 Concluding Remarks

In this chapter, we demonstrated how inducing a complex oscillatory flow field (with anterior, side, and posterior vortices) can be a sufficient tool for micro-swimmers to sense and escape solid boundaries. The presented findings provide a new insight into the cell-surface scattering process. Specifically, the results of our investigation point out the possibility of a purely hydrodynamic surface-scattering for bi-flagellate green algae, *C. reinhardtii*, in agreement with recently reported experimental studies [e.g. 59]. Our findings may also pave the path for new techniques in controlling biological migration, for which many potential applications (including diagnostics [50], drug delivery [69], and bio-remediation [70]) can be sought.

Acknowledgments

This work was supported by the National Science Foundation grant CMMI-1562871.

Chapter 5

Stealthy Movements and Concealed Swarms

In this chapter, we show that micro-swimmers can form a *concealed* swarm through synergistic cooperation in suppressing one another's disturbing flows. We then demonstrate how such a concealed swarm can actively gather around a favorite spot, point toward a target, or track a desired trajectory in space, while minimally disturbing the ambient fluid. Quenching the flow signature (and thus shrinking the associated detection region) by swarming in concealed modes, can potentially have a significant impact on trophic transfer rates among a broad range of aquatic organisms. The findings presented in this chapter provide a clear road map to control and lead flocks of swimming micro-robots in *stealth* versus *fast* modes, tuned through their active collaboration in minimally disturbing the host medium.

5.1 Introduction

Swimming micro-robots capable of navigating through fluid environments are at the forefront of minimally invasive therapeutics and theranostics [18]. They hold great promise for a wide range of biomedical applications including targeted drug delivery, micro-surgery, remote sensing and localized diagnostics [18, 71, 72]. The past decade has seen a great leap forward in science and engineering of these miniaturized untethered robots [73]. Particularly, remarkable progress has been made toward exploring various propulsion mechanisms [74, 75, 76], design and fabrication approaches [77], imaging technologies for real-time motion tracking [78], and manipulation techniques for navigation and motion control [79, 80, 81].

However, *optimal* strategies in swarm control remain largely unexplored for swimming micro-robots [75]. As a result, little is understood about their potential ability as a *group* to optimize their fitness and functionality. A few recent studies have only shown a glimpse of such potentials in the realm of micro-scale swimmers. For instance, actively controlled cooperation between artificial micro-swimmers has been reported to significantly improve

(both the capacity and precision of) micro-manipulation and cargo transport [82]. It has also been recently shown [11] that a pair of interacting micro-swimmers can boost each other's swimming speed through ambient fluid. This observation (termed as 'hydrodynamic slingshot effect') implies that by forming a swarm, swimming micro-robots can collaborate and travel faster as a group than single individuals. Now, the more intriguing question is whether by forming a swarm, swimmers are also able to smartly cancel out each other's disturbing effects to the fluid environment. In other words, is it possible to form a stealth swarm minimally disturbing the ambient fluid? And if so, to what extent such cooperation between the agents can be effective in stifling the swarm's hydrodynamic signature?

In this chapter, a synergistic cooperation of micro-swimmers (in suppressing one another's disturbing flows) is unveiled, that leads to the formation of stealth swarms. We refer to this mode of swarming as the *concealed* mode, which can reduce the swarm's net induced disturbances by more than 99% (or 50%) in three-dimensional (or two-dimensional) movements. This is equivalent to quenching the swarm's hydrodynamic signature (and thus shrinking its associated detection region) by an order of magnitude in range. Through numerical experiments, it is then demonstrated how such a concealed swarm can actively gather around a favorite spot, point toward a target, or track a desired trajectory in space, whilst minimally disturbing the surrounding environment.

5.2 Problem Formulation and Approach

Dynamics of the incompressible flow around swimming objects is governed by the Navier-Stokes equations:

$$\rho \frac{D\boldsymbol{u}}{Dt} = -\nabla P + \eta \, \nabla^2 \boldsymbol{u} + \boldsymbol{F}, \quad \nabla \cdot \boldsymbol{u} = 0, \tag{5.1}$$

subject to boundary conditions imposed by their body deformations. Here, ρ and η are density and dynamic viscosity of the surrounding fluid, P denotes the pressure field, $\boldsymbol{u}$ is the velocity field, and $\boldsymbol{F}$ represents the external body force per unit volume. The relative importance of inertial to viscous effects can also be quantified by the Reynolds number, Re= ρUL/η, where U and L denote characteristic velocity and length, respectively. For micro-scale swimmers (also known as *micro-swimmers*) swimming in water ($\rho \approx 10^3$ kg/m^3 and $\eta \approx 10^{-3}$ Pa.s) the corresponding Reynolds number is always very small (i.e., Re $\ll 1$). Common examples include: (i) typical bacteria, such as *Escherichia coli*, with length of $\sim$ 1-10 μm and swimming speed of $\sim$ 10 μms^{-1} [83], for which the Reynolds number is $\sim$ 10^{-5}-10^{-4} when swimming in water; or (ii) the green algae *Chlamydomonas reinhardtii* with characteristic length L $\sim$ 10 μm and swimming speed U $\sim$ 100 μms^{-1} [68], which result in the Reynolds number Re $\sim 10^{-3}$. Thereby, it is appropriate to study micro-swimmers in the context of low Reynolds number regimes (Re $\ll 1$), where the fluid inertia is negligibly small compared to the fluid viscosity, and the viscous diffusion dominates fluid transport.

The Navier-Stokes equations then simplify to the Stokes equation:

$$\nabla P = \eta \, \nabla^2 \boldsymbol{u} + \boldsymbol{F}, \quad \nabla \cdot \boldsymbol{u} = 0, \tag{5.2}$$

which has no explicit time-dependency. This along with its linearity, makes the Stokes equation invariant under time-reversal. As a result, sequence of body deformations (or swimming strokes) that are reciprocal (i.e. invariant under time-reversal), do not generate a net motion at Stokes regime. This means that typical swimming strategies used by larger organisms (e.g. fish, birds, or insects), are not effective at micro- and nano-meter scales. Therefore, motile microorganisms have evolved alternative propulsion mechanisms to break the time-symmetry, while retaining periodicity in time [6]. Their swimming strategies are often based on drag anisotropy on a slender body in Stokes regime, and include cork-screw propulsion of bacteria, flexible-oar mechanism of spermatozoa, and asymmetric beats of bi-flagellate alga [6].

These inherently available natural micro-swimmers, not only inspire the design of fully synthetic micro-robots [75], but also may be functionalized and directly used as steerable swimming micro-robots [76]. Bio-inspired micro-robots are artificial swimmers that mimic the propulsion mechanism of their natural counter-parts [75]. For instance, the artificial flagellate magnetic micro-robots [84, 9] adopt the helical tail of *E. coli* bacteria and mimic their cork-screw propulsion mechanism. These synthetic swimming robots are capable of programmed trajectory-tracking with micrometer-level precision [84]. In the bio-hybrid approach, on the other hand, a real swimming microorganism is modified with artificial parts to be used as a remotely controllable micro-robot [76]. Common designs employ *E. coli* bacteria [85], spermatozoa [86], or green algae *C. reinhardtii* cells [87]. Here we are interested in *flocks* of such bio-inspired and bio-hybrid swimming micro-robots, where each agent is either a real microorganism or meticulously synthesized to mimic one. Therefore, to model their induced disturbances, we will treat each individual swimmer as a swimming microorganism.

In Stokes regime, self-propelled buoyant micro-swimmers exert no net force and no net torque to the ambient fluid. Flagellated microorganisms, for instance, use their flagella – flexible external appendages – to generate a net thrust, and propel themselves through ambient fluids. This propulsive force – generated mainly owing to the drag anisotropy of slender filaments in Stokes regime [88] – is, however, balanced by the drag force acting on the cell body (see e.g. Fig. 5.1). Hence, in the most general form, far-field of the flow induced by each micro-swimmer can be well described by the flow of a force dipole. To be more precise, by the flow of a force dipole composed of the thrust force generated by swimmer's propulsion mechanism, and the viscous drag acting on its body. Note that the model dipole is contractile for swimmers with front-mounted flagella (i.e., 'pullers' such as *C. reinhardtii*), and extensile for those with rear-mounted flagella (i.e., 'pushers' such as *E. coli*). Schematic representations of the force dipoles generated by archetypal puller and pusher swimming microorganisms, as well as direction of the induced flow fields are shown in Fig. 5.1. This simple model has been validated and widely used in the literature [89, 26]. In the case of *E. coli* bacteria, for example, the validity of this model has been further

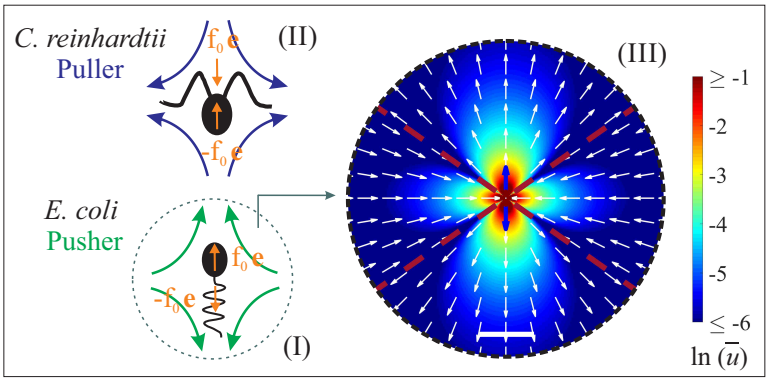

Figure 5.1: Schematic representation of archetypal pusher (panel I) and puller (panel II) micro-swimmers. Forces exerted by each swimming microorganism to the ambient fluid are represented ($\pm f_0 \boldsymbol{e}$ shown in orange), and induced flow directions are shown by curly arrows. The flow field induced by an extensile force dipole (as a model for pushers) is presented in panel (III), where color shading represent the magnitude and white arrows show direction of the induced flow field. Inward and outward flows are separated for the flow field presented in panel (III) by $y = \pm 1/\sqrt{2}\ x$ red dashed lines. The scale bar denotes $10L_s$.

confirmed by comparing it to the flow field experimentally measured around an individual swimming cell [90].

Let us consider a model micro-swimmer swimming toward direction $\boldsymbol{e}$, through an unbounded fluid domain. Disturbing flow induced by the swimmer can be modeled as the flow of a force dipole located at instantaneous position of the swimmer ($\boldsymbol{x}_0$). Thrust and drag forces of equal magnitude are exerted in opposite directions ($\pm f_0 \boldsymbol{e}$) to the ambient fluid at $\boldsymbol{x}_0 \pm \boldsymbol{e}\ l/2$, where the characteristic length l is on the order of swimmer dimensions. For each point force $\boldsymbol{f}$ exerted at point $\boldsymbol{x}_p$ in an infinite fluid domain, the governing equation will turn into:

$$\nabla P = \eta\ \nabla^2 \boldsymbol{u} + \boldsymbol{f}\delta(\boldsymbol{x} - \boldsymbol{x}_p), \quad \nabla \cdot \boldsymbol{u} = 0. \tag{5.3}$$

where $\delta(\boldsymbol{r})$ is the Dirac delta function. Equation (5.3) can be analytically solved in several ways [44], and the resultant velocity field is known as Stokeslet:

$$\boldsymbol{u}_S(\boldsymbol{r}_p, t) = \frac{\boldsymbol{f}}{8\pi\eta}\left(\frac{\boldsymbol{I}}{r_p} + \frac{\boldsymbol{r}_p \boldsymbol{r}_p}{r_p^3}\right) \equiv \boldsymbol{G} \cdot \boldsymbol{f}, \tag{5.4}$$

where $\boldsymbol{r}_p = \boldsymbol{x} - \boldsymbol{x}_p$, and $\boldsymbol{G}$ is the corresponding Green's function. A complete set of singularities in Stokes regime, can then be obtained [44] by taking derivative of the fundamental solution presented in (5.4). The induced flow field of a model force dipole, $\pm f_0 \boldsymbol{e}$, located at

instantaneous position of the swimmer ($\boldsymbol{x}_0$), can therefore be mathematically expressed as:

$$\boldsymbol{u}_{\mathrm{SD}} = \frac{\mathscr{D}}{8\pi\eta\, r^3}\left[-1+3\left(\frac{\boldsymbol{r}\cdot\boldsymbol{e}}{r}\right)^2\right]\boldsymbol{r}, \tag{5.5}$$

where $\boldsymbol{r} = \boldsymbol{x} - \boldsymbol{x}_0$, for any generic point $\boldsymbol{x}$ in space. Note that the dipole strength, $\mathscr{D} \approx f_0 l$, has a positive (negative) sign for pusher (puller) swimmers and its value can be inferred from experimental measurements. For instance, the values of $f_0 = 0.42$ pN and $l = 1.9$ μm, have been experimentally obtained [90] for E. coli, in agreement with resistive force theory [83], and optical trap measurements [91].

Here, we use velocity scale $U_s = f_0/8\pi\eta l$, length scale $L_s = l$, and time scale $T_s = L_s/U_s$, to non-dimensionalize the reported quantities. Therefore, dimensionless disturbing flow induced by a micro-swimmer reads as:

$$\bar{\boldsymbol{u}}_{\mathrm{SD}} = \frac{c_0}{\bar{r}^3}\left[-1+3\left(\frac{\bar{\boldsymbol{r}}\cdot\boldsymbol{e}}{\bar{r}}\right)^2\right]\bar{\boldsymbol{r}}, \tag{5.6}$$

where $c_0 = +1$ (-1) for pushers (pullers) and bar signs denote dimensionless quantities. It worths noting that near-field of the flow induced by a micro-swimmer can be described more accurately via including an appropriately chosen combination of higher order terms from the multipole expansion [e.g. 92, 93]. However, here we are interested in the *span* of swimmers' induced disturbances and their consequent detection region, for which far-field of the flow is of primary interest.

To assess optimality of various swarm arrangements (in stifling disturbing effects), one needs to first quantify the induced fluid disturbances. A measure of distortion (caused by a flock of swimmers to the ambient fluid) can be obtained [14] by directly computing the Mean Disturbing Flow-magnitude (MDF) over a surrounding ring ($\mathcal{C}$) of radius R, i.e.

$$\mathrm{MDF} = \frac{1}{2\pi\bar{R}}\oint_{\mathcal{C}} |\bar{\boldsymbol{u}}_{\mathrm{net}}|\mathrm{ds}, \tag{5.7}$$

where $\bar{R} = R/L_s$, and $\bar{\boldsymbol{u}}_{\mathrm{net}}$ is the overall dimensionless flow field induced by the flock. Due to linearity of the Stokes equation (5.2), the net disturbing flow ($\bar{\boldsymbol{u}}_{\mathrm{net}}$) is computed through superposition of the flow fields ($\bar{\boldsymbol{u}}_{\mathrm{SD}}$) induced by individual swimmers forming the flock (i.e. $\bar{\boldsymbol{u}}_{\mathrm{net}} = \sum_{i=1}^{N} \bar{\boldsymbol{u}}^i_{\mathrm{SD}}$). Alternatively, one can quantify swarm's induced fluid disturbances by computing *Area of the Detection Region* (ADR), within which disturbances exceed a predefined threshold. More precisely, the detection region refers to the subset of space, within which the magnitude of net induced disturbing flow ($\bar{\boldsymbol{u}}_{\mathrm{net}} = \boldsymbol{u}_{\mathrm{net}}/U_s$) exceeds a predefined threshold ($\bar{u}_{\mathrm{th}} = u_{\mathrm{th}}/U_s$), i.e.

$$\mathscr{R} = \left\{\forall \boldsymbol{x} :\ |\bar{\boldsymbol{u}}_{\mathrm{net}}(\boldsymbol{x})| \geq\ \bar{u}_{\mathrm{th}}\right\}, \tag{5.8}$$

which is also consistent with previous numerical studies on swimming microorganisms [94]. The threshold value (u_{th}) can be tuned based on characteristics of the specific problem of interest. For the system representing a prey swarm, as an example, it can be inferred from experimental observations on sensitivity of predators' receptors in sensing flow signatures.

5.3 Results and Discussion

Here, the described theoretical analysis is combined with direct computations and non-linear optimization, to perform a systematic parametric study on flocks of $N \geq 2$ swimmers with a bottom-up approach. Specifically, we develop a general procedure to determine optimal swarming configurations, and systematically investigate their significance in reducing the swarm's induced fluid disturbances. We then present computational evidences demonstrating how such a concealed swarm can actively gather around a favorite spot, point toward a target, or track a desired trajectory, while minimally disturbing the ambient fluid. As a benchmark, here we consider planar arrangements/movements of pusher swimmers (say, *E. coli* bacteria) in an infinite fluid domain. Nevertheless, the reported concealed arrangements will be the same for pullers, and our study can be inherently extended to three-dimensional (3D) scenarios (see section 5.4.1 for details).

5.3.1 Concealed Arrangements

Let us consider simple groups of only two and three swimmers. The relative orientation of the swimmers primarily controls the amount of distortion (measured in terms of MDF/ADR) they induce to the surrounding environment. Our results reveal that by swimming in optimal orientations, swimmers can reduce their induced disturbances by more than 50% (Fig. 5.2) compared to when they simply swim in schooling orientations (i.e. toward the same direction). In fact, there exist a *range* of optimal swarm configurations, arranging into which will result in minimally disturbing the surrounding fluid. For instance, when two of the agents (in a group of three) swim in directions normal to each other, the swarm arrangement remains optimal regardless of the third one's swimming direction (see the green dashed line in Fig. 5.2b). This is due to axisymmetric nature of the disturbing flow induced by two perpendicular dipoles (Fig. 5.2a-II). It bears attention that computed values of induced disturbances (in terms of ADR/MDF) vary depending on associated hyper-parameters – specifically, the threshold value ($\bar{u}_{th}$) considered in computing ADR, or the radius (R/L_s) of surrounding ring over which MDF is computed. However, such dependencies can be avoided by normalizing the computed values against MDF/ADR induced by a reference swarm arrangement (see e.g. Fig. 5.2a). The consequent normalized values also represent a cross-match for MDF versus ADR (Fig. 5.2a). This further confirms equivalence of the described measures in assessing optimality of swarm arrangements.

For groups including a larger number of swimmers (i.e. those with $N > 3$ agents), plotting MDF (or ADR) over the entire parameter-space is not practical. However, we know that any flock of $N \in \{4, 5, \ldots\}$ swimmers can be divided into sub-groups of only two or three agents. For each of such sub-groups, the optimal region configurations is then readily available (Fig. 5.2), assuring about 50% reduction of induced disturbances. This along with linearity of Stokes equations (5.2), which describes dynamics of the flow around micro-swimmers, guarantee the existence of optimal swarm arrangements with the same 50% concealing efficiency. Therefore, the optimal region of configurations exists for any flock

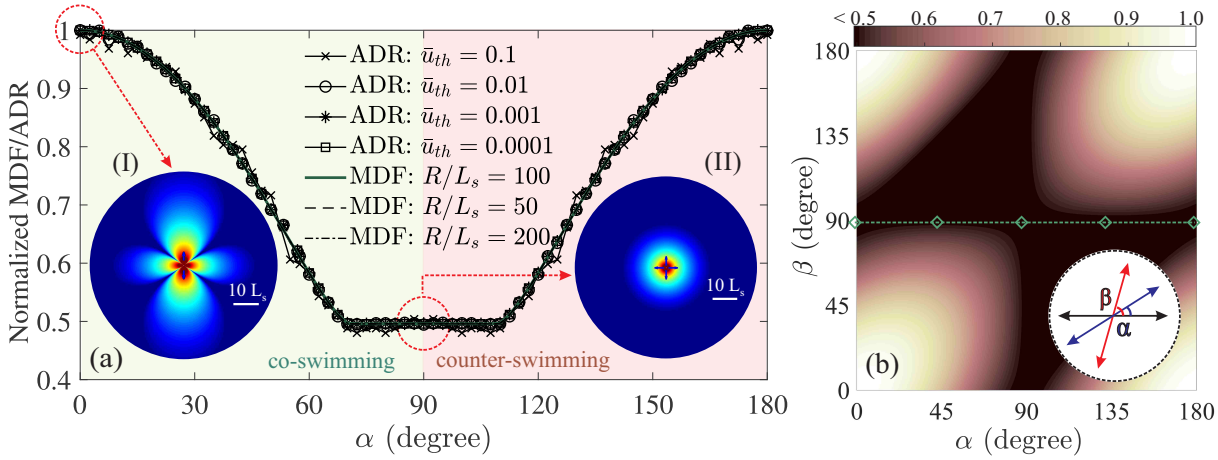

Figure 5.2: **(a):** Fluid disturbances induced by a group of two swimmers are measured in terms of MDF/ADR, and plotted as a function of relative angle between the agents (α). Values presented in each plot are normalized by their maximum, which corresponds to the reference case of aligned swimmers (i.e. in schooling arrangement). We also compare normalized values of MDF computed over surrounding rings of various radii, specifically $R/L_s = 50$, 100, and 200. Similarly, the process of computing ADR has been repeated for different threshold values. Specifically we present those corresponding to $\bar{u}_{th} = 0.1$, 0.01, 0.001, and 0.0001. Insets: Magnitude of the flow induced by two micro-swimmers swimming in parallel (I) or perpendicular (II) directions. **(b):** Fluid disturbances (in terms of MDF) induced by a group of three swimmers is presented by color shading over the space of relative angles (defined as α and β) between them. The values are computed over a surrounding ring of radius $R/L_s = 100$, and then normalized by the reference case (i.e. their maximum value). The green dashed-line highlights the set of all possible arrangements with $\beta = 90^o$. Inset schematically defines α and β.

of N swimmers, and one can extract an optimal arrangement by implementing non-linear optimization over the parameter-space. Note that objective functions quantifying swarm's induced disturbances (i.e. MDF/ADR), are nonlinear and often subject to constraints (e.g. minimum separation distance between the agents). Thereby, in search of the global minima by starting from multiple points, here we perform sequential quadratic programming using local gradient-based solvers.It worths mentioning that merely applying gradient-based solvers will only find local optima, depending on the starting point. To avoid this, here the starting points are generated using a scatter-search mechanism [95], which is a high-level heuristic population-based algorithm, designed to intelligently search on the problem domain. Its deterministic approach in combining high-quality and diverse members of the population – rather than extensive emphasis on randomization – makes it faster than other similar evolutionary mechanisms, such as genetic algorithm [96].

As a benchmark, magnitude of the disturbing flow induced by a random suspension of

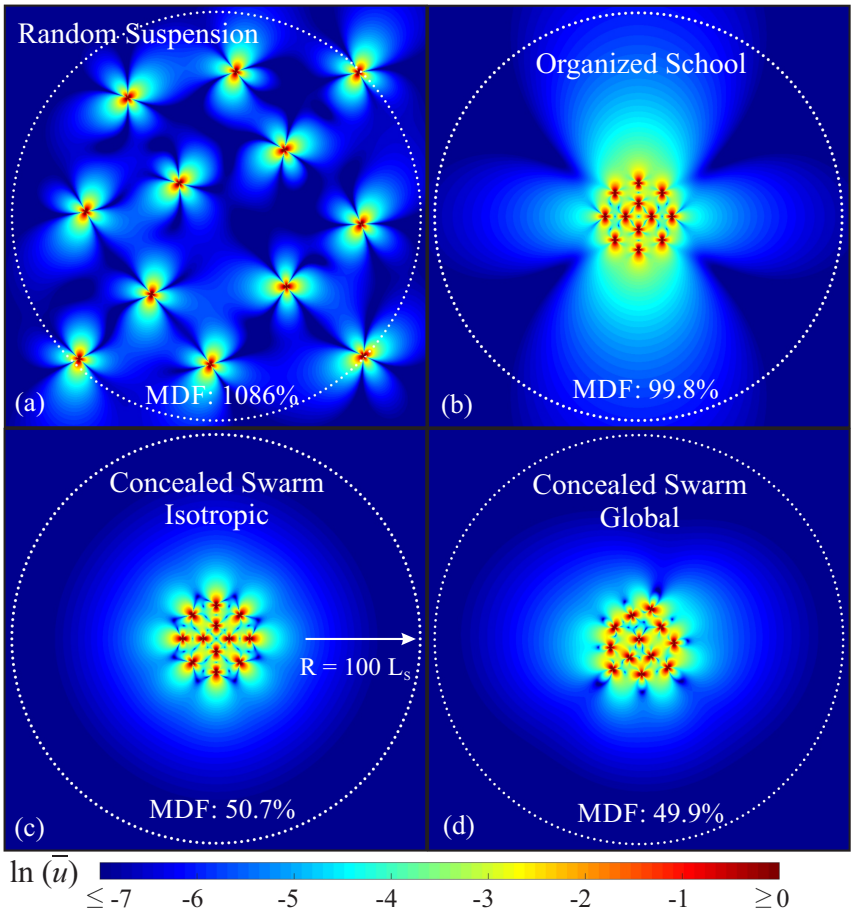

Figure 5.3: Magnitude of the disturbing flows induced by a randomly arranged suspension of twelve swimmers (a), is compared to when they form a structured group and arrange into an isotropic arrangement with schooling orientation (b), or concealed swarms (c-d). The minimum separation distance (ξ) between the swimmers in all cases is set to $10L_s$. Note that positions of the swimmers in panel (b) are the same as those in panel (c). The only difference is that swimmers are arranged into the schooling orientation in (b), whereas the isotropic arrangement in (c) is a particular example from the infinite pool of concealing arrangements (i.e. the optimal region of configurations). For a swarm of twelve swimmers with minimum separation distance of $\xi/L_s = 10$, panel (d) represents arrangement of the globally optimal swarm with minimal disturbing effects. Color shading represents the flow magnitude, and MDF is computed over white dotted rings (with radius $R/L_s = 100$). The reference case used to normalize reported MDF values, corresponds to the case of twelve aligned swimmers all located at the center point.

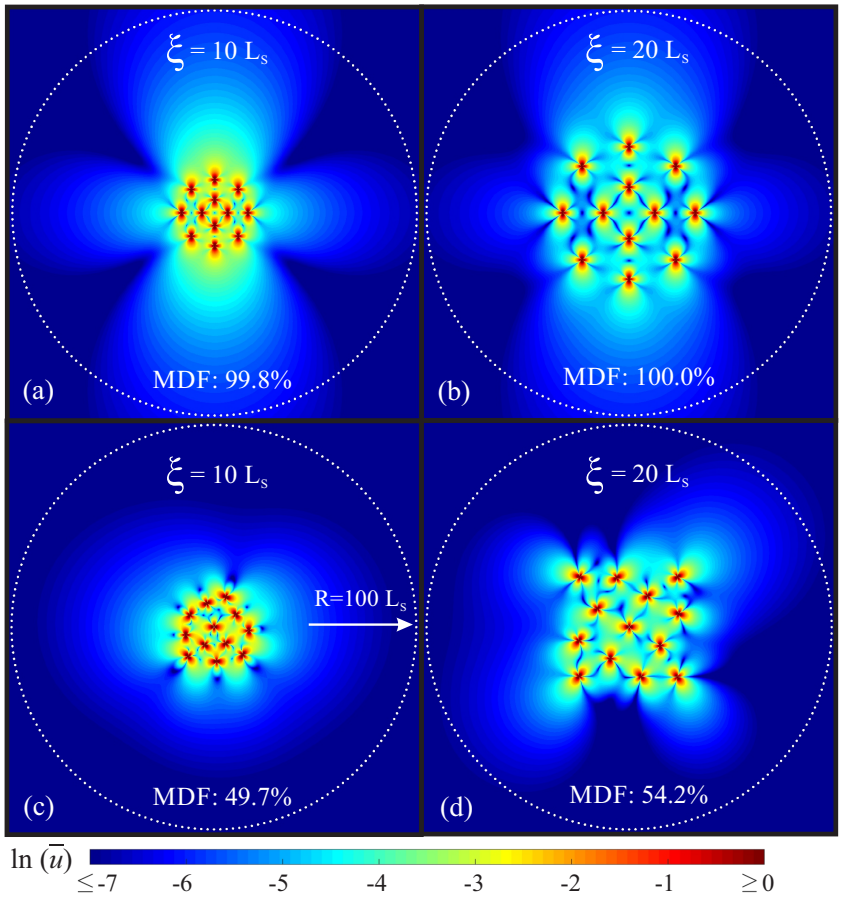

Figure 5.4: (a)-(b): Magnitude of the net disturbing flows induced by a flock of twelve swimmers schooling in an isotropic positioning with minimum separation distance $\xi/L_s = 10$ and 20 between them. (c)-(d): Magnitude of the net disturbing flows induced by concealed swarms of twelve swimmers with minimum separation distance $\xi/L_s = 10$ and 20, respectively. Here the reported values of MDF are computed over the white dotted rings (with radii $R/L_s = 100$), and normalized against the reference case. Color shading represents the net disturbing flow magnitudes in each panel.

twelve swimmers, and the one induced by the same group arranged into an isotropic organized school are compared in Fig. 5.3, to that induced by concealed swarms of twelve swimmers. It worth noting that the amount of disturbances induced by a flock of swimmers depends also on the minimum separation distance between the agents. Our numerical results show that the role of this factor is more significant for a concealed swarm than for an organized school (see e.g. Fig. 5.4). However, it can still be considered as a minor factor compared to relative orientation of the swimmers.

5.3.2 Concealed Swarming

There exist many situations (for both motile microorganisms and swimming micro-robots) that swimmers form an active swarm (i.e. a disordered cohesive gathering) around a desired spot. For instance, this can be a swarm of bacteria around a nutrient source [97], or a flock of biological micro-robots performing a localized micro-surgery [18, 98]. Remaining concealed in these scenarios can keep a bacterial swarm stealth from nearby predators, or help keeping a deployed flock of micro-robots non-disturbing to the host medium.

Note that forming a swarm (as opposed to a random suspension), by itself, keeps the net induced distortions bounded (see e.g. Fig. 5.3). However, to have *minimal* disturbing effects, arrangement of the swimmers (forming a swarm) must lie within the optimal region of configurations at every instant of time. To this end, we choose the proposed measure of net induced disturbances (i.e. MDF) as the objective function ($\mathcal{Z}$) to be minimized by the swarm arrangement. Dynamics of an active *concealed* swarm can then be described as follows: (i) swimmers forming the swarm get into an optimal arrangement (with minimal fluid disturbances); (ii) each swimmer then swims steadily forward (i.e. 'runs') for a fixed period of time (say, τ_r); (iii) the swimmers will then reorient quickly (i.e. 'tumble') into a new optimal arrangement, and then (iv) start running once again toward the new directions. This sequence of events occur in turn, repeatedly. Parameters including swimming speed and frequency of tumbling events (τ_r^{-1}) can be tuned according to the system of interest. As a benchmark, here we present a sample time evolution of an active concealed swarm in Fig. 5.5. Through the above described dynamics, the swarm remains cohesive, keeps itself confined within a finite region of space (around a desired spot), and is able to stifle the induced disturbances by $\sim 50\%$ through system evolution (Fig. 5.5). This is equivalent to shrinking the swarm's detection region by half.

It also worths mentioning that motion of each individual swimmer in the presented system, can be seen as a *controlled* version of the so-called *run-and-tumble* mechanism. This is inspired by the observed behavior of swimming microorganisms, such as E. coli bacteria – known as the paradigm of run-and-tumble locomotion [99]. Recent observations [100] reveal that even C. reinhardtii cells swim in a version of run-and-tumble. From a practical point of view, realization of the smart form of run-and-tumble mechanism also seems feasible in the context of internally/externally controlled artificial micro-swimmers. The recently proposed *Quadroar* swimmer [15, 12], for instance, propels (i.e. runs) on straight lines, and can perform full three-dimensional (3D) reorientation (i.e. tumbling) maneuvers [10].

5.3.3 Stealthy Maneuvers and Target Pointing

Through altruistic collaborations, micro-swimmers can also remain stealth while traveling toward a target point or tracking a desired trajectory in space. There is only one caveat here. The objective function ($\mathcal{Z}$), to be minimized by the traveling swarm during each consecutive run, must now represent a measure not only for the overall disturbances induced by the swimmers, but also their distances from the target point (or from the desired trajectory).

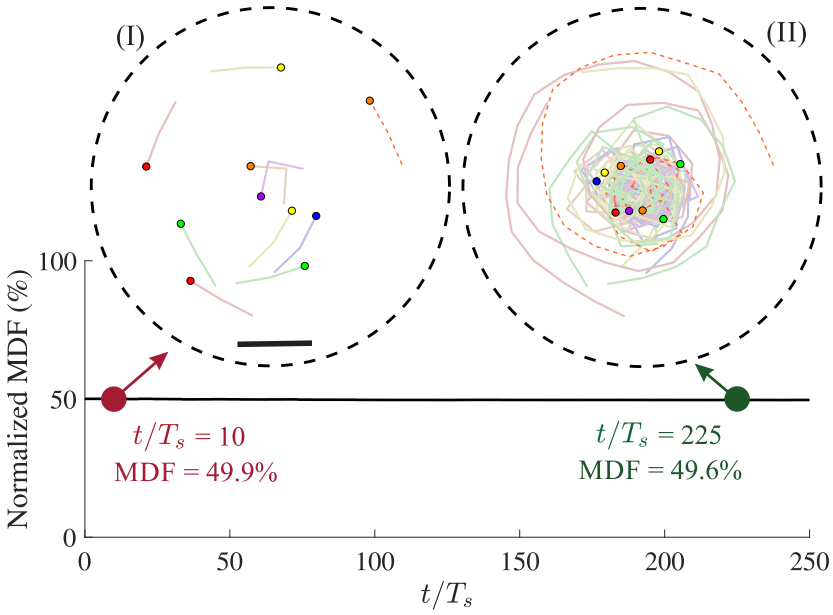

Figure 5.5: Fluid disturbances (in terms of MDF) monitored over the time evolution of an *active* concealed swarm of ten swimmers. The agents are initially positioned and oriented randomly (at $t/T_s = 0$). Thereafter, each agent represents a version of run-and-tumble dynamics (with $\tau_r/T_s = 5$), so that to keep the swarm's arrangement within the optimal region of configurations at every instant of time. The insets (I and II) represent snapshots of the swarm's activity at an early ($t/T_s = 10$) and late ($t/T_s = 225$) stages of the system evolution, respectively. The immediate values of MDF (computed over surrounding rings of radii $R/L_s = 100$) for the presented snapshots are 49.9% and 49.6%, respectively. In each panel, the instantaneous positions of the swimmers are marked with colored dots, and their trajectories are shown by gray-scale lines. As a benchmark, we have also highlighted one of the trajectories with an orange dashed-line. The presented scale bar is $10L_s$.

Therefore, we define

$$\mathcal{Z} = \epsilon \times \bar{\text{MDF}} + (1-\epsilon) \times \bar{\text{RMS}}_d \ , \tag{5.9}$$

where $\bar{\text{RMS}}_d$ stands for the normalized root mean square of swimmers' distances from the target point; $\bar{\text{MDF}}$ quantifies the overall induced disturbances; and $0 \leq \epsilon \leq 1$ is the detuning parameter which determines the importance of concealing versus travel time. Note that the ratio $\epsilon/(1-\epsilon)$ properly covers the entire span of $[0, \infty)$ when $\epsilon \in [0, 1)$. In practice, a variety of imaging techniques [78] can be used to feed back the state information (including swimmers' distance toward the target point) into the agents' decision-making unit. However, some bio-hybrid systems may rely on local (point-wise) sensing capabilities of swimming microorganisms (in measuring quantities such as light or chemicals) to obtain state information. To optimally control such systems, a more realistic objective function can be devised

(see section 5.4.2) by replacing $\bar{\text{RMS}}_d$ in Eq. (5.9) with $\bar{\text{RMS}}_\theta$. The latter stands for normalized root mean square of the swimmers' deviations from their locally desired directions, in the absence of concealing interests. Nevertheless, our numerical experiments reveal that the bottom-line of analysis conducted using such an alternative objective function still remains the same (Fig.5.9, section 5.4.2).

Sample flocks of micro-swimmers, controlled to travel from a starting point ($\mathscr{A}$) toward a target point ($\mathscr{B}$) in *stealth* versus *fast* modes (tuned by ϵ), are shown in Fig. 5.6. Note that $\epsilon = 0$ corresponds to the fastest traveling swarm, for which the swimmers travel in schooling arrangements (i.e. toward the same direction), but it provides no concealing benefits (i.e. MDF = 100% for $\epsilon = 0$). On the other extreme, i.e. for $\epsilon = 1$, the swarm will have the highest concealing efficiency (MDF = 49.7%), yet never reaches the target point (Fig. 5.6a). Trade-off between the travel time and the overall efficiency of concealing is demonstrated with more details in Fig. 5.6(c). To illustrate, we have monitored the induced fluid disturbances for traveling swarms controlled with various values of ϵ, during their migration from $\mathscr{A}$ to $\mathscr{B}$. As $\epsilon \to 1$ ($\to 0$), the swarm will travel slower (faster), yet induces less (more) disturbances to the ambient fluid. Recall that for a traveling swarm controlled by $\epsilon = 0$, the objective function (5.9) encodes only a measure of the swimmers' distances to the target point. This results in reaching the target point in minimum amount of time (Fig. 5.6a). However, once an $\epsilon > 0$ is introduced to the swarm control strategy, the objective function (to be minimized by the traveling swarm) will also include a measure for the swimmers' overall induced disturbances (in terms of MDF). Thereby, the fluid disturbance (measured in terms of normalized MDF) induced by a controlled traveling swarm, rapidly decays with ϵ and eventually converges to the highest possible concealing efficiency (i.e. MDF = 49.7%) at $\epsilon \approx 0.5$ (Fig. 5.6c). It is remarkable that swarming in such an optimally concealed mode (Fig. 5.6b), that is the fastest among those with highest possible concealing efficiency, costs only 23% increase in the trip duration compared to the fastest possible swarm. The associated concealing efficiency

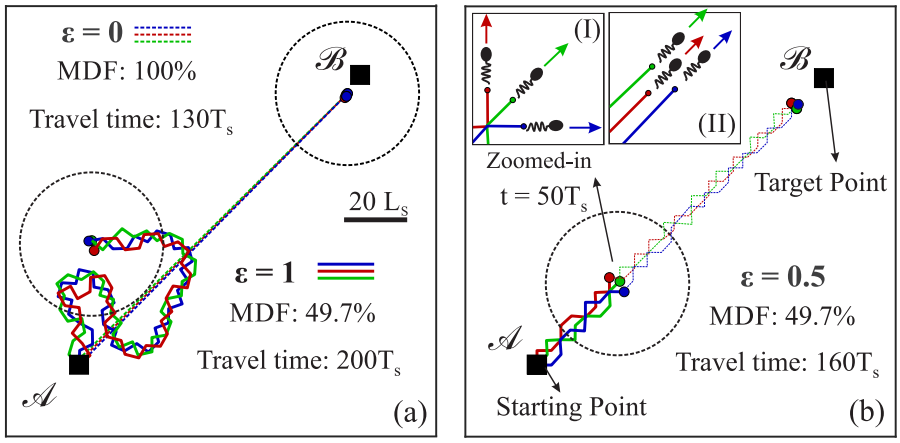

Figure 5.6: For caption see next page.

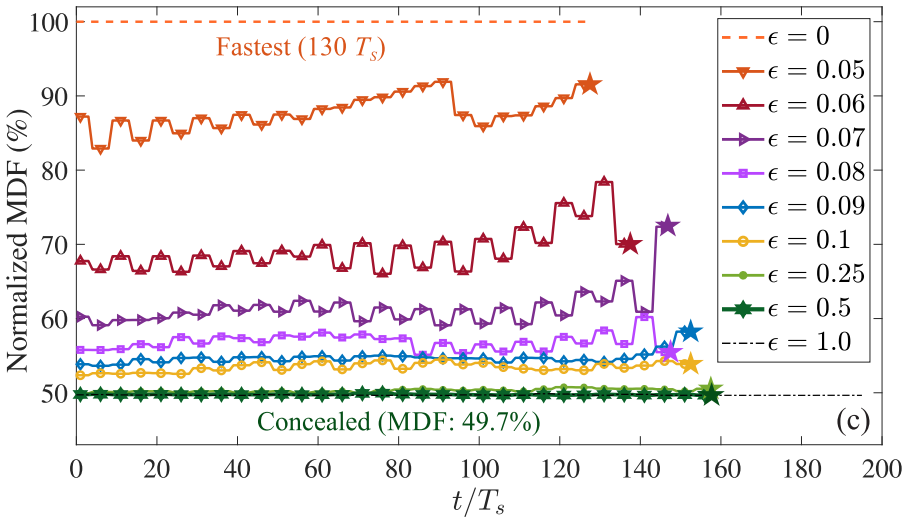

Figure 5.6: (cntd). Sample flocks of micro-swimmers, controlled by different values of ϵ, so as to travel from a starting point ($\mathscr{A}$) toward the target point (at $\mathscr{B}$). **(a):** Comparison between trajectories of the swimmers when controlled by extreme values of $\epsilon = 0$ and 1, respectively. Denoted by dashed thin lines are trajectories of the fastest traveling swarm (travel time = $130T_s$) with no concealing ($\epsilon = 0$). On the other hand, trajectories of the traveling swarm with the highest possible concealing efficiency (MDF = 49.7%), yet no constraints on preferred direction ($\epsilon = 1$), are denoted by solid thick lines. The latter never reaches the target point. **(b):** Snapshots of the optimal concealed traveling swarm ($\epsilon = 0.5$) having the most possible concealing efficiency in the cost of only 23% increase in the travel time. Blue, green, and red thick (thin) solid (dashed) lines represent trajectories of the swimmers after $t/T_s = 50$ (160). Instantaneous arrangement of the swimmers at $t/T_s = 50$ is schematically shown in a magnified view as inset (I) and is compared to the arrangement of an organized school (II) with MDF of about 100%. The dashed circles in panels (a) and (b) mark instantaneous position of each flock in the presented snapshots. **(c):** Fluid disturbances induced by the traveling swarms controlled with various values of ϵ, are measured in terms of MDF and monitored during their trip from $\mathscr{A}$ to $\mathscr{B}$. The terminal time, at which a swarm reaches to the target point $\mathscr{B}$, is denoted in each case by an asterisk.

for such an optimal traveling swarm is equivalent to $\sim 50\%$ shrink of the swarm's detection region throughout its migration from $\mathscr{A}$ to $\mathscr{B}$.

In the end, it also worths noting that although the focus of our analysis in this chapter has been on planar (2D) swarm arrangements/movements, the present study can be readily extended to three-dimensional (3D) scenarios. As a benchmark, we discuss 3D concealed arrangements in section 5.4.1 (Fig. 5.7), for which reduction of the swarm's induced disturbances exceed 99%. We then demonstrate how such swarm configurations can help a group of swimmers to remain stealth (with $\geq 90\%$ reduction in MDF) throughout their trip from $\mathscr{A}$ to $\mathscr{B}$ in a 3D space (Fig. 5.8). Additionally, a sample concealed swarm of micro-swimmers tracking a desired trajectory through a *non-uniform* environment is also discussed in section 5.4.3 (and specifically Fig. 5.10).

5.4 Other Notes

5.4.1 Concealed Swarms with 3D Arrangements/Movements

The focus of this chapter has been on planar (2D) swarm arrangements/movements. However, the present study can be readily extended to three-dimensional (3D) scenarios. In particular, the same procedure can be used to also find 3D optimal (i.e. concealed) swarm arrangements for any flock of N swimmers. The exception is that to quantify fluid disturbances induced by a 3D swarm arrangement, one needs to either: (i) compute the mean disturbing flow-magnitude (MDF) over the surface of a surrounding *sphere*, or (ii) compute the *volume* of a swarm's detection region (VDR).

As a benchmark, a 3D concealed arrangement is demonstrated in Fig. 5.7 for the same flock of twelve swimmers presented in Fig. 5.3 of this chapter. We highlight that forming such a 3D concealed swarm suppresses the induced disturbance by more than 99% – compare this value to the $\sim 50\%$ reduction achieved for 2D concealed arrangements of the same flock (Fig. 5.3). This is equivalent to more than 99% shrink of the instantaneous detection region for the swarm. Note that such a dramatic suppression of the induced disturbances, achieved by forming a 3D concealed swarm (versus a 2D one), reflects a sudden drop in leading order of the swarm's induced disturbing flows. In fact, for any sub-group of three orthogonally oriented agents, within a 3D swarm, the leading order of induced disturbances switches from being a dipole (decaying as $1/r^2$) to a quadrapole (vanishing as $1/r^3$).

Through altruistic collaborations, micro-swimmers also can form a 3D concealed swarm while traveling toward a target point in a 3D space (see Fig. 5.8). The objective function (to be minimized by the swarm through cooperation of the agents) remains untouched, and one can follow the same procedure (as outlined in the paper) to find the optimally concealed traveling swarm. The caveat here is that the 3D MDF has to be computed over the surface of a surrounding *sphere*. As a benchmark, here we show (in Fig. 5.8) a sample 3D concealed swarm of micro-swimmers traveling from a starting point ($\mathscr{A}$) toward a target point (at $\mathscr{B}$). Our numerical experiments reveal that by setting $\epsilon = 0.5$ the traveling swarm can shrink its

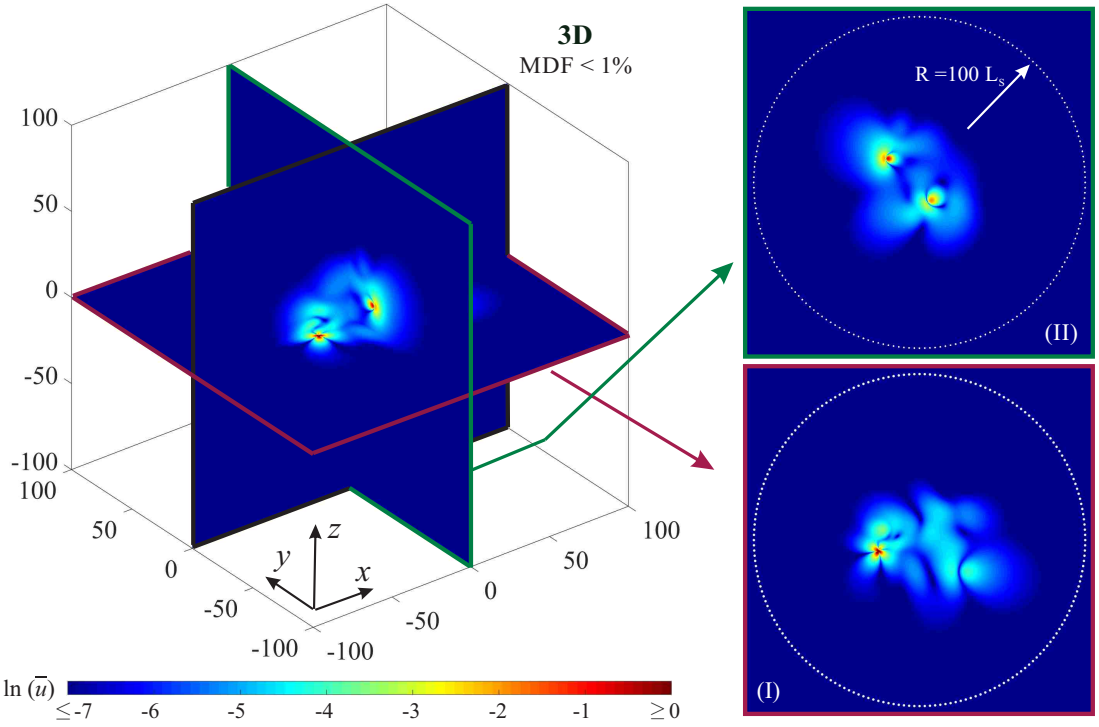

Figure 5.7: Magnitude of the net disturbing flows induced by a three-dimensional (3D) concealed swarm of $N = 12$ swimmers (c.f. the 2D arrangements presented in Fig. 5.3). Forming the presented optimal swarm arrangement suppresses the induced disturbances (and thus shrinks the swarm's detection region) by more than 99%. Here the induced fluid disturbances are quantified by computing mean disturbing flow-magnitude (MDF) over the surface of a surrounding sphere (with $R/L_s = 100$). Also, as a benchmark, the minimum separation distance (ξ) between swimmers forming the swarm is set to $10L_s$, which is the same as those presented in Fig. 5.3. Insets (I-II) represent (x-y) and (y-z) cross sections of the swarm arrangement, respectively. In the panels, color shading represents the flow magnitude, and white dotted rings represent cross-sections of the surrounding sphere used to compute MDF. The reference case used to normalize MDF, corresponds to the case of twelve aligned swimmers (i.e. in schooling arrangement) all located at the center point.

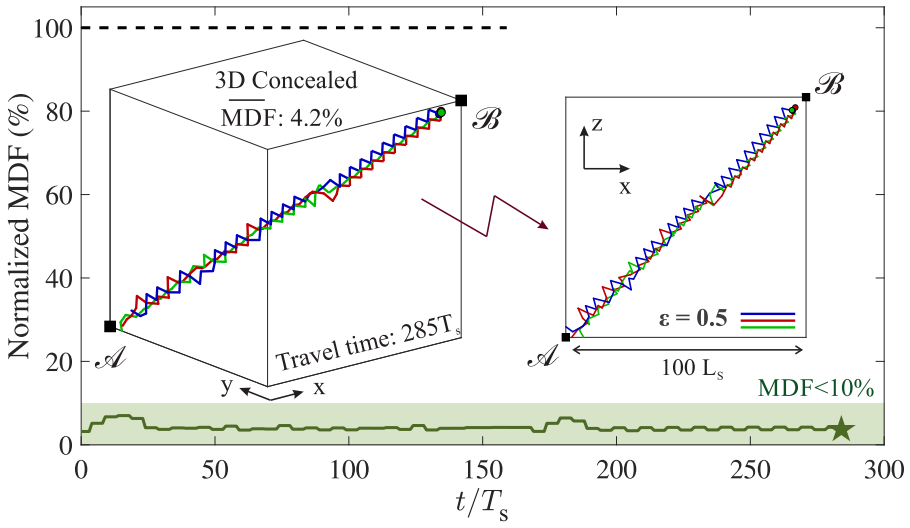

Figure 5.8: Fluid disturbances (measured in terms of MDF) induced by a 3D concealed swarm of three micro-swimmers are monitored throughout their migration (in an unbounded three-dimensional space) from a starting point ($\mathscr{A}$) toward a target point ($\mathscr{B}$). The 3D MDF is computed over the surface of a surrounding sphere of radius $R/L_s = 100$, and the swarm is controlled by $\epsilon = 0.5$ –see Eq.(5.9). The terminal time, at which the swarm reaches the desired target point at $\mathscr{B}$, is denoted by an asterisk. The insets represent trajectories of the swimmers in full 3D and 2D views, respectively. For the sake of comparison, disturbances induced by the fastest swarm with no concealing efficiency ($\epsilon = 0$) is also monitored (in terms of normalized MDF) over time, and is shown by a black dashed line.

detection region by more than 90% and remain concealed throughout the trip from $\mathscr{A}$ to $\mathscr{B}$ (see Fig. 5.8).

5.4.2 Stealth Target Pointing via Local Sensory Information

In the presented study we demonstrated that through altruistic collaborations, micro-swimmers can form a concealed swarm while traveling toward a target point or track a desired trajectory in space. These traveling swarms can represent: (i) flocks of swimming micro-robots traveling (in vivo) toward a target point while controlled to be fast/concealed (as tuned by ϵ); (ii) a swarm of predators attacking a target prey flock (at point $\mathscr{B}$) in stealth versus fast modes (tuned by ϵ); or even (iii) flocks of motile microorganisms swarming under influence of an external gradient (the intensity of which being modeled as $1 - \epsilon$) from $\mathscr{A}$ to $\mathscr{B}$ – e.g. in chemotaxis of sperm cells toward an egg. However, we note that sensing capabilities of swimming microorganisms are often limited to the point-wise measurement of various quantities – e.g. light or chemicals [101]. This makes them unable to identify their distance toward a desired target point, as required for the model presented in Eq. 5.9 of the

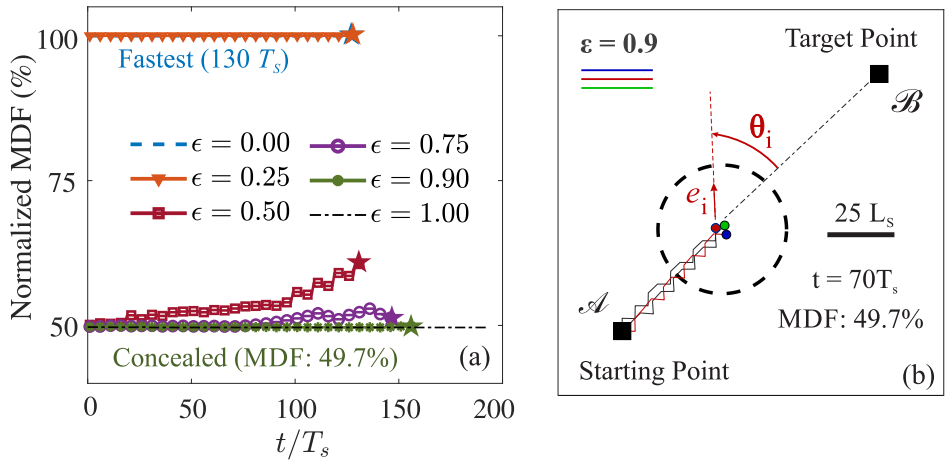

Figure 5.9: (a) Fluid disturbances induced by sample flocks of micro-swimmers, which are controlled to migrate from a starting point ($\mathscr{A}$) toward a target point ($\mathscr{B}$) with different values of ϵ tuning their alternative objective function (5.10). The presented traveling swarms can represent flocks of micro-swimmers swarming from $\mathscr{A}$ to $\mathscr{B}$ under influence of an external gradient, the intensity of which being tuned by different values of $1-\epsilon$. The terminal time, at which a swarm reaches the target point at $\mathscr{B}$, is denoted in each case by an asterisk. Note that the swarm corresponding to the extreme case of $\epsilon = 1$, never reaches the target. (b) Snapshots of the optimally concealed traveling swarm (controlled with $\epsilon = 0.9$) which has the highest possible concealing efficiency (MDF = 49.7%) in cost of only 23% increase in the travel time compared to the fastest possible swarm. As a benchmark, the deviation angle (θ_i) for the swimmer i swimming in direction e_i is shown (in red). Blue, green, and red solid lines represent trajectories of the swimmers after $70T_s$.

article. Therefore, for a bio-hybrid system which relies on sensing capabilities of swimming microorganisms, a more realistic objective function ($\mathscr{Z}$) can be devised by replacing $\bar{\text{RMS}}_d$ in Eq. 5.9 with $\bar{\text{RMS}}_\theta$, which stands for the normalized root mean square of the swimmers' deviations from their locally desired directions in the absence of concealing interests. The alternative objective function thereby reads as

$$\mathscr{Z} = \epsilon \times \bar{\text{MDF}} + (1-\epsilon) \times \bar{\text{RMS}}_\theta \ . \tag{5.10}$$

Note that when concealing is not of interest, the desired direction at the location of each swimmer is the steepest ascent in the external field that leads it toward the target. Thus, $\bar{\text{RMS}}_\theta$ stands for the normalized root mean square of the swimmers' deviations from the direction representing maximal gradient – i.e. the direction toward the target point (see e.g.

Fig. 5.9b). Mathematically, we define

$$\bar{\text{RMS}}_\theta = \sqrt{\left(\sum_{i=1}^{N} \theta_i^2\right)/N} \ . \tag{5.11}$$

This requires the swimmers to only identify deviation of their swimming direction from that of the maximal gradient in the external field of interest, that can be obtained locally.

Trade-off between the travel time and the overall efficiency of concealing in this case is demonstrated in Fig. 5.9. The induced fluid disturbances (measured in terms of MDF) are monitored during the trip from $\mathscr{A}$ to $\mathscr{B}$, while the traveling swarm is controlled with various values of ϵ. Similar to what was observed for the test cases presented in Fig. 5.6, as $\epsilon \to 0$ ($\to 1$) the swarm travels faster (slower) in space, i.e. the travel time decreases (increases), but it will induce more (less) disturbances to the ambient fluid. Our results reveal that the bottom-line of our analysis also remains the same. In particular, the results reveal that swarming in an optimally concealed mode (via such an alternative local sensory information), with more than 50% reduction in disturbances, may cost only 23% increase in the trip duration compared to the fastest possible trip (Fig. 5.9). This is equivalent to 50% shrink in detection region of the swarm throughout its migration from $\mathscr{A}$ to $\mathscr{B}$.

5.4.3 Stealth Trajectory Tracking in a non-Uniform Environment

There exist many situations, for both biological micro-robots and swimming microorganisms, in which they have to travel through a non-uniform environment. Examples include fluids at the interface of different organs inside the human body with distinct viscosities, or those in vicinity of a mucus zone [102]. Depending on their propulsion mechanism, motile microorganisms experience different energy expenditures, and thus distinct swimming speeds, while traveling in regions with different rheological properties [103, 104, 105, 106, 107, 108].

Here, we show that through altruistic collaborations, micro-swimmers can also remain stealth while traveling toward a target point or tracking a desired trajectory in such *non-uniform* environments. In particular, we are interested to find an *optimally* concealed traveling swarm, that is the fastest among those with highest possible concealing efficiency – see e.g. the one presented in Fig. 5.6(b) passing through a uniform environment. Note that a straight line connecting two points in non-uniform environments no longer represents the fastest pathway between them. Therefore, one needs to first find the optimal (i.e. fastest) pathway from the starting point to the target point. Then, a similar procedure (as outlined in section III-C) can be used to track the specified trajectory. However, there is a caveat here: $\bar{\text{RMS}}_d$ in the objective function ($\mathscr{Z}$), now stands for the normalized root mean square of swimmers' distances from the optimal pathway.

As a benchmark, let us consider a simple example of two side-by-side regions (Fig. 5.10), each with a distinct swimming cost for swimmers. This, for instance, can represent the interface between two distinct liquids. A concealed swarm of three micro-swimmers tracking

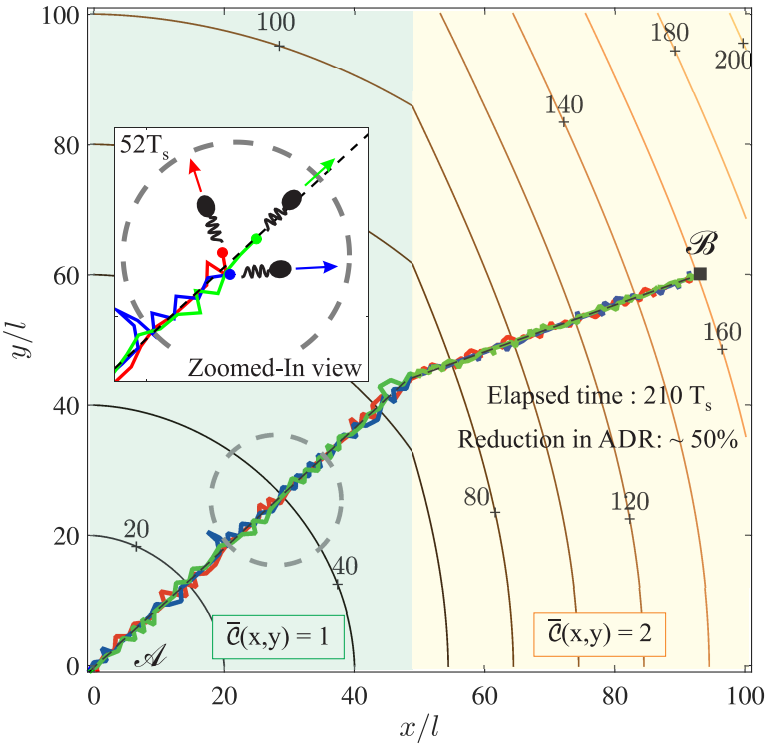

Figure 5.10: A concealed swarm of three micro-swimmers tracking an optimal trajectory in a non-uniform environment from a starting point ($\mathscr{A}$) to a target point at $\mathscr{B}$. Detection region of the swimmers is significantly stifled, such that reduction in ADR exceeds 50% during the trip. This is equivalent to minimal disturbances toward the ambient fluid with 50.4% reduction in MDF. Total time taken for the swimmers to reach the target point is $210T_s$. The normalized swimming cost is $\bar{C}(x,y) = 1$ for $x/l < 50$, and $\bar{C}(x,y) = 2$ for $x/l \geq 50$. The optimal (i.e. fastest) pathway from $\mathscr{A}$ to $\mathscr{B}$ is computed through fast marching level-set method, and is shown by a black dashed line. Isolines correspond to $\bar{\mathcal{T}}(x,y)$, that is the minimum time required to reach any point (x,y), starting from point $\mathscr{A}$. Trajectories of the swimmers (tracking the optimal pathway) are also shown by blue, red and green solid lines. The inset represents a specific moment from the trip (as marked by a dashed circle), where schematics demonstrate arrangement of the swimmers at this moment.

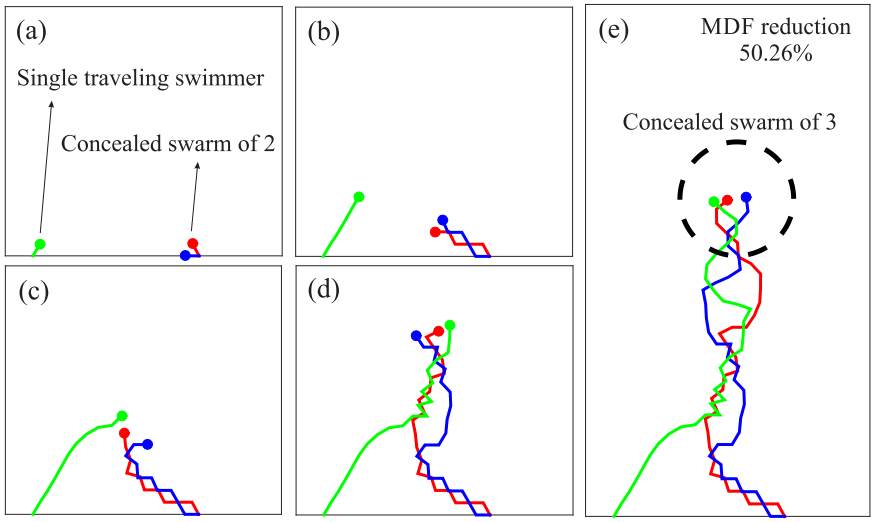

Figure 5.11: Snapshots of a single traveling swimmer joining a nearby (traveling) concealed swarm to minimize the overall disturbing flows. (a)-(b) There is a mutual desire to bring the single swimmer into the swarm. (c)-(d) Members trying to form a new optimal swarm arrangement to include the new member in the group. (e) A concealed swarm of three swimmers is formed with more than 50% reduction in MDF.

a prescribed optimal pathway (from $\mathscr{A}$ to $\mathscr{B}$) through such an inhomogeneous environment is represented in Fig. 5.10. At the cost of only 30% increase in the travel time, compared to the fastest possible swarm, detection region of the swarm is significantly stifled, so that reduction in ADR exceeds 50% during the trip. This is also equivalent to minimally disturbing the ambient fluid with 50.4% reduction in MDF.

It also worths noting that by solving the normalized Eikonal equation, i.e. $|\nabla\bar{\mathcal{T}}| = \bar{C}(\bar{x},\bar{y})$, using a fast marching level-set method [109, 110], one can find $\bar{\mathcal{T}}(\bar{x},\bar{y})$, which is the minimum cost (i.e., the least required time) of reaching to any arbitrary point $(\bar{x},\bar{y})$ in space. Here, the bar signs denote dimensionless quantities and $\bar{C}(\bar{x},\bar{y})$ is the swimming cost at $(\bar{x},\bar{y})$ normalized by U_s^{-1}. Values of $\mathcal{T}$ are also normalized by the time scale $T_s = L_s/U_s$. Tracing back from point $\mathscr{B}$ to $\mathscr{A}$, while always moving normal to the isolines of $\bar{\mathcal{T}}$ (see Fig. 5.10), will then provide the optimal pathway from $\mathscr{A}$ to $\mathscr{B}$ [110].

5.4.4 Expansion of a concealed swarm

As we discussed in section 5.3.1, it is desired for individual swimmers to form a group and collaborate to cancel out each others disturbing effects to the surrounding fluid. Our results further reveal that a traveling concealed swarm can attract nearby individual swimmers (those swimming in its vicinity), and subsequently expand by re-forming into a new larger swarm. To provide further insight, the minimal example is demonstrated in Fig. 5.11 via

successive snapshots (a)-(e). It is shown how a single traveling swimmer joins a nearby concealed swarm of two swimmers, and together, they form a new concealed swarm of three swimmers. Note that the only imposed constraint on the motion of swimmers is the upward swimming (c.f. gravitaxis). Relaxing this constraint will simply result in a quasi-random walk of the swarm with no preferred direction.

5.5 Concluding Remarks

To summarize, in this chapter we revealed that micro-swimmers can form a stealth swarm through controlled cooperation in suppressing one another's disturbing flows. Specifically, our results unveil the existence of *concealed* arrangements, which can stifle the swarm's hydrodynamic signature (and thus shrink its detection region) by more than 50% (or 99%) for planar (or 3D) movements. We then demonstrated how such a concealed swarm can actively gather around a desired spot, point toward a target, or track a prescribed trajectory in space. Our study provides a road map to optimally control/lead a swarm of interacting micro-robots in stealth versus fast modes. This, in turn, paves the path for non-invasive intrusion of swimming micro-robots with a broad range of biomedical applications [18].

The presented findings also provide insights into dynamics of prey-predator systems. Importance of the fluid mechanical signals (i.e. flow signatures) produced by swimming objects, in dynamics of prey-predator systems is well appreciated for a broad range of aquatic organisms. Free-living copepods, for example, possess highly sensitive fluid-mechanoreceptors [111] capable of detecting disturbing flows as small as 20 μms^{-1}. These sensors enable the organism to accurately measure fluid disturbances induced by nearby predators (preys), estimate their distance/size, and thereby properly trigger escape (catch) behavior [112, 113]. Another example is the Gram-negative *Bdellovibrio bacteriovorus* [114], which is a prototypical predator among motile microorganisms and hunts other bacteria, such as *E. coli*. Recent experiments [115] show that it is, in fact, hydrodynamics rather than chemical clues that lead this predator into regions with high density of prey. Therefore, quenching the flow signature (and thus shrinking the associated detection region) by swarming in concealed modes, can potentially have a significant impact on trophic transfer rates among a broad range of aquatic organisms. In particular, stifling the induced disturbances may help an active swarm of prey swimmers gathered around a favorite spot (say, a nutrient source) to lower their detectability (and thus predation risk) through shrinking their detection region. Quenching flow signatures induced by a traveling swarm, on the other hand, may help a swarm of predators to remain concealed while attacking a target prey flock.

Acknowledgments

This work is supported by the National Science Foundation grant CMMI-1562871.

Chapter 6

Active Cloaking via Reinforcement Learning

Hydrodynamic signatures at the Stokes regime, pertinent to motility of micro-swimmers, have a long-range nature. This implies that movements of an object in such a viscosity-dominated regime, can be felt tens of body-lengths away and significantly alter dynamics of the surrounding environment. In this chapter, a systematic methodology is presented to actively cloak swimming objects within any arbitrarily crowded suspension of micro-swimmers. Specifically, our approach is to conceal the target swimmer throughout its motion using cooperative flocks of swimming agents equipped with adaptive decision-making intelligence. Through a reinforcement learning algorithm, the cloaking agents experientially learn optimal adaptive behavior policy in the presence of flow-mediated interactions. This artificial intelligence enables them to dynamically adjust their swimming actions, so as to optimally form and robustly retain any desired arrangement around a moving object without disturbing it from its original path. Therefore, the presented active cloaking approach not only is *robust* against disturbances, but also is *non-invasive* to motion of the cloaked object. We then further generalize the proposed approach and demonstrate how our cloaking agents can be readily used, in any region of interest, to realize hydrodynamic invisibility cloaks around any number of arbitrarily moving intruders.

6.1 Introduction

Living organisms in aquatic environments highly depend on detecting the fluid-mechanical signals caused by motions in the surrounding fluid [116]. A broad range of swimming organisms, for instance, possess intricate sensors to directly measure the magnitude of disturbing flows (i.e. flow signatures) induced by nearby swimming objects [see 111, 113, 116]. This invaluable information is then used, as a 'tool', to detect the presence of nearby predators (preys), estimate their relative distance/size, and subsequently trigger an appropriate escape (catch) behavior [see 117, 118, 119]. For micro-swimmers, however, it was recently

revealed [13] that an interacting flock can significantly suppress the induced disturbances (by $\sim 50\%$) once swarming in specific arrangements (referred to as *concealed* modes). This finding inspires an even more intriguing question, that is whether a micro-swimmer can be actively cloaked, so as to remain undetectable (generating no trace) when passing through a host medium? Equivalently, is there a way to actively cloak random intruders to protect a sensitive region from disturbing effects of their induced fluid flows?

The concept of cloaking has long been of great interest to physicists and engineers, and remarkable progress has been made toward cloaking an object in the realm of electromagnetic waves [see e.g. 120, 121], gravity waves [see e.g. 122], fluid flows [see e.g. 123, 124], acoustics [see e.g. 125, 126], quantum mechanics [see e.g. 127], thermodynamics [see e.g. 128], solid mechanics [see e.g. 129], and even time [see e.g. 130].

Realizing a hydrodynamic invisibility cloak for a motile micro-swimmer, however, faces two fundamental challenges: (i) the *dynamic* nature of the subject, that is continuously moving in arbitrary directions; and (ii) the long-range nature of underlying flow-mediated interactions, which can easily induce chaos and bring disorder to any potentially designed cloaking system that is initially set to a perfect order. The latter is further exacerbated for the case of cloaking specific subjects within a crowded suspension of micro-swimmers. In fact, the motion of each swimming object in the Stokes regime, perturbs the net flow field at the position of all nearby swimmers, and thus alters dynamics of the entire system. Therefore, to properly conceal swimming objects in a viscous environment, the cloak formation has to dynamically adjust in response to such non-linearly varying hydrodynamic loads. This leads us to the concept of *active* cloaking.

In this chapter, the first demonstration of active cloaking in Stokes flows is presented using cooperative flocks of micro-swimmers – hereafter referred to as the '*cloaking agents*'. In the presented method, hydrodynamic signature of the cloaked object – hereafter referred to as the '*intruder*', is actively suppressed (throughout its motion) by a group of cloaking agents that form specific arrangements around it. To optimally form (and robustly retain) such desired cloaking arrangements around a moving intruder, the agents indeed need to dynamically adjust their swimming actions. Therefore, we first provide a rigorous approach to systematically train the cloaking agents through a reinforcement learning algorithm. This experiential learning process, equips the agents with an optimal adaptive behavior policy in the presence of flow-mediated interactions. The sequence of actions taken by the agents based on such an artificial intelligence, enables them to keep any arbitrary intruder concealed throughout its motion without disturbing it from its original path. Therefore, the presented active cloaking approach is also *non-invasive* to the intruder's motion. We then further generalize our approach, and demonstrate how these smart cloaking agents can be readily used to realize hydrodynamic invisibility cloaks around any number of swimming objects, within any arbitrarily crowded suspension of micro-swimmers.

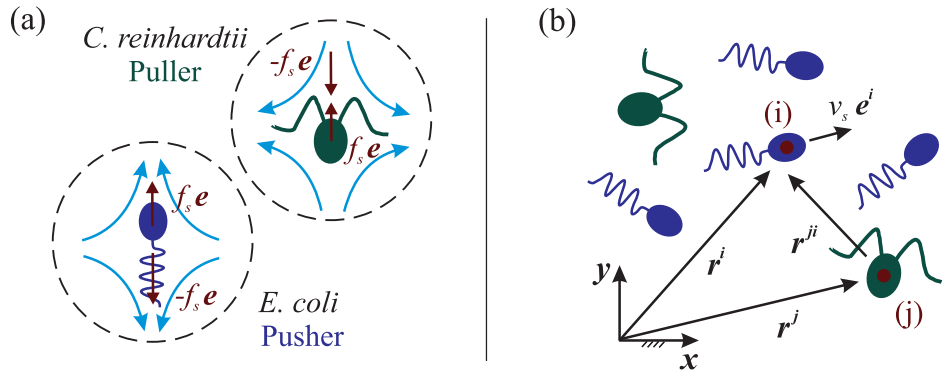

Figure 6.1: (a) Schematic representation of the archetypal puller and pusher swimmers. The force dipole ($\pm f_0 \boldsymbol{e}$) exerted by each swimmer to the surrounding fluid is shown by red arrows. Vector $\boldsymbol{e}$ denotes the swimming direction, and curly blue arrows demonstrate direction of the induced disturbing flows in each case. (b) Schematic representation for a system of interacting micro-swimmers. The position vector of swimmer $i \in \{1 \dots N\}$, swimming with speed V_s in direction $\boldsymbol{e^i}$, is denoted by $\boldsymbol{r}^i$ with respect to the fixed frame of reference. Here $N = 6$, and the system includes both pusher and puller swimmers.

6.2 Interaction Dynamics in Viscous Environments

Dynamics of the flow induced by a micro-swimmer (i.e. a swimming micro-robot or a motile microorganism) can be described by the Stokes equations:

$$\nabla P = \mu \, \nabla^2 \boldsymbol{u} + \boldsymbol{F}, \quad \nabla \cdot \boldsymbol{u} = 0. \tag{6.1}$$

where μ is dynamic viscosity of the surrounding fluid, P represents the pressure field, $\boldsymbol{u}$ is the velocity field, and $\boldsymbol{F}$ is the notion of body forces per unit volume. In the absence of external (magnetic or electric) fields, a self-propelled buoyant micro-swimmer exerts no net force/torque to the surrounding fluid. Therefore, in the most general form, far-field of the disturbing flow induced by a micro-swimmer is well-described by the flow of a force dipole ($\pm f_s \boldsymbol{e}$) composed of the thrust force (generated by the swimmer's propulsion mechanism) and the viscous drag acting on its body (Fig. 6.1a). To be more precise, for a micro-swimmer swimming with speed v_s toward direction $\boldsymbol{e}$ through an unbounded fluid domain, the induced flow field can be formulated [see e.g. 26] as

$$\boldsymbol{u}_{\mathrm{SD}} = \frac{\mathscr{D}}{8\pi\mu \, r^3} \left[-1 + 3 \left(\frac{\boldsymbol{r} \cdot \boldsymbol{e}}{r} \right)^2 \right] \boldsymbol{r}, \tag{6.2}$$

where $\boldsymbol{r} = \boldsymbol{x} - \boldsymbol{x}_0$, for any generic point $\boldsymbol{x}$ in space; $\boldsymbol{x}_0$ represents the instantaneous position of the swimmer, and $r = |\boldsymbol{r}|$. The dipole strength, $|\mathscr{D}| \sim v_s L_s^2 \sim f_s L_s$, has a positive (negative) sign for pusher (puller) swimmers, and its value can be inferred from experimental

measurements [see e.g. 90]. Here the characteristic length L_s is on the order of swimmer dimensions, and we use $\{U_s = v_s, L_s, T_s = L_s/v_s\}$ to make the quantities dimensionless.

Swimming in the Stokes regime is significantly affected by the presence of long-range hydrodynamic interactions. In fact, disturbing flows induced by the motion of each micro-swimmer highly affects dynamics of other nearby swimming objects. Here we take into account both *hydrodynamic* and *steric* interactions between the swimmers. To this end, let us consider a generic flock of 'N' interacting micro-swimmers as presented schematically in Fig. 6.1(b). For any swimmer $i \in \{1, \dots, N\}$ in the flock, dynamics of the position vector, $\boldsymbol{r}^i$, and the swimming direction, $\boldsymbol{e}^i$, are governed by

$$\dot{\boldsymbol{r}}^i = v_s \boldsymbol{e}^i + \sum_{j \neq i} \left[\boldsymbol{u}^j \left(\boldsymbol{r}^i \right) + \frac{1}{6\pi\mu L_s} \, \boldsymbol{\mathcal{F}}^j \left(\boldsymbol{r}^i \right) \right] + \boldsymbol{u}_f \left(\boldsymbol{r}^i \right), \tag{6.3a}$$

$$\dot{\boldsymbol{e}}^i = \left\{ \frac{1}{2} \, \boldsymbol{\omega}_f \left(\boldsymbol{r}^i \right) + \frac{1}{2} \sum_{j \neq i} \boldsymbol{\omega}^j \left(\boldsymbol{r}^i \right) + \mathcal{B} \boldsymbol{e}^i \times \left[\mathtt{E}_f \left(\boldsymbol{r}^i \right) + \sum_{j \neq i} \mathtt{E}^j \left(\boldsymbol{r}^i \right) \right] \cdot \boldsymbol{e}^i \right\} \times \boldsymbol{e}^i, \tag{6.3b}$$

where $\boldsymbol{u}^j \left(\boldsymbol{r}^i \right) = \boldsymbol{u}_{\mathrm{SD}} \left(\boldsymbol{r}^i - \boldsymbol{r}^j \right)$ is the disturbing flow induced by swimmer 'j' at the position of swimmer 'i' (6.2), and $\boldsymbol{\omega}^j = \nabla \times \boldsymbol{u}^j$ is the corresponding vorticity field. Similarly, $\boldsymbol{u}_f \left(\boldsymbol{r}^i \right)$ denotes the background (external) flow at the position of swimmer 'i', and $\boldsymbol{\omega}_f = \nabla \times \boldsymbol{u}_f$ is the corresponding vorticity field. Here each swimmer is modeled as an infinitesimal spheroid of aspect ratio λ, for which the Bretherton constant [see e.g. 131] is defined as $\mathcal{B} = \left(\lambda^2 - 1 \right) / \left(\lambda^2 + 1 \right)$. The rate of strain tensor, defined as

$$\mathtt{E} \left(\boldsymbol{r}^i \right) = \frac{1}{2} \left[\nabla \boldsymbol{u} (\boldsymbol{r}^i) + \nabla \boldsymbol{u}^\top (\boldsymbol{r}^i) \right], \tag{6.4}$$

is also denoted by $\mathtt{E}^j$ and $\mathtt{E}_f$, for $\boldsymbol{u}^j$ and $\boldsymbol{u}_f$, respectively. To regularize our dipole models (diverging as $1/r^2$), we also define a purely repulsive force [c.f. 132], based on the Lenard-Jones-type potential:

$$\boldsymbol{\mathcal{F}}^j \left(\boldsymbol{r}^i \right) = -\partial \mathscr{L}^{ji} / \partial \boldsymbol{r}^{ji}, \quad \mathscr{L}^{ji} = 4\epsilon_L \left[\left(\frac{\sigma}{r^{ji}} \right)^{12} - \left(\frac{\sigma}{r^{ji}} \right)^{6} \right] + \epsilon_L, \tag{6.5}$$

where $r^{ji} = |\boldsymbol{r}^i - \boldsymbol{r}^j|$, the constant σ indirectly specifies the equilibrium distance (i.e. $2^{1/6}\sigma \sim 2L_s$), and ϵ_L tunes strength of the steric interactions. This ensures the excluded volume constraints, and thus pushes the swimmers away from each other when approaching closer than a certain distance (determined by $2^{1/6}\sigma$).

It is worth noting that the presented framework (6.3) can be readily extended by incorporating a more detailed description of $\boldsymbol{u}^j \left(\boldsymbol{r}^i \right)$. In particular, near-field of the flow induced by micro-swimmers can be described more accurately through including an appropriately chosen combination of higher order terms from the multipole expansion [see e.g. 133, 92]. However, in this work, we are interested in the *span* of swimmers' induced disturbances and their consequent detection region, for which far-field of the flow is of primary interest. Therefore, as discussed earlier, the disturbing flow induced by each micro-swimmer is formulated

here, in the most general form, as the flow of a force dipole. This simple model has been validated and widely used in the literature [see 89, 26]. In particular, for archetypal pusher and puller swimmers (i.e. *Escherichia coli* bacteria and *Chlamydomonas reinhardtii* alga) used as benchmarks throughout this work, the validity of this model is further confirmed via direct comparison to the disturbing flows (experimentally) measured around individual swimming cells [60, 90]. In the case of *E. coli* bacteria, for instance, values of $f_s = 0.42$ pN and $L_s = 1.9$ μm, have been suggested [90] in agreement with resistive force theory [83] and optical trap measurements [91]. The corresponding dipole model (with $\mathscr{D} \sim f_s L_s$) is proven to be highly accurate in predicting magnitude of the induced disturbing flows, even at distances comparable to characteristic length of the swimmer [90]. To be more specific, the predicted values are in agreement with those experimentally measured around an individual swimming cell at ranges $r \gtrsim 3L_s$. At shorter distances, the induced disturbing flows are shown to be less significant than those estimated by the dipole model [90], and thus steric interactions ('soft' collisions) are known to dominate the hydrodynamic interaction. Therefore, it is expected that the dipolar hydrodynamics, when supplemented by the Lennard-Jones-type excluded volume interactions (6.5), well-describe interaction dynamics in a semi-dilute suspension (see e.g. [132, 134]).

To keep the model simple and tractable in this work, we specifically consider swimmers with spherical body shapes (with $\mathcal{B} = 0$) for our swimmers. Nevertheless, the presented framework (6.3) explicitly incorporates the effects of swimmers' geometry. Thus, it can be used to describe the interaction dynamics of micro-swimmers with different shapes. In the case of ellipsoidal body shapes with eccentricity λ, for instance, the Bretherton constant can be evaluated as $\mathcal{B} = (\lambda^2 - 1)\,/\,(\lambda^2 + 1)$. This stands for the values of $\mathcal{B} = 0/1$ for spheres/needles, and takes positive (negative) values for prolate (oblate) objects.

6.3 Cloaking a micro-Swimmer in Stokes Flows

A cloak is commonly referred to as a patch enclosing an object to make it invisible. In an aquatic environment, however, swimming organisms nearly always use fluid disturbances (caused by motions in the surrounding fluid), as hydrodynamic signals to detect the nearby objects. Therefore, to be invisible in such environments, one needs to generate no disturbances to the ambient fluid. Accordingly, here we define the cloak as a patch virtually covering/enclosing a swimmer to cancel out its induced disturbances. This will then keep the enclosed swimmer 'invisible' to others in the medium – by stifling its flow signature. Similar to other forms of cloaking, a suitable cloak is also required to be omni-directional, that is, to keep itself and the enclosed swimmer 'invisible' from any direction. It worths highlighting that the induced disturbing flows have a long-range nature at the Stokes regime pertinent to motility of micro-swimmers. This means that despite high Reynolds number motions in which hydrodynamic signature is relatively confined to the immediate neighborhood, the motion of an object at a low Reynolds number regime can be felt tens of body-lengths away. Thus, movements of micro-swimmers significantly alter their surrounding environment. As a

result, specific to biological applications, cloaking a micro-swimmer may be more important in *protecting* sensitive regions (e.g. organs) against disturbing flows induced by intruders – such as passing-by swimming microorganisms or deployed biomedical micro-robots. This, indeed, is equivalent to making such intruders hydrodynamically invisible (i.e. cloaked) within the surrounding environment.

We assess the effectiveness of an invisibility cloak in Stokes regime, by evaluating its efficiency in stifling the swimmer's induced disturbing flows. A measure of distortion caused by swimming objects to the ambient fluid can be obtained through directly computing the mean disturbing flow-magnitude ($\mathscr{U}$) over a surrounding ring of radius R (c.f. Fig. 6.2a) – here denoted by $\mathcal{C}(R)$. The cloaking efficiency (η) can then be calculated as

$$\eta = 1 - \frac{\mathscr{U}_c}{\mathscr{U}_i}, \quad \mathscr{U} = \frac{1}{2\pi R} \oint_{\mathcal{C}(R)} |\bar{\boldsymbol{u}}| \, \mathrm{ds}, \tag{6.6}$$

where $\mathscr{U}_c$ measures the induced disturbances once the cloak is implemented (i.e. corresponding to the net flows generated by the swimmer and its implemented cloak), and is directly compared to disturbances induced by the isolated swimmer ($\mathscr{U}_i$) – when no cloaking is in place. Here, 'ds' is the differential length along the surrounding ring, and $\bar{\boldsymbol{u}} = \boldsymbol{u}/v_s$ represents the net dimensionless flow field induced by the swimmer/system.

The simplest strategy in cloaking a single swimmer (an *intruder*) at any given instance of time is to properly position, next to it, another swimmer of the same dipolar strength, but from the opposite type. This basically replaces the dipolar (vanishing as $1/r^2$) leading order of the overall disturbing flows (in the far-field) with a quadrupole (rapidly decaying as $1/r^3$), and thus can effectively cloak the intruder by drastically stifling its induced disturbances in the ambient fluid. To give an example, a single cloaking agent positioned next to the intruder with a separation distance of r_0, dramatically reduces magnitude of the overall detectable

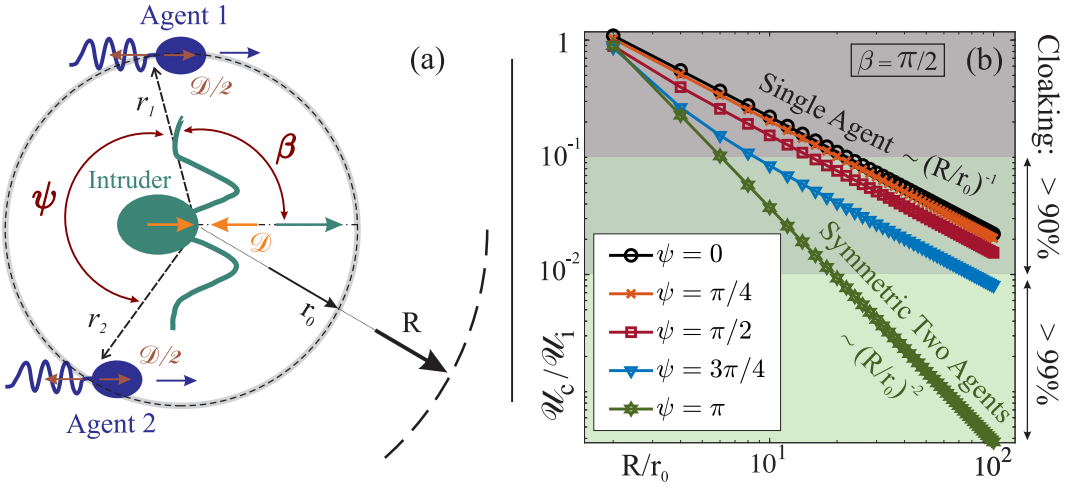

Figure 6.2: For caption see next page.

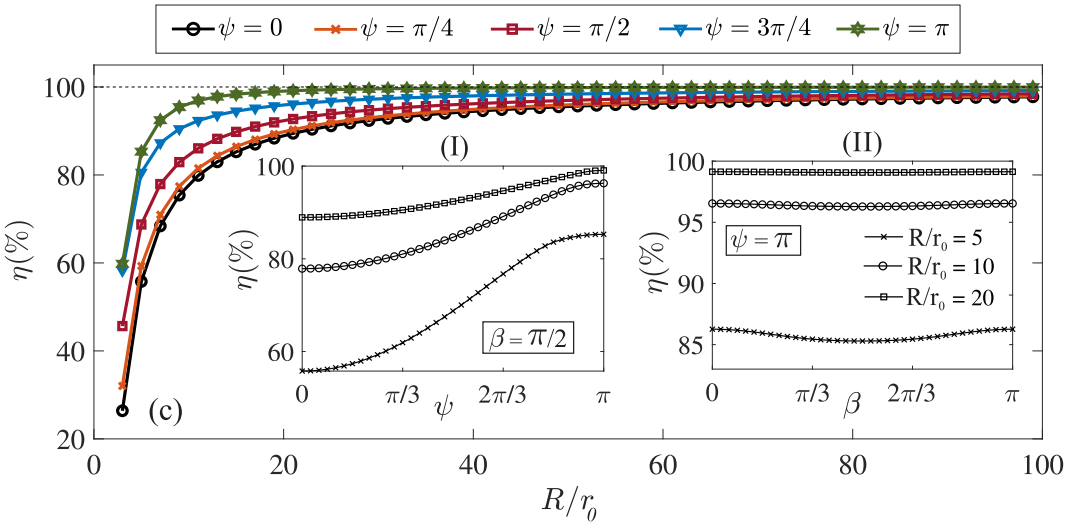

Figure 6.2: (cntd). **(a)** Schematic representation of the proposed method for cloaking an intruder (here a puller swimmer shown in green) using properly positioned single ($\psi = 0$) or double ($\psi \neq 0$) cloaking agents (here the pusher swimmers shown in blue). To compute the cloaking efficiency of different arrangements, the induced fluid disturbances are measured over a surrounding (dashed) ring of radius R. The dipole strength of each smart agent is half of the intruder's (i.e. $\mathscr{D}/2$). The agents are positioned on a (highlighted dashed) ring of radius r_0 around the intruder – i.e. their separation distance from the intruder is set to r_0, and their relative position vectors are denoted by $\boldsymbol{r_1}$ and $\boldsymbol{r_2}$, respectively. The angle between these two vectors is denoted by ψ and represents a measure of symmetry. Also, β is defined as the angle between intruder's swimming direction (green arrow) and the position vector $\boldsymbol{r_1}$. **(b)** Magnitude of the net fluid disturbances ($\mathscr{U}_c$) induced by the cloaked intruder and its cloaking agents, normalized by that of an isolated intruder ($\mathscr{U}_i$), is plotted for various cloak arrangements as a function of distance from the swimmer (R). Specifically, $\mathscr{U}_c/\mathscr{U}_i$ is plotted as a function of R/r_0 for $\psi = 0$, $\pi/4$, $\pi/2$, $3\pi/4$, and π, where β is set to $\pi/2$. **(c)** The cloaking efficiency of the arrangements associated with each of the ψ-angles presented in panel (b), is plotted as a function of R/r_0. Insets also demonstrate how the cloaking performance (in terms of $\eta\%$) varies with ψ (I) and β (II), respectively. For all cases presented in (I), β is fixed to $\pi/2$, and for those presented in (II), ψ is fixed to π. The presented values are measured at $R/r_0 = 5$, 10, and 20.

disturbing flows (measured by $\mathscr{U}$) to 11.6% and 4.4% of its original value, once measured at distances $R/r_0 = 20$, and 50 from the intruder, respectively (Fig. 6.2b for $\psi = 0$). This is equivalent to more than 88.4% and 95.6% in cloaking efficiencies at the ranges of $R/r_0 \geq 20$, and ≥ 50, respectively (Fig. 6.2 for $\psi = 0$). For this simple approach, however, the underlying hydrodynamic interaction between the intruder and its cloaking agent will inevitably disturb the intruder from its original path. Therefore, using a single cloaking agent, although effective, is not the smartest approach.

Here, we are particularly interested in implementing non-invasive active cloaking, where the cloaked swimmer (i.e. the intruder) is not deviated from its original path by the cloak implementation. This is fundamentally impossible using only a single cloaking agent. Alternatively, a proper positioning of two *half-sized* cloaking agents around an intruder (e.g. see Fig. 6.2-a for $\psi = \pi$ and $\beta = \pi/2$), can potentially prevent its deviation from the original path. This also significantly improves the cloaking efficiency (by switching the leading order in the far-field of induced disturbing flows to an octupole rapidly vanishing as $1/r^4$) compared to the single-agent method (with quadrupolar far-field decaying as $1/r^3$).

The schematic representations of cloaking an intruder using single ($\psi = 0$) and double ($\psi \neq 0$) cloaking agents are presented in Fig. 6.2(a). We also present cloaking performances corresponding to various arrangements of the agents around an intruder in Fig. 6.2 – both in terms of the relative magnitude of induced disturbances ($\mathscr{U}_c/\mathscr{U}_i$) and the cloaking efficiency (η). Note that the presented efficiencies correspond to a set of optimally designed cloaking agents which can provide an ideally canceling set of dipole strengths for the specific intruder of interest. Our results show that the effect of angular positioning (measured by β) on cloaking efficiency is negligible (Fig. 6.2c-II), whereas ψ (as a measure of symmetry) primarily controls the efficiency (Fig. 6.2c-I). Variation of ψ in the range of $[0, \pi]$ basically covers the whole spectrum from single-agent ($\psi = 0$) to symmetric double-agent ($\psi = \pi$) cloaking. It is worth highlighting that the symmetric arrangement of cloaking agents on the sides of an intruder (i.e. the arrangement with $\psi = \pi$ and $\beta = \pi/2$ in Fig. 6.2-a), represents not only a *non-invasive*, but also the most *efficient* double-agent cloaking strategy. The latter, in particular, is not immediately clear a priori, and has been revealed through the presented results (Fig. 6.2). In practice, such an optimal arrangement can potentially be used to realize a virtually perfect *non-invasive* cloak, the efficiency of which reaches beyond 99%, and 99.9% at distances $R/r_0 \geq 20$ and 50, respectively (Fig. 6.2).

Active cloaking of an arbitrarily moving intruder in the Stokes regime, however, still remains a challenge. For naive (i.e. non-smart) pair of cloaking agents, even if they are initially placed accurately in their predefined positions, the arrangement will soon be distorted due to the presence of long-range hydrodynamic interactions – causing the swimming agents to either diverge from one another or collide. In fact, disturbing flows induced by the intruder (although canceled out by its cloak in the far-field) are internally disruptive for the cloak itself – i.e. disturbs the agents' arrangement and thus breaks the cloak. Therefore, to realize *active* cloaking in the presence of such complex flow-mediated interactions, key questions still remain to be addressed in the following section: First, what is the optimal sequence of actions (corresponding to the shortest non-invasive path) for each cloaking agent

to position itself in a desired arrangement around an arbitrary intruder? Then, what is the optimal behavior policy for the cloaking agents to dynamically adjust their swimming actions in response to non-linearly varying hydrodynamic loads, so as to robustly keep their concealing arrangements around an intruder? Lastly, to what extent is the presented approach generalizable? That is, can we use it to actively cloak multiple arbitrary intruders within crowded suspensions, where each swimmer moves toward an arbitrary direction and experiences frequent close encounters?

6.4 Learning to Cloak Random Intruders via Reinforcement Learning

Here, a systematic methodology is presented to equip micro-swimmers with adaptive decision-making intelligence in response to flow-mediated interactions. We then use these smart agents to elucidate *active* cloaking of arbitrary intruders within a crowded environment. Note that once an agent is equipped with such an artificial intelligence, it will consider potential consequences of its actions when making any decision – hence, is called a *planning* agent. One may alternatively suggest the implementation of an external active control to lead each of the employed swimming micro-robots (i.e. cloaking agents) toward the desired arrangements. However, the efficacy of such approaches suffer from nonlinearly varying hydrodynamic loads due to the presence of flow-mediated interactions. In fact, the dynamical system representing a group of interacting micro-swimmers, is a complicated four-way-coupled system, where any tiny perturbation/deviation in prescribed motions of the swimmers can induce unpredicted complex choreographies [11, see e.g.]. It also worths noting that the *reflex* agents (by definition) are incapable of identifying *optimal* pathways to form non-invasive cloaks, especially in crowded suspensions or in the presence of obstacles. Therefore, here our approach is to let the cloaking agents learn optimal action policies by their own experience through a reinforcement learning algorithm [135]. By accumulating experience, our cloaking agents learn how to optimally collaborate, and dynamically adjust their swimming actions, to form a robust non-invasive cloak for any randomly moving intruder.

The implemented reinforcement learning algorithm was initially inspired by the concept of animal learning [136], and has been shown effective in learning previously unknown strategies, solely based upon the received feedback on performance [137]. The great potential of this approach has also been recently demonstrated in fish schooling [138], soaring of birds through turbulent environments [139], and flow navigation of gravitactic particles [140].

Here, we formulate the reinforcement learning algorithm as a Markov Decision Process (MDP). This allows us to use the Q-learning framework, which not only benefits from algorithmic simplicity, but also is proven [141] to converge to an *optimal* behavior policy. In this framework, the *agent* (here a micro-swimmer capable of decision-making) gradually learns the optimal behavior policy through exploring the environment (see Fig. 6.3a). At any given instance of time (the nth learning step), the agent is able to sense some information about

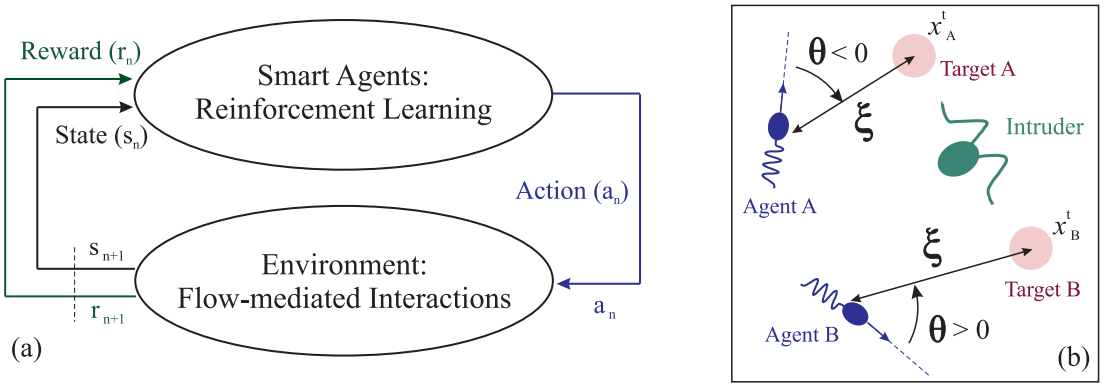

Figure 6.3: (a) Schematic representation of the reinforcement learning algorithm coupled with the presented flow-mediated interaction dynamics in viscous environments. (b) Schematic illustration of the state-space (ξ, θ), when two of our smart micro-swimmers (i.e. the agents A and B, shown here in blue) attempt to form a desired active cloak around a randomly moving intruder (shown in green).

the environment (referred to as the *state*, s_n), depending on which, it will choose an *action* (a_n) according to its current *policy* (π_n). Taking this action will then transit the agent to a new state (s_{n+1}), and it will be given a *reward* (r_{n+1}) quantifying its immediate success (Fig. 6.3a). The experience acquired by the agent (after going through each learning step) is stored as an action-value function, $Q(s, a)$, in the Quality matrix 'Q' – hence the name of algorithm. To be more precise, for any state-action pair (s_n, a_n), the Q-matrix encodes the expected sum of discounted future rewards when taking the action a_n at the current state (s_n) and following the current policy (π_n) thereafter; i.e.,

$$Q\left(s_n, a_n\right) = r_{n+1} + \gamma r_{n+2} + \gamma^2 r_{n+3} + \dots \ . \tag{6.7}$$

This Q-matrix is updated throughout the learning process, and is proven [141] to encode *optimal* action-value function (Q^*) at convergence. The optimal behavior policy ($\pi^* : s_n \rightarrow a_n$) is then readily available. To be more precise, in any given state (s_n), the optimal action (a_n^*) is the one that maximizes the expected sum of future rewards (which is encoded in Q^*). This policy (π^*), in fact, serves as the agent's adaptive decision-making intelligence.

Here, an off-policy control is implemented using the described Q-learning scheme. During the learning phase, an ϵ-greedy behavior policy has been employed to ensure exploration of new solutions while appropriately exploiting the gained knowledge. Specifically, at the n^{th} learning step, the policy ($\pi_n : s_n \rightarrow a_n$) is to choose the action (a_n) that maximizes current evaluation of the action-value function (Q). Except for a small probability (ϵ), in which case, a random action will be chosen (independent of Q) from the set of possible actions ($\mathcal{A}$) to

further explore the state-space; i.e.

$$a_n = \begin{cases} \arg\max_a Q(s_n, a) & \text{probability of } 1-\epsilon \\ \text{random action } a \in \mathcal{A} & \text{probability of } \epsilon \end{cases}. \tag{6.8}$$

After going through each learning step, the current estimation of the action-value function (Q) is then updated according to

$$Q\left(s_n, a_n\right) \leftarrow Q\left(s_n, a_n\right) + \alpha\left[r_{n+1} + \gamma \max_a Q\left(s_{n+1}, a\right) - Q\left(s_n, a_n\right)\right], \tag{6.9}$$

where the learning rate, $0 \leq \alpha \leq 1$, specifies the rate at which, previously learned experience is overwritten by the newly gained information. The discount factor, $0 \leq \gamma < 1$, determines to what extent the value of expected future rewards is incorporated into the agent's decision-making: for $\gamma \to 0$ ($\to 1$) its behavior will be myopic (farsighted) tending to maximize immediate (future) rewards. Here, the state-transition ($s_n \to s_{n+1}$), i.e. evolution of the system dynamics, is directly simulated taking into account the four-way coupled nature of the system through flow-mediated interactions (see section 6.2 for details). Once in the new state (s_{n+1}), the agent will then take another action, based on the updated policy, and the process will be repeated (Fig. 6.3a). Note that the updated action policy (π_{n+1}) in the new state will still be the same ϵ-greedy policy, yet based on the updated estimation of Q. Therefore, the behavior policy is continuously improved through the learning phase, and eventually converges to the optimal behavior policy ($n \to \infty : \ \pi_n \to \pi^*$). We then employ a purely deterministic (and greedy) behavior policy (i.e. with $\epsilon = 0$) for our cloaking agents, according to the obtained optimal action-value function, Q^*, to further assure the success of any assigned task.

Let us now consider the problem of cloaking arbitrarily moving intruders using pairs of swimming agents. In the following, we first outline a rigorous approach to equip our cloaking agents with adaptive decision-making intelligence – i.e. realizing the concept of *smart* micro-swimmers. As a benchmark, we consider puller intruders (say e.g. motile *C. reinhardtii* cells) swimming in an infinite two-dimensional fluid domain. Nevertheless, the results will be similar for pushers, and our study can be inherently generalized to a 3D domain. Each of the cloaking agents is modeled as a self-propelled micro-swimmer of the opposite type (here pushers) with a half-sized dipole strength ($\mathscr{D}/2$). We are particularly interested in realizing the *active* (and robust) form of the most effective cloak presented in section 6.3 (Fig. 6.2) – for which, $\eta > 99\%$ at $R/r_0 \geq 20$. Therefore, the approach is to position two cloaking agents symmetrically arranged (with a predefined separation distance r_0) on the sides of each intruder throughout its motion. This non-invasive cloak will effectively keep the enclosed swimmer hydrodynamically 'invisible' within the surrounding fluid.

In order to form this active cloak, our cloaking agents must learn optimal behavior policy in the presence of long-range hydrodynamic interactions. A pair of these smart micro-swimmers can then be assigned to cloak each of the randomly moving swimmers within any arbitrarily crowded suspension. The learning objective for each of these two cloaking

agents can be translated into two specific tasks: (i) learning how to optimally catch the assigned (randomly moving) intruder by forming a desired cloaking arrangement around it; and once reached to the target positions (e.g. points A and B in Fig. 6.3b), then (ii) learning how to keep on following the assigned intruder while robustly retaining the desired arrangement. Hereafter, we refer to these two consecutive learning tasks as to '*catch*' and '*follow*' a random intruder – both required in realizing an active cloak. Note that optimal execution of the former requires the cloaking agents to identify shortest non-invasive paths toward positioning themselves (from anywhere in the state space) into predefined desired arrangements around any moving subject.

To accomplish these tasks, each swimming agent can sense (or is provided with) an estimation of its distance and relative orientation with respect to the intruder. In practice, a range of imaging techniques [see 78] can be used to feed such information into the agent's decision-making unit. For instance, magnetic resonance imaging (MRI) has successfully been integrated into robotic platforms to provide the information required for real-time navigation of untethered micro-robots (or bacteria) swimming through human micro-vasculature [see e.g. 142, 79]. The acquired information by each agent, mathematically translates to the normalized distance $\xi = |\boldsymbol{x}^t - \boldsymbol{x}|/L_s$ and relative orientation θ with respect to the assigned target point, as depicted in Fig. 6.3(b) for the catching phase. This representation of the state-space is also consistent with previous studies (e.g. [138]) on swarm control of swimming agents. Note that once the agents successfully *catch* the intruder (by forming the desired cloaking arrangement around it), they still will need to *follow* the intruder, so as to actively keep the desired arrangement throughout its motion. Therefore, once in the cloaking positions, θ is defined as the deviation angle that each agent senses for its own swimming direction relative to the assigned intruder's.

Although the micro-swimmers are free to move in a continuous two-dimensional space, here we map the state-space, $s = (\xi, \theta)$, on a finite-size 2D pseudo-grid. This way of representing the state-space dramatically mitigates the curse of dimensionality, and makes the learning process computationally feasible. Also, from the practical point of view, the agents will then only need an estimation of their distance and deviation from their assigned target points. The required accuracy of such estimation is specified by the grid-size. Therefore, let us consider the discretized representation of our state-space ($\mathcal{S}$), which is the product of two finite-size subsets, i.e. $\mathcal{S} = \mathcal{S}_\xi \times \mathcal{S}_\theta$. Specifically, $\mathcal{S}_\xi$ represents the distance ξ as n_ξ discrete states within the range of $\Delta\xi$, and $\mathcal{S}_\theta$ indexes the angle θ as n_θ discrete states within the range of $\Delta\theta$. Hence, at every instance of time (t_n), the state of an agent is represented by a tuple $s_n = (\xi_n, \theta_n)$, where

$$\xi_n = \min\,(\Delta\xi,\ \lfloor \xi n_\xi/\Delta\xi \rfloor \cdot \Delta\xi/n_\xi), \tag{6.10a}$$

$$\theta_n = \min\,(\Delta\theta,\ \lfloor \theta n_\theta/\Delta\theta \rfloor \cdot \Delta\theta/n_\theta). \tag{6.10b}$$

For instance, here we set $n_\xi = 100$, $\Delta\xi = 50$, $n_\theta = 36$, and $\Delta\theta = 2\pi$. This means a total of 3,600 discrete possible states for each agent.

The deployed cloaking agents are able to swim in three distinct speeds: v^0 (nominal), $v^+ = v^0 + \delta v$ (fast), and $v^- = v^0 - \delta v$ (slow). They can also instantly turn to right

($\theta \leftarrow \theta + \delta\theta$) or left ($\theta \leftarrow \theta - \delta\theta$) with different choices of angle $\delta\theta$. Therefore, the motion of each swimming agent during the learning process can be described as a repeated occurrence of the following two-step process: (i) the agent updates its swimming velocity (through either a change in orientation by $\delta\theta$, or a modification in speed by δv) according to the current policy; and then (ii) it moves with the new velocity for a fixed time τ_r (=1 in non-dimensional time units scaled by $T_s = L_s/v^0$). Note that each agent takes an *exclusive* swimming action (e.g. turning to the right/left with an angle $\delta\theta$, or speeding up/down with δv) based on the current policy (π_n), at intervals of τ_r during the learning process. Once an action is taken, the agent swims steadily forward (i.e. 'runs'), until a new action (potentially a change in orientation, i.e. 'tumbling') is taken after τ_r. This is inspired by the observed behavior of natural swimming microorganisms, and is reminiscent of the so-called *run-and-tumble* locomotion. In practice, realization of the smart version of this locomotion dynamics seems also feasible in the context of artificial and model micro-swimmers. The recently proposed Quadroar swimmer [15, 12], for instance, propels on straight lines (runs), and can perform full 3D reorientation (tumbling) maneuvers [10].

Here, the nominal swimming speed for the agents is set to that of the intruders (i.e. $v^0 = v_s$), and we consider $\delta v = 0.05\ v^0$ ($0.5\ v^0$) while following (catching) an intruder. Nevertheless, our numerical experiments reveal that a learned policy (under this specification) can be readily adopted by agents with different speed characteristics (v^0, δv), and so in cloaking intruders with various swimming speeds (see Appendix A.1 for details). Furthermore, the space of possible values for $\delta\theta$, inherently covers the entire range of $[0, \pi]$. However, selecting only a finite-size set of options for $\delta\theta$, substantially reduces the computational costs associated with the recurrent identification of optimal actions, during the reinforcement learning process. Therefore, here we assume the agents are only able to turn right/left with $\delta\theta \in \{\pi/18, \pi/4, \pi/2\}$. This finite-size simplified set is particularly devised to provide each agent with the ability to: (i) make major changes in the swimming direction (with $\delta\theta = \pi/2$), typically done in early stages of a catching process; (ii) perform moderate re-orientations (with $\delta\theta = \pi/4$) commonly used during a catching process; and (iii) fine tune slight deviations from a desired orientation (with $\delta\theta = \pi/18$), which is particularly required at final stages of a *catching* process or while *following* an intruder. Therefore, our set of possible actions ($\mathcal{A}$) consists of nine specified swimming actions. This, along with the described discretized state-space, result in 32,400 entries for the space of state-action pairs, to be used in evaluating the action-value function $Q(s_n, a_n)$. We note that the frequency of taking an action by each agent (i.e. τ_r^{-1}) can also be tuned according to the system of interest.

For the swimming agents, realization of an active cloak around an arbitrary intruder is translated into taking an optimal sequence of actions to actively catch and follow the assigned target points in a predefined arrangement. The immediate success of each agent in satisfying this assigned task is mathematically interpreted as a numerical reward signal

$$r_n = [1/(\xi_n + \delta\xi) - \xi_n] + [\delta(v_n - v^0) - 1] + \mathscr{C}_n + \mathscr{P}_n, \tag{6.11}$$

where $\delta\xi$ is the system precision (i.e. the grid-size) in measuring the distance. The $\delta(x)$ is defined such that $\{\delta(x) = 0 \mid \forall x \neq 0\}$ and $\delta(0) = 1$. In our reward signal definition, the first

term reflects how well the agent is following (or catching) an assigned target point, while the second term penalizes any unnecessary speed-ups or -downs. This penalty is assigned because the dipole strength of the swimmers is directly proportional to their swimming speed ($\mathscr{D} \sim v_s l_s^2$), and thus any change in the value of swimming speeds can disturb the balance of dipole strengths. However, the relative value of these speed modifications is kept negligibly small (here e.g. $\delta v/v^0 = 0.05$) while the agents are actively cloaking an intruder (i.e. robustly following it in a predefined arrangement). Contribution of the third term in the reward signal ($\mathscr{C}_n$) is two-folded: (i) it encourages the agent to accurately get into the assigned target point once fairly close (here e.g. $\mathscr{C}_n = 100$ when $|\boldsymbol{x}^t - \boldsymbol{x}| \leq \delta\xi$), and (ii) it strictly penalizes wandering of the agent far off the target (here e.g. $\mathscr{C}_n = -100$ when $|\boldsymbol{x}^t - \boldsymbol{x}| \geq \Delta\xi$). Finally the last term, $\mathscr{P}_n = -\cos^{-1}(\boldsymbol{e}\cdot\boldsymbol{e}^i)$, ensures that the agents learn how to smartly collaborate in a way that their induced disturbing flows do not disturb the cloaked object (i.e. the intruder) from its original path ($\boldsymbol{e}^i$) – hence, encouraging the realization of a *non-invasive* active cloaking.

It is to be noted that realizing an active cloak around the assigned intruder, as the ultimate goal of this learning algorithm for each agent, is mathematically encoded as achieving maximal long-term *accumulated* rewards. Therefore, negative nature of the reward signal r_n (6.11) further ensures that our cloaking agents learn the shortest paths toward positioning themselves in the desired cloaking arrangement – as taking any unnecessary action will result in an extra accumulation of negative rewards.

Here, the cloaking agents are trained in pairs, and we employ a shared policy approach among them to accelerate the learning process. Training is conducted through consecutive learning episodes, denoted by $E = 1, 2, \ldots, n_E$, where n_E is the total number of episodes in the learning phase. Each episode starts with an intruder randomly entering a guarded (sensitive) region – i.e. from a random position and toward a random direction. The cloaking agents are also initially located on either side of the entrance (see Figs. 6.4 and 6.5). The first episode ($E = 1$) is initialized by zero entries for all elements of the Q-matrix (i.e. an optimistic initialization) to further encourage exploration of new solutions and avoid trapping in local optima – recall the negative nature of the reward signal. For the subsequent episodes ($E = i + 1$, $i \geq 1$), the action-value function, Q, will be initialized by that obtained at the end of previous episode (i.e. $E = i$). The end of each training episode is declared when: either (i) the agents have formed a desired cloak around the intruder – i.e. when they both have reached to the assigned target points in a predefined arrangement (see e.g. Fig. 6.5c); or (ii) a certain number of state changes has passed without any success (e.g. $N_{s,\max} = 250$ in Fig. 6.4). The process is in turn repeated until the action-value function coverages to an optimal value (i.e. $Q_n \to Q^*$ as $n_E \to \infty$) – or practically, when the policy (π_n) converges to the optimal behavior policy ($\pi_n \to \pi^*$).

To assess the learning process at different stages, we run a set of 100 random active-cloaking tests throughout the training phase – here, specifically after every 1000 learning episodes. In testing the agents' intelligence, we deploy a purely deterministic (greedy) policy (i.e. $\epsilon = 0$) based on the most-updated acquired Q-matrix. During each of these testing episodes, the agents are subject to cloak a random intruder using their so-far gained ex-

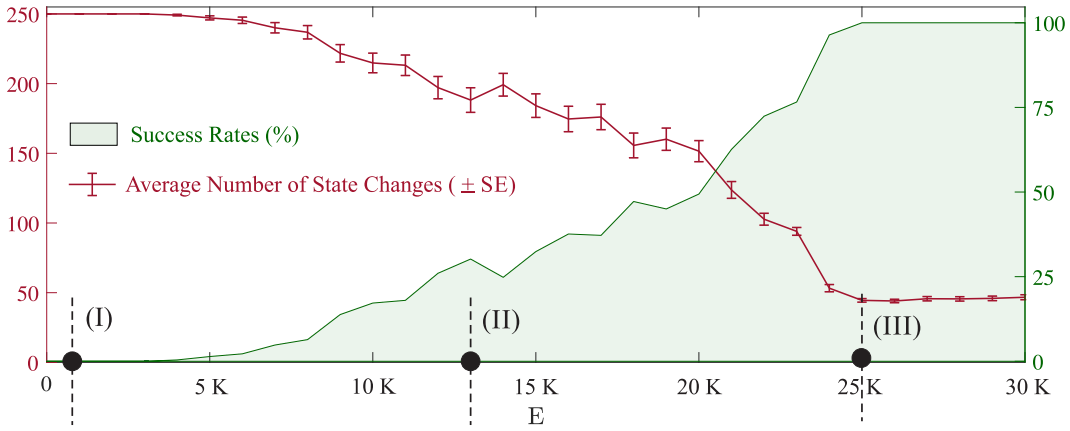

Figure 6.4: The learning process is assessed in terms of the agents' success rate, and number of the required swimming actions. After every 1000 training episodes, a set of 100 random active-cloaking tests have been performed using a purely deterministic policy based on the most updated Q-matrix at the moment. Each of the testing episodes starts with an intruder randomly entering a guarded region (shaded in gray; see Fig. 6.5) from a random position and swimming toward a random direction, while the cloaking agents are initially positioned on the sides of entrance (see the samples presented in Fig. 6.5). The test results are presented throughout the learning phase in terms of: (i) the success rate (shown in green) of the agents in catching the intruders and forming the desired active cloak, as well as (ii) the number of total state-changes (average ± Standard Error) in each set of testing episode (shown in red). Here, the learning hyper-parameters are set to $\alpha = 0.3$, $\gamma = 0.95$, and $\epsilon = 0.01$.

perience (encoded in the given Q-matrix). For each set of the (100) performed tests, we then compute the average number of total state-changes (N_s), along with success rate of the agents in catching the intruders and forming desired active cloaks. Both measures are monitored throughout the learning phase as demonstrated in Fig. 6.5. The learning is evident in the gradual increase (decrease) of the agents' success rate (required number of swimming actions) in collaborative formation of the desired active cloak around random intruders (Figs. 6.4 and 6.5). As a benchmark, we also demonstrate, in panels (a)-(c) of Fig. 6.5, a specific sample test performed in three different learning stages – the corresponding episode numbers (E) are marked in Fig. 6.4 as (I)-(III). While the agents are too naive at early stages (e.g. Fig. 6.5a) and fail to catch and cloak the subject, they eventually learn how to actively cloak the moving intruder through an optimal set of non-invasive actions (e.g. Fig. 6.5c). Note that both of the monitored measures (i.e. the success rate and the number of swimming actions required to form a desired cloak) eventually converge to their optimal values as the number of learning episodes increases sufficiently (here, after $E \sim 25,000$). The converged value of 100% success rate for the cloaking agents, clearly shows their ability to smartly form a non-invasive active cloak around any randomly moving intruder (see e.g. the samples presented in Fig. 6.5 d-f). In doing so, they find shortest non-invasive paths using only their

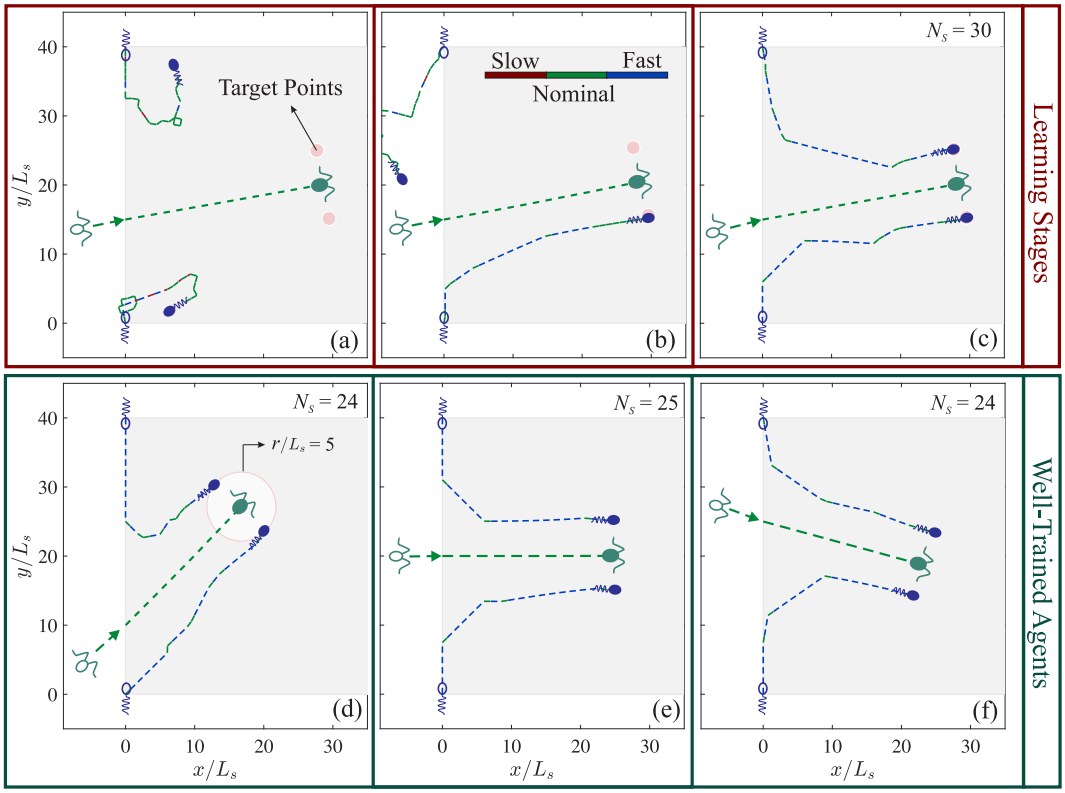

Figure 6.5: **(a)-(c):** Benchmark samples of different stages in the learning process (presented in Fig. 6.4). The panels represent a sample test to realize active cloaking around a random intruder, performed in three different learning stages, i.e. non-adaptive (a), intermediate-adaptive (b), and well-adaptive (c) stages. The episode number (E) corresponding to each of the panels (a-c) is marked in Fig. 6.4 (I-II-III), and agents use the most updated behavior policy at each stage. The intruder (here a puller shown in green) and the cloaking agents (pushers shown in blue) are also represented both at the initial and final positions with stripe and solid schematics, respectively. Trajectories of the swimmers are shown in each panel by dashed lines, and color-coded based on the swimming speed at the moment – see the legend in panel (b). The assigned target points (to realize the desired symmetrical active cloak) for each of the agents is also marked in each panel (pink markers). **(d)-(f):** Sample tests performed using well-trained cloaking agents, equipped with well-adaptive behavior policy, which is obtained after convergence of the success rate to 100% (see Fig. 6.4). The number of required swimming actions (or equivalently the number of state-changes, N_s) is denoted on each panel. The target arrangement here is to symmetrically position on the sides of intruder, with a separation distance $r_0/L_s = 5$ (see e.g. panel d). The learning hyper-parameters are set to $\alpha = 0.3$, $\gamma = 0.95$, and $\epsilon = 0.01$.

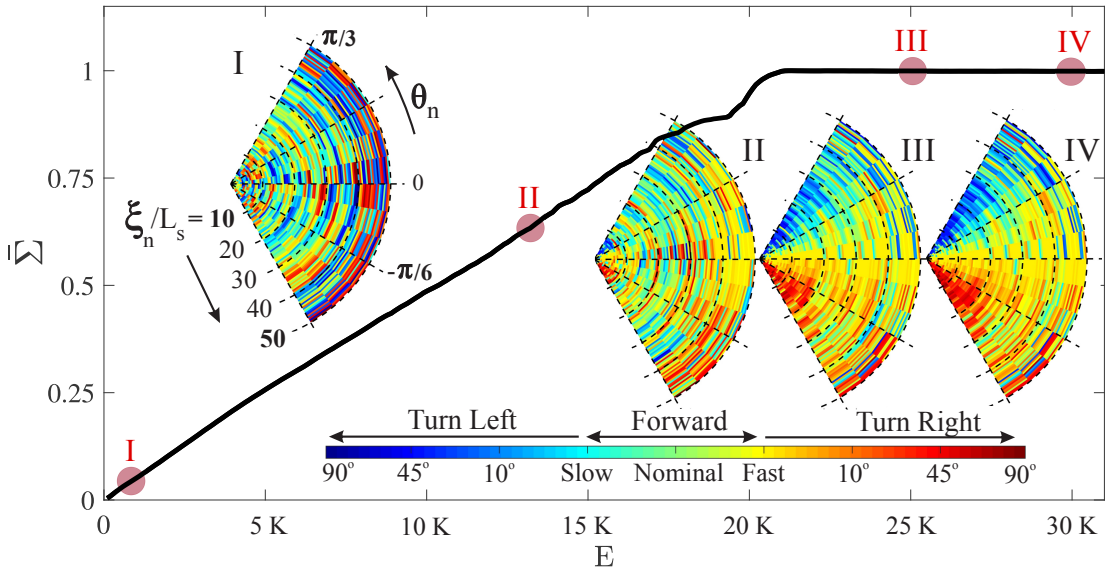

Figure 6.6: Evolution of the normalized element-wise sum of the Q-matrix ($\bar{\Sigma}$) through successive training episodes (E) during the learning phase. The agents' behavior policy is also visualized (see insets I-IV) by color-coding over a selected sector of the state-space. Its evolution is monitored at four different learning stages (marked over the curve by I-IV), and eventually converges to the optimal behavior policy. Here, each swimming action is presented by a color-code (see the color-bar legend), and every point in the state-space is shaded by a color representing the agents' current understanding of the best action at that specific state. The training episodes are the same as those presented in Figs. 6.4 and 6.5, for which the learning hyper-parameters are set to $\alpha = 0.3$, $\gamma = 0.95$, and $\epsilon = 0.01$.

own adaptive decision-making intelligence – hence, the name *smart* micro-swimmers.

Convergence of the cloaking agents' adaptive decision-making intelligence (encoded in the Q-matrix) is better demonstrated in Fig. 6.6, where we show evolution of the element-wise sum of the Q-matrix (Σ), normalized by its converged value. Additionally, the experientially learned behavior policy is visualized by color-coding over a sector of the state-space, in four different learning stages (marked in Fig. 6.6 by I-IV). Here, convergence of the action-value function (and thus the behavior policy) is achieved when the number of successive training episodes (E) exceeds $\sim 25,000$ (Figs. 6.4 and 6.6).

Once the learning process is converged, the cloaking agents are readily equipped with an *optimal* behavior policy. To be more precise, the optimal behavior policy refers to the policy ($\pi^* : s \rightarrow a$) that in any given state (s), determines the action (a) which maximizes the expected sum of future rewards (encoded in Q^*). Here, the reward signal (r_{n+1}) received (during the learning process) by the agents after taking an action (a_n), has two salient features – c.f. Eq. (6.11): (i) it reflects a penalty for disturbing the intruder from its original path, and (ii) it is designed to always have a negative value, except at the target

state. Therefore, maximizing the discounted sum of future rewards will ensure, not only to successfully realize the desired non-invasive cloak, but also to do so with minimum number of actions (Fig. 6.4). Note that spending more time (by taking excessive actions) will simply result in accumulating more negative rewards, which is discouraged by the optimal policy. This enables the agents to find *shortest* non-invasive paths toward positioning themselves in desired cloaking arrangements around arbitrarily moving intruders (see e.g. the samples presented in Fig. 6.5 d-f).

However, there is still a caveat here: the presence of long-range flow-mediated interactions, if not responded adaptively by taking proper swimming actions, will soon distort the arrangement and reveal the cloaked object. Our swimming agents, however, have been trained not only to '*catch*' and form desired cloaks around random intruders, but also to '*follow*' them robustly, while maintaining the implemented cloak throughout their motion. As a benchmark, let us monitor the time evolution of a sample crowded suspension of intruders (Fig. 6.7), where the deployed pairs of our smart micro-swimmers have already formed the desired cloak around each of the subjects – see the examples presented in Fig. 6.5. Periodic boundary conditions are imposed on the presented panels, as if they represent just a window of an infinite domain of suspension. Such a complex random system is mainly characterized by each of the swimmers moving toward a random direction in space (Fig. 6.7a), with frequent close encounters happening between them (e.g. Fig. 6.7b-c). It worths noting that even an isolated intruder, swimming (alone) on a straight line in an unbounded domain, can distort the arrangement of an implemented cloak, and cause naive cloaking agents to diverge or collapse. The situation here is further exacerbated by the presence of other nearby swimmers, given their disturbing flows and long-range flow-mediated interactions – let alone

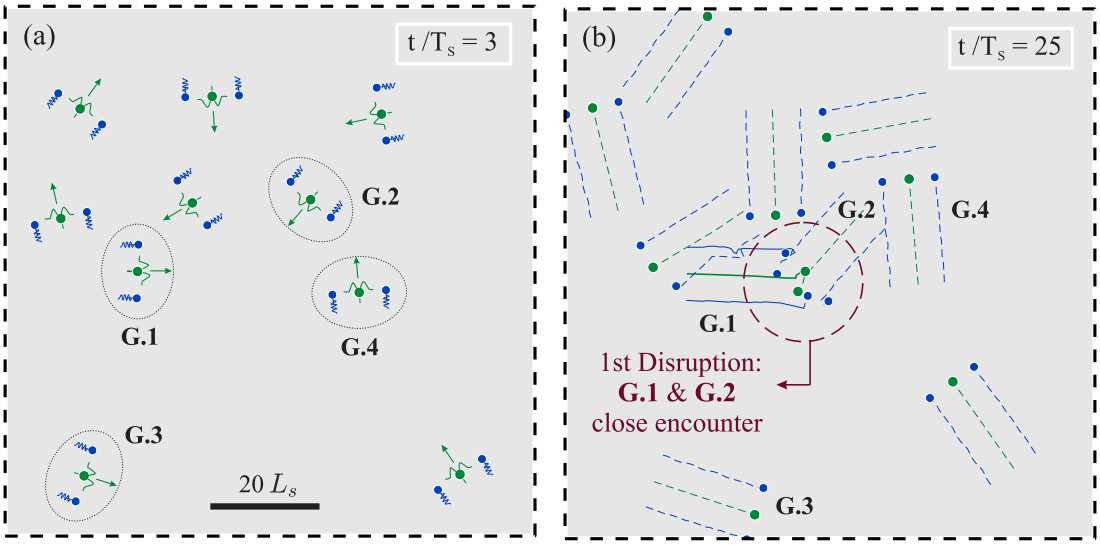

Figure 6.7: For caption see next page.

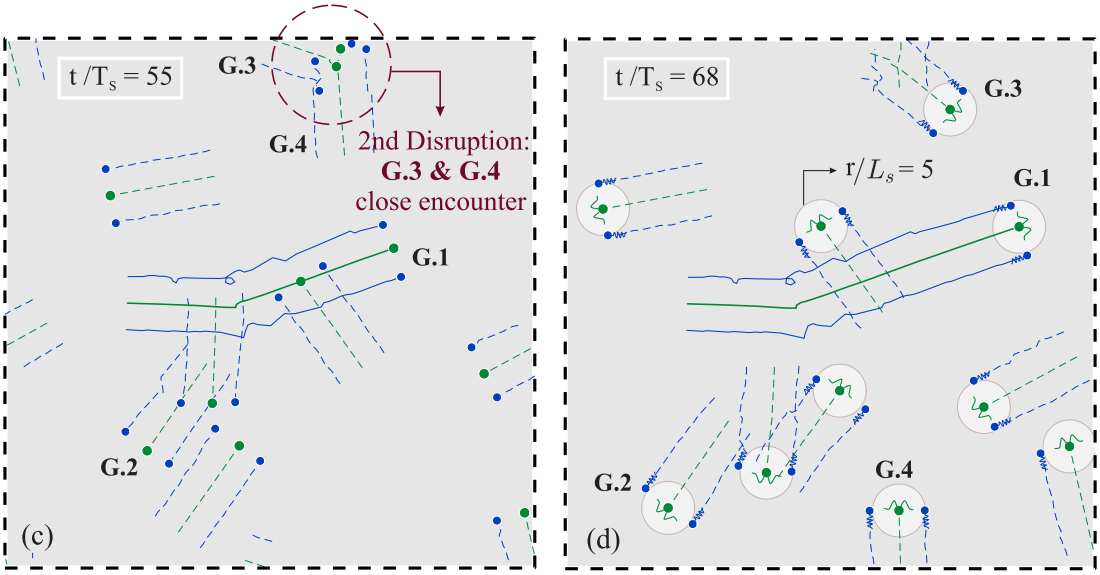

Figure 6.7: (cntd). Time evolution of a crowded suspension of intruders (shown in green), each of which actively cloaked by a pair of smart micro-swimmers (shown in blue). Here the intruders are freely moving toward random directions in space – specified by green arrows in (a). Periodic boundary conditions are imposed on the presented panels – i.e. each panel represents just a window of an infinite domain at that specific moment. As demonstrated through snapshots (a)-(d) of the system's time evolution, using their adaptive decision-making intelligence, our agents are able to robustly maintain the cloak formation in the presence of complex hydrodynamic interactions. They are also able to immediately restore the desired formation after any severe close encounters (b-c) which cause major disruptions to the cloak. As a benchmark, the evolution dynamics of four sample groups (G.1-4) are tracked in the panels. Specifically, the close encounter between G.1 and G.2, as well as G.3 and G.4, are marked by red dashed circles in panels (b) and (c), respectively. Also, trajectories of the swimmers in G.1 are shown by solid lines throughout the time, while other groups' trajectories are only demonstrated (by dashed lines) within the last $25T_s$ of their motion. The time corresponding to each snapshot is noted in each panel, and swimmer schematics are added to panels (a) and (d) for readability. Here, the goal was to realize an active version of the symmetric cloak presented in Fig. 6.2. Thus, for the reference, rings of radii $r/L_s = 5$ (that is equal to the predefined desired separation distances) are depicted around intruders in the final snapshot (d).

close encounters happening in such a crowded system, and the consequent disruptions in cloak arrangements. However, as it is evident throughout the system evolution, the proposed *smart* active cloaking strategy is robust. In particular, by taking optimal adaptive swimming actions, the cloaking agents not only successfully retain their arrangement in the presence of hydrodynamic interactions, but also immediately re-form the desired cloaking arrangements after any sudden disruption (Fig. 6.7).

In practice, it is often of interest to conceal a single micro-swimmer (e.g. a biological micro-robot) within a crowded suspension (e.g. inside the human body) using only a pair of cloaking agents. However, for the sake of generality, here we have used a *flock* of cloaking agents to cloak all the (randomly moving) swimmers in the presented crowded suspension (see Fig. 6.7). To assess performance of the deployed flock in concealing the assigned swimming objects, we then monitor the overall cloaking efficiency ($\eta\%$) throughout the system's time evolution (Fig. 6.8a). The magnitude of disturbing flows (i.e. flow signatures) induced by the system is also monitored throughout the represented time evolution, and is compared to the same system when no cloaking agents are deployed (Fig. 6.8 b-e).

The implemented cloaks are dynamically adjustable, as the cloaking agents behave adaptively in response to fluid-mediated interactions. This enables them to robustly keep their specified arrangement, and actively conceal any moving subject throughout its motion (see e.g. Fig. 6.7). Not to mention that the agents first need to smartly collaborate in pairs and find optimal paths to separately catch each of the assigned subjects (see the samples in Fig. 6.5) forming an active set of perfect cloaks (with $\eta > 98\%$) around these randomly moving intruders (Figs. 6.7a, 6.8b). Once realized, throughout the system evolution, the cloaking efficiency remains well above 75% even in the presence of non-linearly varying complex flow-mediated interactions (Fig. 6.8a). The two relatively notable sudden drops in the cloaking performance (i.e. to $\eta \sim 70\%$) occur right after the reported close encounters, which cause major disruptions to the cloaks' arrangements (Fig. 6.7 b-c, Fig. 6.8 c-d). However, the implemented active cloaks are robust, thus are immediately re-formed and the cloaking efficiency is quickly recovered. For instance, note the final stage (Figs. 6.7d, 6.8e) with a remarkable 93% cloaking efficiency, that is recovered after going through many interactions and encounters. It is noteworthy that the deployed flock of cloaking agents have never been trained for, neither exposed to, this (or any other) specific scenario with *multiple* intruders. This means that once the agents undergo the described *catch* and *follow* training processes (see Figs. 6.4 and 6.5), they can be readily used in pairs to actively cloak any number of arbitrary intruders within unexposed crowded suspensions.

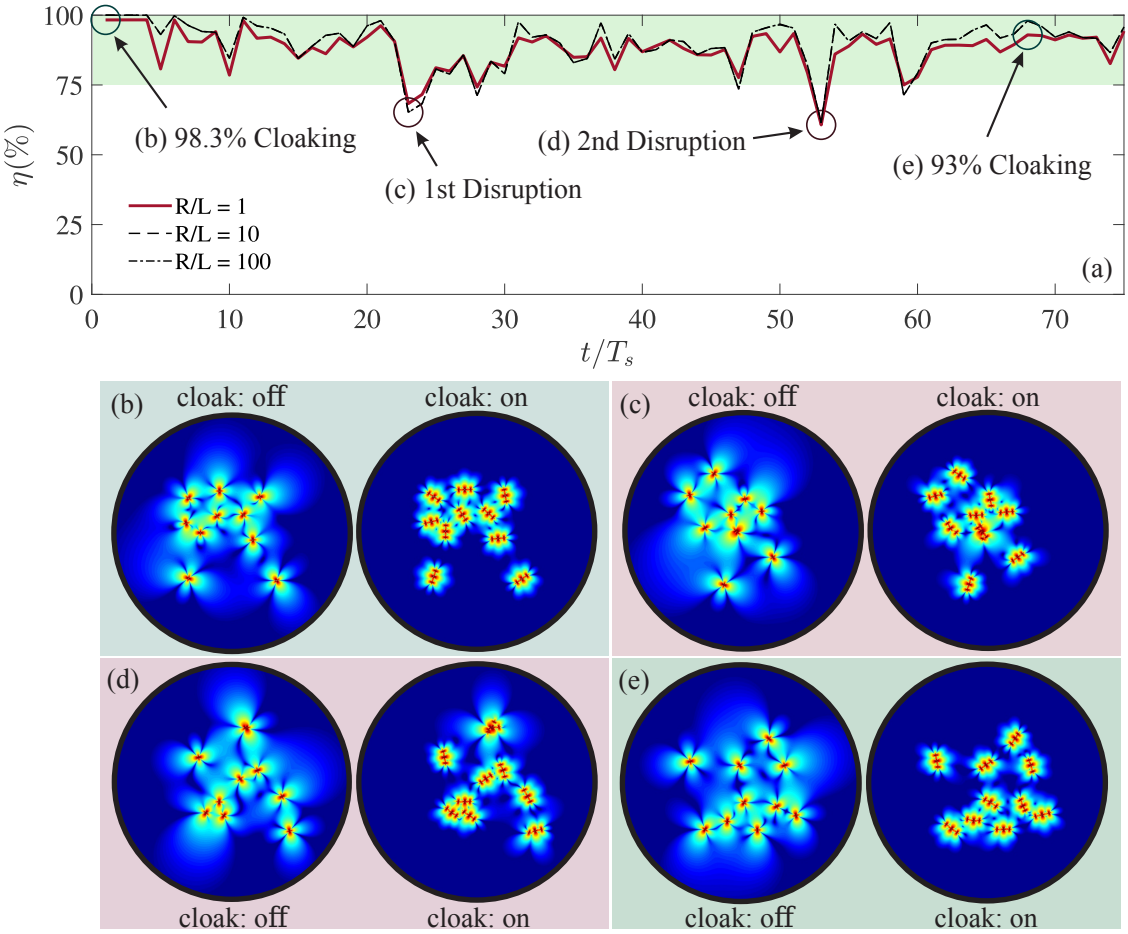

Figure 6.8: **(a)** Time evolution of the overall cloaking performance ($\eta\%$) corresponding to the flock of smart micro-swimmers deployed within the crowded suspension presented in Fig. 6.7 to cloak random intruders. Here η (%) is monitored over the entire time evolution at ranges $R/L = 1$ (red solid line), $R/L = 10$ (black dashed line), and $R/L = 100$ (black dash-dotted line), where L is the length of each presented window in Fig. 6.7. **(b-e)** Snapshots of the induced fluid disturbances are visualized (by color shading) over the entire system (cloak: on), and also compared to those induced when no cloaking agents are deployed (cloak: off). The moment corresponding to each of the snapshots in (b-e) is marked on the curve in (a). Specifically, we demonstrate the snapshots at: (i) an early stage, where the desired cloaks ($\eta \approx 98\%$) have been just formed (Figs. 6.7a, 6.8b); (ii) the moments of close encounters happening between G.1 & G.2 (1st Disruption, see Figs. 6.7b, 6.8c) as well as G.3 & G.4 (2nd Disruption, see Figs. 6.7c, 6.8d), respectively, where the implemented cloaks undergo severe disruptions; and (iii) a final recovered stage (Figs. 6.7d, 6.8e) where the agents are once again perfectly in the desired cloaking arrangements ($\eta \approx 93\%$).

6.5 Other Notes

6.5.1 On the Generality of a Learned Policy

As discussed in section 6.4, the reinforcement learning process will equip our cloaking agents with an adaptive decision-making intelligence. A flock of these smart micro-swimmers can then be readily used to actively cloak any number of arbitrarily moving intruders, within any unexposed crowded suspension (see e.g. Figs. 6.7-6.8). However, it still remains unclear to what extent a learned policy can be effective once used: (i) by agents with different swimming speeds, and/or (ii) for cloaking intruders of various swimming speeds.

Let us consider the optimal policy (π^*) obtained specifically for the agents with $\delta v/v^a = 0.5$, through episodes of catching intruders swimming in random directions with the speed of $v^i/v^a = 1$ (see e.g. Figs. 6.4, 6.5, and 6.6). The generality of this policy is assessed in Fig. 6.9 over the parameter-space (v^i/v^a, $\delta v/v^a$). In particular, for every point in the presented parameter-space (i.e. corresponding to each specific choice of v^i/v^a and $\delta v/v^a$), we run a set of 25 random active-cloaking tests (similar to those demonstrated in Fig. 6.5). The results of our numerical experiments (presented in Fig. 6.9) reveal a wide range of ideal applicability (region I), within which the learned policy is fully effective (with a success rate of 100%) in cloaking random intruders. This almost covers the entire parameter-space, except the cases with $v^i > v^a + \delta v$ (region II), for which catching the intruder is not physically feasible, followed by a transition zone (region III).

Our numerical experiments also reveal that the agents equipped with a learned behavior policy, can be readily deployed to realize any other form of cloaking arrangements around a random intruder. Here, as a benchmark, we demonstrate how our smart agents can be readily used in *triple-* or *quadruple-agent* cloaking strategies (Fig. 6.10). Note that when a pair or multiple micro-swimmers perform active cloaking, the state space is defined for *each* agent independently. To be more precise, the state space for each agent includes its distance and relative orientation with respect to the intruder, while all the agents use a shared action policy. It is to be highlighted that the policy (π^*) adopted by agents in the presented triple- and quadruple-agent cloaking test cases (Fig. 6.10), is the one obtained through consecutive learning episodes of *double-agent* cloaking (demonstrated in Figs. 6.4-6.6). Therefore, the deployed agents have no prior experience in forming such three- or four-agent cloaks.

6.5.2 On the Design of a Reward Signal

In the reinforcement learning process, actions taken by an agent are rewarded with a feedback signal (r_n) that quantifies immediate success in achieving a predefined objective. This form of feedback on performance is the only information that agents receive throughout their interaction with the environment. For them, the learning objective is to maximize the sum of accumulated rewards, which should properly reflect the ultimate *physical* objective. This makes the design of a proper reward signal a challenge for any reinforcement learning process.

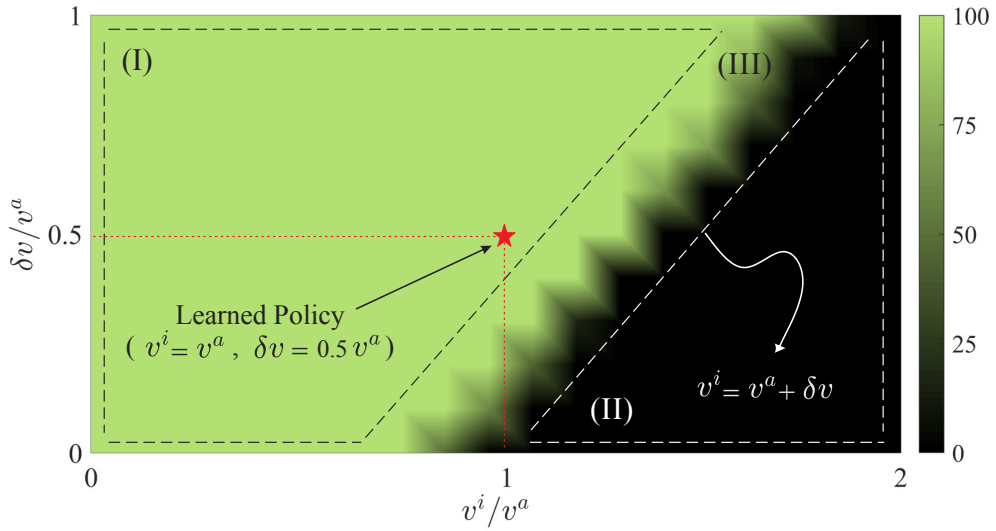

Figure 6.9: Applicability of a learned policy (measured in terms of the success rate) in cloaking intruders with various swimming speeds (v^i), once adopted by agents with different speed characteristics (i.e. v^a and δv). The employed policy (π^*) is specifically the one learned by agents with $\delta v/v^a = 0.5$, through episodes of catching intruders swimming in random directions with the speed of $v^i/v^a = 1$ (see Figs. 6.4 and 6.5). The corresponding reference point is marked (with a red asterisk) on the parameter-space (v^i/v^a, $\delta v/v^a$). To assess the generality of this policy, we run a set of 25 random active-cloaking tests (similar to those demonstrated in Fig. 6.5) for every point in the presented parameter-space (i.e. corresponding to each specific choice of v^i/v^a and $\delta v/v^a$). Color shading represents success rate of the deployed agents (equipped with the same π^*) in forming desired cloaks (i.e. the one with $\beta = \pi/2$ and $\psi = \pi$ in Fig. 6.2) around the corresponding randomly moving intruders. Three distinct regions can be identified in the parameter-space: (I) the region of ideal applicability within which the learned policy is fully effective with a success rate of 100%, (II) the region associated with $v^i > v^a + \delta v$, for which catching the intruder is not physically possible, and (III) a transition region.

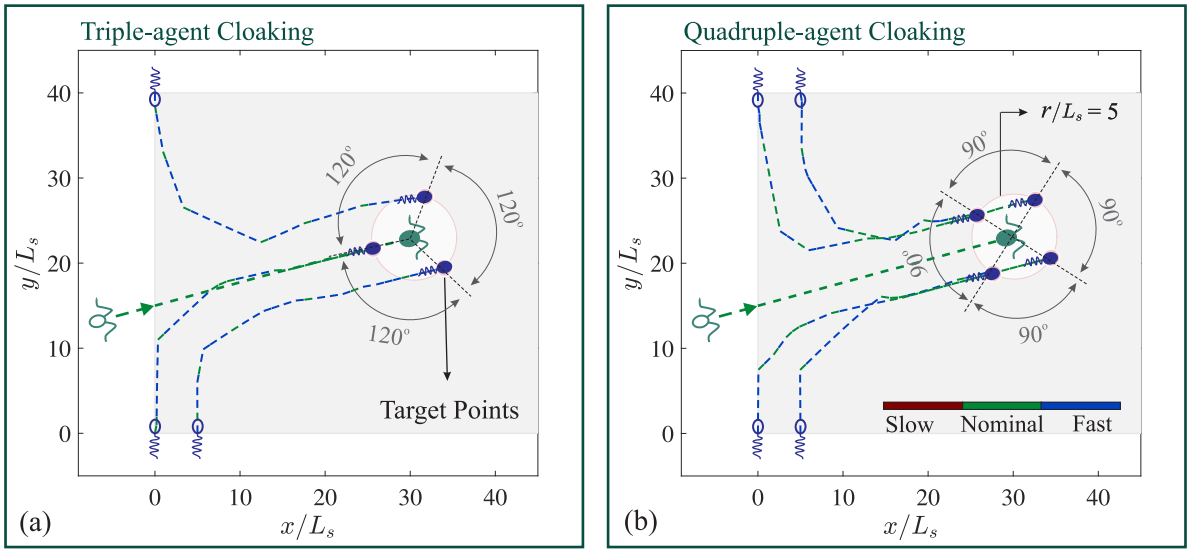

Figure 6.10: Applicability of a learned policy in realizing multi-agent active cloaks for random intruders. Here, the employed policy (π^*) is the one obtained through consecutive learning episodes of *double-agent* cloaking, as demonstrated in Figs. 6.4 and 6.5. Once the agents are equipped with this behavior policy, they can be readily deployed to form any other forms of cloaking arrangements around random intruders. Here, as a benchmark, we demonstrate samples of triple- and quadruple-agent cloaking strategies in panels (a) and (b), respectively. Similar to those presented in Fig. 6.5, each testing episode starts with an intruder entering a guarded region (shaded in gray) from (toward) a random position (direction), while the cloaking agents are initially positioned on the sides of entrance. The intruder (here a puller, shown in green) and the cloaking agents (pushers shown in blue) are also represented both at the initial and final positions with stripe and solid schematics, respectively. Trajectories of the swimmers are shown in each panel by dashed lines, and color-coded based on the swimming speed at the moment – see the legend in panel (b). The assigned target points for each of the agents (to realize the desired symmetrical active cloaks) are also marked in each panel (with pink markers). Note that the agents (equipped with optimal behavior policy) are capable of identifying the shortest non-invasive paths toward forming any desired active cloak around any randomly moving intruder. The target arrangements here are symmetric configurations, achieved by positioning three (a) or four (b) agents around the subject, with a separation distance of $r_0/L_s = 5$ (denoted by a pink circle around the intruder).

Here, the ultimate goal for the agents is to obtain the ability to identify optimal (i.e. shortest) non-invasive pathways toward positioning themselves into desired cloaking arrangements, around any arbitrarily moving intruder. In section 6.4, we devised a reward function (6.11) composed of four elements, each meticulously encoding a particular aspect of this objective into the feedback signal received by the agents. Here, we further explore robustness of the presented learning approach against excluding each of those elements from the proposed signal. To this end, let us consider the following set of alternative reward functions:

$$r_n^{(1)} = [1/(\xi_n + \delta\xi) - \xi_n] + [\delta(v_n - v^0) - 1] + \mathscr{C}_n + \mathscr{P}_n \ , \tag{6.12a}$$

$$r_n^{(2)} = [1/(\xi_n + \delta\xi) - \xi_n] + [\delta(v_n - v^0) - 1] + \mathscr{C}_n \ , \tag{6.12b}$$

$$r_n^{(3)} = [1/(\xi_n + \delta\xi) - \xi_n] + [\delta(v_n - v^0) - 1] \ , \tag{6.12c}$$

$$r_n^{(4)} = [1/(\xi_n + \delta\xi) - \xi_n], \tag{6.12d}$$

$$r_n^{(5)} = -1 \ , \tag{6.12e}$$

where $r_n^{(1)}$ is the original reward signal (used throughout this work), and $r_n^{(2)}$ to $r_n^{(5)}$ are the ones obtained through systematic elimination of the constitutive elements from $r_n^{(1)}$. As discussed in section 6.4, the first term of the original reward signal (i.e. $r_n^{(1)}$) reflects how well each agent is following (or catching) an assigned target point. The second term is to penalize any unnecessary speed-ups or -downs by the agents, and thereby further encourages them to keep the dipole-strength in balance. The third term in the signal has two main contributions: (i) it encourages each agent to get into the precise position of an assigned target point (once in its close proximity), and (ii) it strictly penalizes wandering of the agents far away from their target points. Finally, the last term ensures that the agents learn how to smartly collaborate in a way that their induced flow fields do not disturb the cloaked object (i.e. the intruder) from its original path – hence, realizing *non-invasive* active cloaking. We also note that the negative nature of the presented reward signals further ensures that our cloaking agents learn the *shortest* paths toward positioning themselves in the desired cloaking arrangement – as taking any unnecessary action will result in an extra accumulation of negative rewards, which is discouraged by the algorithm.

Here we repeat the learning process, using each of the proposed alternative feedback signals. Similar to the original process (demonstrated in Figs. 6.4 and 6.5), alternative learning processes are then independently assessed (Fig. 6.11) via running random sets of 100 active-cloaking tests after every 1000 training episodes. The results further suggest robustness of the presented methodology against excluding different elements from the devised reward signal ($r_n^{(1)}$). However, there is a caveat here: each of the described components, are included to quantify the agents' success in achieving a particular aspect of their ultimate goal. Failing to provide an explicit feedback on any of these aspects, makes the learning process substantially longer, and thus significantly increases the computational costs. For instance, by eliminating the last term from the reward signal $r_n^{(1)}$, the agents will no longer receive an explicit (negative) feedback when disturbing the intruder. As a result, it takes a significantly larger number of trial-and-errors (i.e. training episodes) for them to learn that

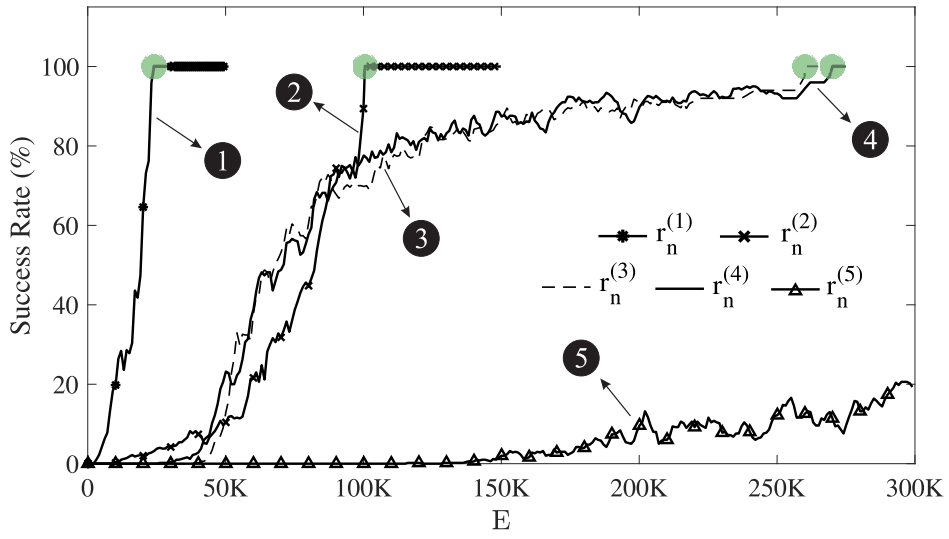

Figure 6.11: The learning process repeated for each alternative reward signal, $r_n^{(1)}$ to $r_n^{(5)}$, is assessed in terms of the agents' success rate. Similar to the original process demonstrated in Figs. 6.4 and 6.5, a set of 100 random active-cloaking tests have been performed after every 1000 training episodes, where the agents use a purely deterministic (greedy) policy based on the most updated Q-matrix at the moment. Results are presented for each case throughout the corresponding learning process, in terms of the success rate of the agents in catching the random intruders and forming desired active cloaks. The target arrangement is defined similar to the original process, that is the symmetric double-agent cloaking with a separation distance of $r_0/L_s = 5$. Learning hyper-parameters are also kept the same – i.e. $\alpha = 0.3$, $\gamma = 0.95$, and $\epsilon = 0.01$. Here, the learning processes represented by curves (1)-(4) have converged (as marked in green) to the 100% success rate after $\sim$ 25000, 100000, 260000, and 270000 training episodes, respectively. Note that curve (1) corresponds to the originally proposed learning process, also presented in Fig. 6.4.

such a behavior is sub-optimal – as it will increase the number of actions (and thus the time) required to catch an intruder. Therefore, performance of the agents trained by the reward signal $r_n^{(2)}$ requires $\sim$ 100,000 learning episodes to converge to the 100% success rate (Fig. 6.11), which is significantly higher than the $\sim$ 25,000 episodes required for those trained by $r_n^{(1)}$. Similarly, the learning processes corresponding to the agents trained by further truncated signals $r_n^{(3)}$ and $r_n^{(4)}$, converge to the full performance rate after $\sim$ 260,000 and 270,000 episodes, respectively (Fig. 6.11). We once again highlight that using an appropriately devised reward signal will significantly facilitate the learning process (see e.g. Fig. 6.11). In fact, as the reward signal (received by the agents) becomes less informative about the ultimate objective, the required number of training episodes (i.e. the computational cost) for the agents to learn optimal behavior policy grows substantially. As an extreme case, let us consider $r_n^{(5)}$, where all components are eliminated from the originally proposed reward

signal, keeping only the negative nature of the feedback. This means that throughout the learning process agents will merely receive a constant reward of '-1' after any action they take, regardless of the outcome. Swimming agents trained by this naively defined feedback on performance, still can potentially learn how to realize desired active cloaks – as it is the only way for them to stop accumulating more negative rewards. However, the process is cumbersome, reaching to only $\sim 20\%$ success rate after 300,000 training episodes (Fig. 6.11), and requires a few million to achieve the full performance.

6.5.3 Alternative Control Strategies

In section 6.4 of this chapter, we presented a systematic methodology to equip cloaking agents with an adaptive decision-making intelligence in response to flow-mediated interactions. We then described how such an artificial intelligence encodes consequences of each possible action (at any given state) into the learned behavior policy (π^*), based on which optimal actions are taken. This makes the agents inherently aware of the shortest non-invasive paths (from anywhere in the state space) toward positioning themselves into a desired cloaking arrangement around an arbitrarily moving intruder.

Alternatively, one may use an active optimal control strategy to guide the deployed swimming micro-robots (i.e. the cloaking agents) toward the desired arrangement. Here, as a benchmark, we implement a model predictive control strategy [143] based on the same state-action space (s_n, a_n) used in the proposed reinforcement learning algorithm (see section 6.4 for details). In this alternative approach, the swimming agents are actively controlled to target the optimal double-agent cloaking configuration (already identified in section 6.3). In doing so, the controlled agents are provided (throughout the process) with a feedback signal informing them about their current state, and then use a predictive model (that incorporates agent/intruder hydrodynamic interactions) to take the best action at any given state. We compare the performance of this alternative agent-control strategy on a benchmark test case (illustrated in Fig. 6.12), against the smart agents equipped (via reinforcement learning) with the optimal behavior policy (π^*). Although efficacy of the implemented active control approach suffers from nonlinearly varying hydrodynamic loads (due to the presence of long-ranged flow-mediated interactions), the controlled agents are able to correct the induced deviations and eventually form the desired cloak (see Fig. 6.12-a).

It is also worth noting that in a model predictive control strategy, swimming actions (i.e. the control inputs) at each state, are determined by solving an on-line optimization problem. Therefore, the main drawback of such an alternative approach is the potentially exorbitant on-line computational requirement [144]. Instead in the proposed reinforcement learning algorithm, the cloaking agents experientially learn optimal action policies through an *off-line* trial-and-error training process (see e.g. Figs. 6.4 and 6.5). The learned behavior policy (encoded in the so-called Q-matrix) then serves as the agents' decision-making intelligence, and the control actions are implemented on-line in the form of a simple table look-up (see section 6.4 for details). To give an example, for the model predictive control implemented on the simple test case presented in Fig. 6.12, the on-line computation in taking each single

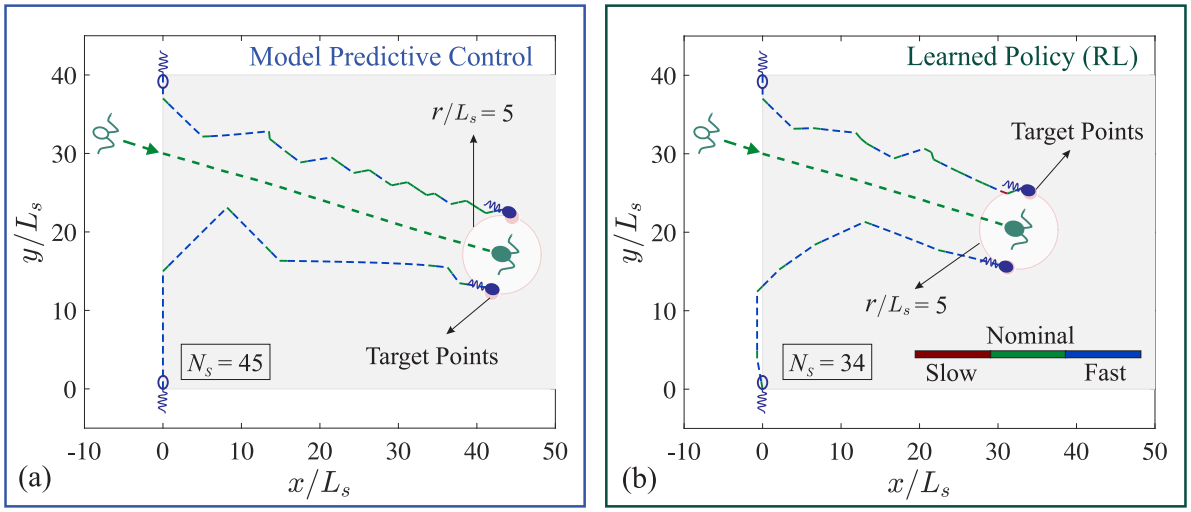

Figure 6.12: Performance of the implemented model predictive control (as an alternative agent-control strategy) is compared (on a benchmark test case) to the performance of smart agents equipped with the optimal behavior policy (π^*) obtained through the proposed reinforcement learning-based algorithm. Similar to the sample test cases presented in Fig. 6.5, the testing episode starts with an intruder entering a guarded region (shaded in gray) from (toward) a random position (direction), while the cloaking agents are initially positioned on the sides of entrance. Throughout the process, cloaking agents in panel (a) are actively controlled through a model predictive control scheme that targets the pre-identified optimal double-agent cloaking configuration. On the other hand, the agents deployed in panel (b) use their own adaptive decision-making intelligence encoded in the learned optimal policy (π^*), to realize the desired cloak. In both panels, the intruder (here, a puller shown in green) and the cloaking agents (pushers shown in blue) are represented both at their initial and final positions, with stripe and solid schematics, respectively. Trajectories of the swimmers are shown in each panel by dashed lines (color-coded based on the instantaneous swimming speed). The number of swimming actions (or equivalently, the number of state-changes N_s) taken to form the desired cloaks around the intruder in each case is reported within panels.

action required $\sim 4.47 \times 10^{-1}$ s on a personal computer, whereas taking the optimal action based on the learned policy (i.e. through the table look-up) requires only $\sim 6.76 \times 10^{-5}$ s on the same machine (2019 Lenovo ThinkPad T470p; Intel Core i7-7700 HQ CPU @ 2.80 GHz; 8.00 GB RAM). It is, however, to be mentioned that in principle, using the exact same state-action space as for the learning strategy, one can also pre-compute the optimal actions (as a function of initial state) in the predictive control scheme to make a look-up table [145].

6.5.4 Incorporation of the Swimmers' Realistic Geometry

In this section, we further explore effectiveness of the presented approach for cases where realistic geometry of the micro-swimmers is simulated in a three-dimensional (3D) setting. Common approaches to provide precise description of swimmers' hydrodynamics in such settings include the boundary element method [e.g. 146, 147] and the regularized Stokeslets approach [e.g. 148, 149]. Formulation of the boundary element method (BEM) for Stokes flows is based on integrating a distribution of Stokeslets over the surface of each swimmer (see e.g. [150, 151]). As a result, the computational costs associated with this mesh-based method is relatively high, and can drastically increase with grid refinement [146]. The regularized stokeslet method, on the other hand, can be a mesh-free approach for discretizing the boundary integral equations. A nearest-neighbor-based discretization of this approach (recently proposed by [152], has been shown to considerably reduce the computational cost without compromising the accuracy. Therefore, here we use this technique (as outlined by [153] to discretize the regularized Stokeslet boundary integral equations, and accurately model 3D geometry of the intruder as well as our swimming agents.

Performance of the learned behavior policy (as an agent-control strategy to realize desired cloaking arrangements around arbitrarily moving intruders) is then evaluated for cases where the swimmers' hydrodynamics is simulated using the described high-accuracy method (see Fig. 6.13). In particular, we adapt the simulation framework and the open-source code provided by [153] to accurately model realistic 3D geometry of the intruder and cloaking agents. Here, for example, 3D models of self-propelled sperm cells (which propel based on the flexible-oar mechanism) are used to represent our pusher-type swimming agents. The puller-type intruder is also simulated using a 3D model bi-flagellate algae, in consistent with other sample tests presented throughout this chapter. Detailed (3D) geometry of the deployed model micro-swimmers and their beating patterns (i.e. swimming strokes) are also presented in panels (b)-(c) of Fig. 6.13. Our numerical experiments further confirm that through implementing the sequence of actions provided by the learned policy (π^*), the swimming agents (simulated with realistic 3D geometries) can indeed form any desired cloaking arrangements (see e.g. Fig. 6.13) around an arbitrarily moving intruder (which is also simulated with its realistic 3D geometry). In doing so, the swimming agents use an action space ($\mathcal{A}$) similar to the one described in section 6.4. Particularly, they can instantly turn to their right ($\theta \leftarrow \theta + \delta\theta$) or left ($\theta \leftarrow \theta - \delta\theta$) with different choices of angle $\delta\theta \in \{\pi/18, \pi/4, \pi/2\}$. Note that such actions are chosen (with frequency τ_r^{-1}) by the agents,

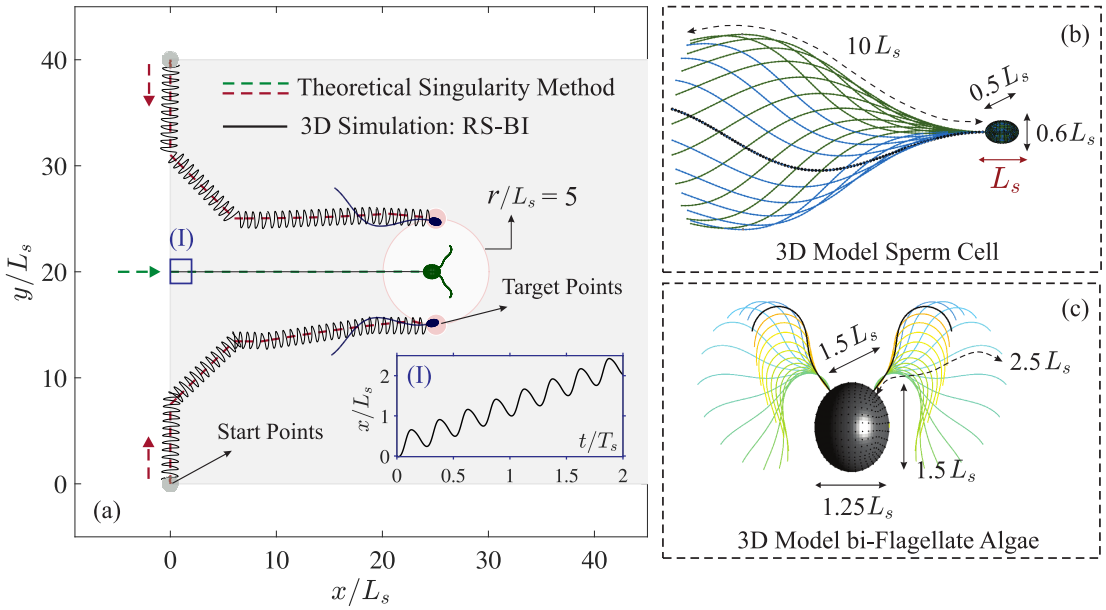

Figure 6.13: (a) Applicability of the learned behavior policy for agent-control, when the simulation of hydrodynamics incorporates the swimmers' realistic 3D geometry. Specifically, the swimmers' hydrodynamics and their flow-mediated interactions are modeled using a high-accuracy 3D simulation framework (proposed by Gallagher and Smith [153]) based on discretization of the regularized Stokeslets in boundary integral (RS-BI) formulation (solid trajectories). For the sake of comparison, we also plot (with dashed line) the trajectories presented in Fig. 6.5(e) associated with the test case conducted using ideal cloaking agents, modeled through the theoretical singularity method (as described in section 6.3). In both cases, the cloaking agents are equipped with the optimal behavior policy (π^*), obtained through the consecutive learning episodes demonstrated in Figs. 6.4 and 6.5. Here, the desired arrangement for the deployed agents is to symmetrically position themselves on the sides of intruder (with a separation distance $r_0/L_s = 5$) that is properly achieved in both cases. The assigned target point for each agent is marked (in pink) at the final stages. Note that the RS-BI approach precisely models realistic geometry of the intruder and our swimming agents, as demonstrated in their final positions in panel (a). Here, as a benchmark, 3D models of self-propelled sperm cells (which propel based on the flexible-oar mechanism) are used to represent our pusher-type swimming agents. The 3D geometry of these model sperm cells and their beating pattern (i.e. swimming stroke) are presented in panel (b). The puller-type intruder, on the other hand, is simulated using a 3D model bi-flagellate algae, for which the swimming trajectory is also monitored over time, throughout the presented window in inset (I) of panel (a). The 3D geometry of the deployed bi-flagellate swimming cell along with its beating pattern is presented in panel (c).

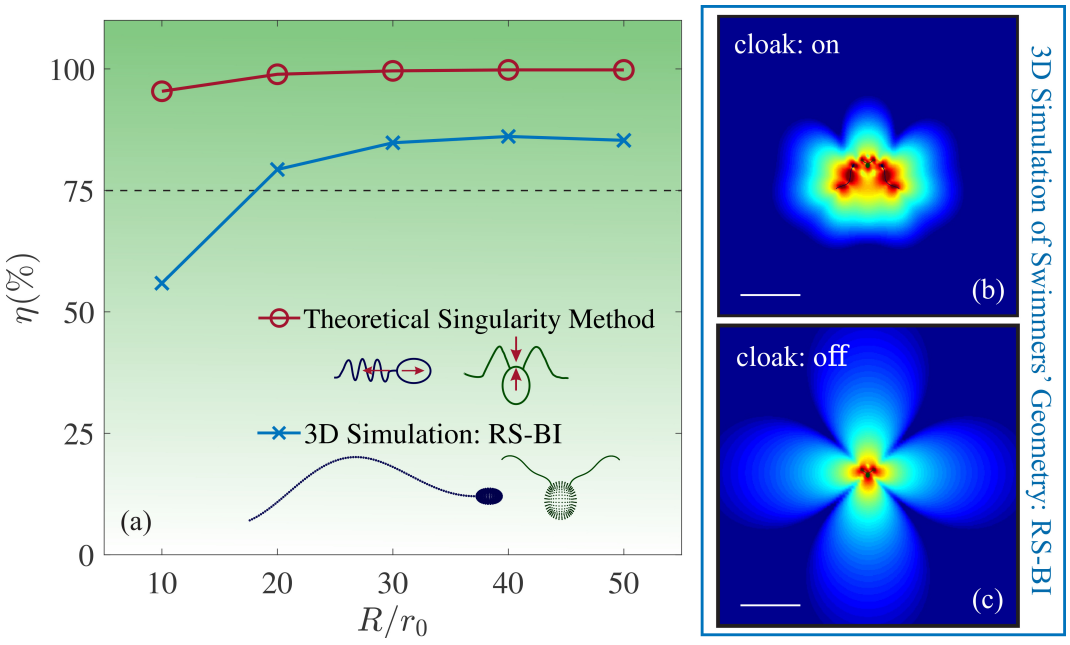

Figure 6.14: Effectiveness of the double-agent symmetric cloak formed at final stage of the numerical experiment (presented in Fig. 6.13) that incorporates the swimmers' realistic geometry by simulating hydrodynamics using a high-accuracy 3D framework based on discretization of the regularized Stokeslets in boundary integral (RS-BI) formulation. In panel (a) we compare the efficiency (η, quantified as a function of R/r_0) of the realized cloak (shown in red with 'o' markers) to that associated with an ideal set of cloaking agents (shown in blue with 'x' markers) modeled through the theoretical singularity method as described in section 6.3 of this chapter. Inset also compares the model force-dipoles used in the singularity method, against the 3D realistic geometries used in the RS-BI simulation. In panel (b), we visualize performance of the cloak formed using the latter approach, where a realistic geometry of the intruder and cloaking agents are incorporated into the simulation of hydrodynamics. The color shading represents the magnitude of induced disturbing flows. For the sake of comparison, we also visualize (via color shading) the magnitude of fluid disturbances induced by an isolated intruder (c), when no cloaking agents are deployed (i.e. cloak: off). The presented snapshots correspond to the final stage of numerical experiment demonstrated in Fig. 6.13, and the scale bars denote $20L_s$.

based on the optimal behavior policy (π^*) obtained through consecutive learning episodes demonstrated in Figs. 6.4 and 6.5.

Effectiveness of the implemented cloak is then evaluated (see Fig. 6.14) for the benchmark numerical experiment presented in Fig. 6.13. For the realized non-invasive cloak (in which the hydrodynamics are simulated by incorporating the swimmers' realistic geometry), our results reveal an efficiency (η) that reaches beyond 80% and 85% at ranges $R/r_0 \geq 20$ and 30,

respectively (Fig. 6.14). This is owing to the fact that (as discussed in section 6.2) far-field of the disturbing flow induced by a micro-swimmer, can be well-described by the flow of a force dipole. The difference (observed in Fig. 6.14) between far-field cloaking efficiencies of the presented test case (conducted using the RS-BI method) compared to those predicted in section 6.3 (using the theoretical singularity method) is due to the following fact. In computing the cloaking efficiencies presented in section 6.3, we use a set of artificial agents (i.e. swimming micro-robots) carefully designed to provide an ideally canceling set of dipole strengths for the specific intruder of interest (that is the $+\mathscr{D}/2$ dipole strength for each of the pusher-type cloaking agents, where $-\mathscr{D}$ is the dipole strength of the puller-type intruder). Therefore, the results associated with the theoretical singularity method, portray the theoretical limit for efficiencies that can be achieved using *optimally designed* cloaking agents. Whereas, here we implement the RS-BI method to demonstrate an active cloaking test case using a set of micro-swimmers with geometric characteristics of swimming micro-organisms. In fact, 3D models of self-propelled sperm cells (with their realistic geometry as opposed to being carefully designed) are used to represent our pusher-type swimming agents, and a 3D model of bi-flagellate algae (with its realistic geometry) is used to represent the puller-type intruder (Fig. 12). As a result, the associated dipole strengths (for the latter case) do not precisely cancel out, and thus the cloaking efficiency is expected to be less than those predicted (in section 6.3) for an ideal set of cloaking agents (see the comparison in Fig. 6.14). Nevertheless, in principle, by changing details of the swimmers' geometry (and/or swimming stroke), one can tune the force-dipoles representing far-field of their induced disturbances. Therefore, when using the sperm-like swimming micro-robots to cloak a specific intruder of interest, further optimization of their shape (and swimming stroke) can provide a perfectly canceling set of dipole strengths. This, however, is beyond the scope of this chapter and deserves an independent investigation.

In the end, we note that the implemented singularity method is based on modeling the disturbing flow induced by each micro-swimmer as the flow of a force dipole with *fixed* strength/direction. As discussed in section 6.2, this simple model has been widely used in the literature [89], and its validity is particularly confirmed (through experimental measurements) for modeling the flow induced by *E. coli* bacteria [90], as well as the time-averaged flow induced by *C. reinhardtii* algae [60]. However, it is worth mentioning that swimmers may induce time-varying flows characterized by a time-dependent dipole strength. Examples include the swimming cells simulated in the presented numerical experiment (Fig. 6.13) – i.e. the bi-flagellate algae and spermatozoa, which transition between pusher- and puller-type dipoles over the course of their beat period. In this section, we demonstrated (Figs. 6.13-6.14) the possibility of using such swimming agents (with time-dependent flow fields) to form a desired arrangement and cloak an arbitrarily moving intruder (with a different time-varying disturbing flow). To optimally conceal an intruder (over time) in such settings, however, the cloaking agents must additionally learn how to adjust their swimming gates (and/or beating patterns) in response to the time-varying flow induced by the intruder. This, indeed, can be an interesting topic for future work.

6.6 Concluding Remarks

In this chapter, a rigorous approach was presented to actively cloak swimming objects in the Stokes regime using a flock of micro-swimmers equipped with adaptive decision-making intelligence. Through a reinforcement learning algorithm, our cloaking agents experientially learn optimal adaptive behavior policy in the presence of non-linear flow-mediated interactions. This artificial intelligence enables them to dynamically adjust their swimming actions, so as to optimally form, and robustly retain, desired cloaking arrangements around any arbitrarily moving object. In doing so, our *smart* agents optimally cooperate, such that their overall generated flows not only cancel out the cloaked object's induced fluid disturbances, but also do not disturb it from its original path. Therefore, the presented active cloaking approach is also *non-invasive* to the subject's motion. We then generalized our methodology, and demonstrated that a cooperative flock of well-adapted cloaking agents can be readily used in a crowded environment to actively cloak any number of arbitrary intruders.

This work provides a clear road-map toward realizing hydrodynamic invisibility cloaks for externally or internally controlled artificial swimming micro-robots [e.g. 71]. This is significant in non-invasive intrusion of swimming micro-robots with a broad range of biomedical applications [see e.g. 18]. Moreover, our findings demonstrate the great potential of reinforcement learning in paving the path toward engineering of smart micro-swimmers capable of accomplishing a new class of group-objectives. We, therefore, hope that this study will spur further research on this field at the intersection of fluid mechanics and artificial intelligence.

Acknowledgments

This work is supported by the National Science Foundation grant CMMI-1562871.

Chapter 7

Conclusions

To summarize, in this dissertation we addressed various aspects of realizing a three-dimensional (3D) controlled flock of swimming micro-robots that operate in, and cooperatively influence, viscous fluid environments. We then demonstrated how to equip each individual agent with an adaptive decision-making intelligence, so as to enable the flock of these artificially intelligent swimming micro-robots to achieve various objectives in the presence of long-range flow-mediated interactions. Specific contribution of each chapter is as follows.

In chapter 2, we reported the design, fabrication, control strategy, and experimental testing of a swimming robot with full 3D maneuverability in viscous environments. This low-Reynolds-number swimmer (called Quadroar) is composed of four independently controlled rotary paddles (hence the name, Quadru oars) and a linear actuator on its chassis which is capable of reciprocal expansion/contraction. These five degrees of freedom enable the Quadroar to swim along forward/transverse straight lines and perform full three-dimensional reorientation maneuvers. A hierarchical supervisory control scheme was also designed and implemented on the swimmer to perform primary modes of swimming maneuvers. This highly-controllable artificial low-Reynolds swimmer can be used either as: (i) a swimming micro-robot for various biomedical purposes such as targeted drug delivery and autonomous surgery [18]; or (ii) a mm-scale swimming robot performing inspection, monitoring and remediation missions in highly viscous fluid environments such as oil reservoirs [20].

In chapter 3, we used this artificial swimming micro-robot as a model to unveil orbital topologies of interacting micro-swimmers. Depending on the initial conditions of the swimmers, diverse families of attractors including dynamical equilibria, bound orbits, braids, and pursuit-evasion games were reported. In particular, we revealed that through flow-mediated interaction, two micro-swimmers in Stokes regime can trap each other into: (i) a dynamical equilibrium state at which they both remain stagnant indefinitely, or (ii) a bound orbit in which they revolve about each other indefinitely. We also observed the hydrodynamic slingshot effect: a system of two hydrodynamically interacting micro-swimmers moving along braids can boost each other's swimming speed and advance in space faster than non-interacting swimmers. Our findings suggest existence of complex collective behaviors of micro-swimmers, ranging from equilibrium to rapidly streaming states.

In chapter 4, we reported a systematic investigation on the near-wall behavior of a model micro-swimmer with flow characteristics of bi-flagellate algae. Specifically, we showed that inducing an oscillatory flow field with anterior, side, and posterior vortices, can be a sufficient tool for micro-swimmers to sense and escape solid boundaries. Our finding provides a new insight into the cell-surface scattering process, and may pave the path for new techniques in controlling biological migration, for which a broad range of potential applications can be sought – including diagnostics [50], drug delivery [69], and bio-remediation [70].

In chapter 5, we revealed that micro-swimmers can form a stealth swarm through a controlled cooperation in suppressing one another's disturbing flows. Specifically, our results unveiled the existence of concealed arrangements, which can stifle the swarm's hydrodynamic signature (and thus, shrink its detection region) by more than 99% (or 50%) for three-dimensional (or planar) movements. We then demonstrated how such a concealed swarm can actively gather around a desired spot, point toward a target, or track a prescribed trajectory in space. The systematic study presented in this chapter provides a road map to optimally control/lead a swarm of interacting swimming micro-robots in stealth versus fast modes. This paves the path for non-invasive intrusion of bio-medical swimming micro-robots with a broad range of potential applications [18]. The presented findings also provide insights into dynamics of prey-predator systems. For instance, stifling the induced disturbances (via forming a concealed swarm) may help an active swarm of prey swimmers gathered around a favorite spot (e.g. a nutrient source) to lower their detectability and thus the predation risk. Stealthy movements by quenching flow signatures induced by a traveling flock, on the other hand, can help a flock of predators to remain stealth while attacking a target prey swarm. Therefore, stealthy movements and swarming in concealed modes, can potentially have a significant impact on trophic transfer rates among a broad range of aquatic organisms.

In chapter 6, a systematic approach was presented to equip swimming micro-robots with an adaptive decision-making intelligence in response to long-range flow-mediated interactions. Flocks of these artificially intelligent micro-swimmers were then deployed to actively cloak swimming objects within an unforeseen crowded environment. In particular, we demonstrated how a reinforcement learning algorithm can be used to let the agents experientially learn an optimal adaptive behavior policy in the presence of non-linear hydrodynamic interactions. This artificial intelligence enables them to dynamically adjust their swimming actions, so as to optimally form and robustly retain, desired cloaking arrangements around any arbitrarily moving object. In doing so, our *smart* agents optimally cooperate, such that their overall generated flows not only cancel out the cloaked object's induced fluid disturbances, but also do not disturb it from its original path. Therefore, the presented active cloaking approach is also non-invasive to the cloaked object's motion. We then generalized our methodology, and demonstrated that a cooperative flock of well-trained swimming micro-robots can be readily used in a crowded environment to actively cloak any number of arbitrary intruders. This work provides a clear road-map toward realizing hydrodynamic invisibility cloaks for/using externally or internally controlled artificial swimming micro-robots. This is a significant step toward non-invasive intrusion of swimming micro-robots with a broad range of biomedical applications [see e.g. 18]. Moreover, our findings demon-

strate the great potential of reinforcement learning in paving the path toward engineering of smart micro-swimmers capable of accomplishing a new class of group-objectives. We, therefore, hope that the presented study will spur further research on this field at the intersection of fluid mechanics, robotics and artificial intelligence.

Bibliography

[1] Frank Schweitzer, Werner Ebeling, and Benno Tilch. "Statistical mechanics of canonical-dissipative systems and applications to swarm dynamics". In: *Physical Review E* 64.2 (2001), p. 021110.

[2] Maria R D'Orsogna et al. "Self-propelled particles with soft-core interactions: patterns, stability, and collapse". In: *Physical review letters* 96.10 (2006), p. 104302.

[3] Reza Olfati-Saber. "Flocking for multi-agent dynamic systems: Algorithms and theory". In: *IEEE Transactions on automatic control* 51.3 (2006), pp. 401–420.

[4] Michael Rubenstein, Alejandro Cornejo, and Radhika Nagpal. "Programmable self-assembly in a thousand-robot swarm". In: *Science* 345.6198 (2014), pp. 795–799.

[5] John Happel and Howard Brenner. *Low Reynolds number hydrodynamics: with special applications to particulate media*. Vol. 1. Springer Science & Business Media, 2012.

[6] Edward M Purcell. "Life at low Reynolds number". In: *American journal of physics* 45.1 (1977), pp. 3–11.

[7] Ali Najafi and Ramin Golestanian. "Simple swimmer at low Reynolds number: Three linked spheres". In: *Physical Review E* 69.6 (2004), p. 062901.

[8] Li Zhang et al. "Artificial bacterial flagella: Fabrication and magnetic control". In: *Applied Physics Letters* 94.6 (2009), p. 064107.

[9] Soichiro Tottori et al. "Magnetic helical micromachines: fabrication, controlled swimming, and cargo transport". In: *Advanced materials* 24.6 (2012), pp. 811–816.

[10] Mohsen Saadat et al. "The Experimental Realization of an Artificial Low-Reynolds-Number Swimmer with Three-Dimensional Maneuverability". In: *2019 American Control Conference (ACC)*. IEEE. 2019, pp. 4478–4484.

[11] Mehdi Mirzakhanloo, Mir Abbas Jalali, and Mohammad-Reza Alam. "Hydrodynamic Choreographies of Microswimmers". In: *Scientific Reports* 8.1 (2018), p. 3670.

[12] Mehdi Mirzakhanloo and Mohammad-Reza Alam. "Flow characteristics of Chlamydomonas result in purely hydrodynamic scattering". In: *Physical Review E* 98.1 (2018), p. 012603.

[13] Mehdi Mirzakhanloo and Mohammad-Reza Alam. "Stealthy movements and concealed swarms of swimming micro-robots". In: *Physics of Fluids* 32.7 (2020), p. 071901.

[14] Mehdi Mirzakhanloo, Soheil Esmaeilzadeh, and Mohammad-Reza Alam. "Active cloaking in Stokes flows via reinforcement learning". In: *Journal of Fluid Mechanics* 903 (2020), A34.

[15] Mir Abbas Jalali, Mohammad-Reza Alam, and SeyyedHossein Mousavi. "Versatile low-Reynolds-number swimmer with three-dimensional maneuverability". In: *Physical Review E* 90.5 (2014), p. 053006.

[16] Nagatoshi Koumura et al. "Light-driven monodirectional molecular rotor". In: *Nature* 401.6749 (1999), pp. 152–155.

[17] Mariana Medina-Sánchez and Oliver G Schmidt. "Medical microbots need better imaging and control". In: *Nature News* 545.7655 (2017), p. 406.

[18] Bradley J Nelson, Ioannis K Kaliakatsos, and Jake J Abbott. "Microrobots for minimally invasive medicine". In: *Annual review of biomedical engineering* 12 (2010), pp. 55–85.

[19] Mir Abbas Jalali, Atefeh Khoshnood, and Mohammad-Reza Alam. "Microswimmer-induced chaotic mixing". In: *Journal of Fluid Mechanics* 779 (2015), pp. 669–683.

[20] Constantinos Mavroidis and Antoine Ferreira. "Nanorobotics: past, present, and future". In: *Nanorobotics*. Springer, 2013, pp. 3–27.

[21] Davide Barcelliy, Alberto Bemporadz, and Giulio Ripaccioliy. "Hierarchical multi-rate control design for constrained linear systems". In: *49th IEEE Conference on Decision and Control (CDC)*. IEEE. 2010, pp. 5216–5221.

[22] Hua-jie Hong et al. "Multi-rate tracking controller analysis and design for target tracking systems". In: *Journal of Central South University* 20.11 (2013), pp. 3049–3056.

[23] Brent C Christner et al. "Ubiquity of biological ice nucleators in snowfall". In: *Science* 319.5867 (2008), pp. 1214–1214.

[24] Maria Mooshammer et al. "Adjustment of microbial nitrogen use efficiency to carbon: nitrogen imbalances regulates soil nitrogen cycling". In: *Nature communications* 5 (2014), p. 3694.

[25] Kenneth J Locey and Jay T Lennon. "Scaling laws predict global microbial diversity". In: *Proceedings of the National Academy of Sciences* 113.21 (2016), pp. 5970–5975.

[26] Jens Elgeti, Roland G Winkler, and Gerhard Gompper. "Physics of microswimmers—single particle motion and collective behavior: a review". In: *Reports on progress in physics* 78.5 (2015), p. 056601.

[27] Henricus H Wensink et al. "Meso-scale turbulence in living fluids". In: *Proceedings of the National Academy of Sciences* 109.36 (2012), pp. 14308–14313.

[28] Jörn Dunkel et al. "Fluid dynamics of bacterial turbulence". In: *Physical review letters* 110.22 (2013), p. 228102.

[29] Umberto Marini Bettolo Marconi and Claudio Maggi. "Towards a statistical mechanical theory of active fluids". In: *Soft matter* 11.45 (2015), pp. 8768–8781.

[30] GP Alexander and JM Yeomans. "Dumb-bell swimmers". In: *EPL (Europhysics Letters)* 83.3 (2008), p. 34006.

[31] Eric Lauga and Denis Bartolo. "No many-scallop theorem: Collective locomotion of reciprocal swimmers". In: *Physical Review E* 78.3 (2008), p. 030901.

[32] Takuji Ishikawa et al. "Hydrodynamic interactions between two swimming bacteria". In: *Biophysical journal* 93.6 (2007), pp. 2217–2225.

[33] Matilda Backholm et al. "Tangling of tethered swimmers: Interactions between two nematodes". In: *Physical review letters* 113.13 (2014), p. 138101.

[34] Takuji Ishikawa and Masateru Hota. "Interaction of two swimming Paramecia". In: *Journal of Experimental Biology* 209.22 (2006), pp. 4452–4463.

[35] Takuji Ishikawa, MP Simmonds, and TJ Pedley. "Hydrodynamic interaction of two swimming model micro-organisms". In: *Journal of Fluid Mechanics* 568 (2006), pp. 119–160.

[36] Gaojin Li, Anca Ostace, and Arezoo M Ardekani. "Hydrodynamic interaction of swimming organisms in an inertial regime". In: *Physical Review E* 94.5 (2016), p. 053104.

[37] Sébastien Michelin and Eric Lauga. "The long-time dynamics of two hydrodynamically-coupled swimming cells". In: *Bulletin of mathematical biology* 72.4 (2010), pp. 973–1005.

[38] MunJu Kim and Thomas R Powers. "Hydrodynamic interactions between rotating helices". In: *Physical review E* 69.6 (2004), p. 061910.

[39] CM Pooley, GP Alexander, and JM Yeomans. "Hydrodynamic interaction between two swimmers at low Reynolds number". In: *Physical review letters* 99.22 (2007), p. 228103.

[40] Gary S Klindt and Benjamin M Friedrich. "Flagellar swimmers oscillate between pusher-and puller-type swimming". In: *Physical Review E* 92.6 (2015), p. 063019.

[41] Jeffrey S Guasto, Karl A Johnson, and Jerry P Gollub. "Oscillatory flows induced by microorganisms swimming in two dimensions". In: *Physical review letters* 105.16 (2010), p. 168102.

[42] Benjamin M Friedrich and Frank Jülicher. "Flagellar synchronization independent of hydrodynamic interactions". In: *Physical Review Letters* 109.13 (2012), p. 138102.

[43] Diego Lopez and Eric Lauga. "Dynamics of swimming bacteria at complex interfaces". In: *Physics of Fluids* 26.7 (2014), pp. 400–412.

[44] Allen T Chwang and T Yao-Tsu Wu. "Hydromechanics of low-Reynolds-number flow. Part 2. Singularity method for Stokes flows". In: *Journal of Fluid Mechanics* 67.4 (1975), pp. 787–815.

[45] Eshel Ben-Jacob, Inon Cohen, and Herbert Levine. "Cooperative self-organization of microorganisms". In: *Advances in Physics* 49.4 (2000), pp. 395–554.

[46] Fernando Peruani et al. "Collective motion and nonequilibrium cluster formation in colonies of gliding bacteria". In: *Physical review letters* 108.9 (2012), p. 098102.

[47] Gareth P Alexander, CM Pooley, and Julia M Yeomans. "Scattering of low-Reynolds-number swimmers". In: *Physical Review E* 78.4 (2008), p. 045302.

[48] Preethi L Chandran and Mohammad RK Mofrad. "Averaged implicit hydrodynamic model of semiflexible filaments". In: *Physical Review E* 81.3 (2010), p. 031920.

[49] Sadao Ota et al. "Brownian motion of tethered nanowires". In: *Physical Review E* 89.5 (2014), p. 053010.

[50] Petr Denissenko et al. "Human spermatozoa migration in microchannels reveals boundary-following navigation". In: *Proceedings of the National Academy of Sciences* 109.21 (2012), pp. 8007–8010.

[51] William M Durham et al. "Division by fluid incision: Biofilm patch development in porous media". In: *Physics of Fluids* 24.9 (2012), p. 091107.

[52] RW Nash et al. "Run-and-tumble particles with hydrodynamics: Sedimentation, trapping, and upstream swimming". In: *Physical review letters* 104.25 (2010), p. 258101.

[53] Gastón Miño et al. "Enhanced diffusion due to active swimmers at a solid surface". In: *Physical review letters* 106.4 (2011), p. 048102.

[54] Mehdi Molaei et al. "Failed escape: solid surfaces prevent tumbling of Escherichia coli". In: *Physical review letters* 113.6 (2014), p. 068103.

[55] Orsolya Sipos et al. "Hydrodynamic trapping of swimming bacteria by convex walls". In: *Physical review letters* 114.25 (2015), p. 258104.

[56] Hao Wu et al. "Amoeboid motion in confined geometry". In: *Physical Review E* 92.5 (2015), p. 050701.

[57] Joost de Graaf et al. "Understanding the onset of oscillatory swimming in microchannels". In: *Soft matter* 12.21 (2016), pp. 4704–4708.

[58] Vasily Kantsler et al. "Ciliary contact interactions dominate surface scattering of swimming eukaryotes". In: *Proceedings of the National Academy of Sciences* 110.4 (2013), pp. 1187–1192.

[59] Matteo Contino et al. "Microalgae scatter off solid surfaces by hydrodynamic and contact forces". In: *Physical review letters* 115.25 (2015), p. 258102.

[60] Knut Drescher et al. "Direct measurement of the flow field around swimming microorganisms". In: *Physical Review Letters* 105.16 (2010), p. 168101.

[61] John Happel and Howard Brenner. *Low Reynolds number hydrodynamics: with special applications to particulate media*. Vol. 1. Springer Science & Business Media, 2012.

[62] J. R. Blake. "A note on the image system for a stokeslet in a no-slip boundary". In: *Mathematical Proceedings of the Cambridge Philosophical Society* 70.2 (1971), pp. 303–310.

[63] JR Blake and AT Chwang. "Fundamental singularities of viscous flow". In: *Journal of Engineering Mathematics* 8.1 (1974), pp. 23–29.

[64] GK Batchelor. "The stress system in a suspension of force-free particles". In: *Journal of fluid mechanics* 41.3 (1970), pp. 545–570.

[65] Erwin Fehlberg. "Classical fifth-, sixth-, seventh-, and eighth-order Runge-Kutta formulas with stepsize control". In: *National Aeronautics and Space Administration* (1968).

[66] Michaël Garcia et al. "Random walk of a swimmer in a low-Reynolds-number medium". In: *Physical Review E* 83.3 (2011), p. 035301.

[67] Hao Wu et al. "Amoeboid swimming in a channel". In: *Soft matter* 12.36 (2016), pp. 7470–7484.

[68] Raymond E Goldstein. "Green algae as model organisms for biological fluid dynamics". In: *Annual review of fluid mechanics* 47 (2015).

[69] Douglas B Weibel et al. "Microoxen: Microorganisms to move microscale loads". In: *Proceedings of the National Academy of Sciences* 102.34 (2005), pp. 11963–11967.

[70] David L Valentine et al. "Propane respiration jump-starts microbial response to a deep oil spill". In: *Science* 330.6001 (2010), pp. 208–211.

[71] Jinxing Li et al. "Micro/nanorobots for biomedicine: Delivery, surgery, sensing, and detoxification". In: *Science Robotics* 2.4 (2017).

[72] Pelin Erkoc et al. "Mobile microrobots for active therapeutic delivery". In: *Advanced Therapeutics* 2.1 (2019), p. 1800064.

[73] Metin Sitti. *Mobile Microrobotics*. MIT Press, 2017.

[74] Jake J Abbott et al. "How should microrobots swim?" In: *The international journal of Robotics Research* 28.11-12 (2009), pp. 1434–1447.

[75] Klaas Bente et al. "Biohybrid and bioinspired magnetic microswimmers". In: *Small* 14.29 (2018), p. 1704374.

[76] Yunus Alapan et al. "Microrobotics and microorganisms: biohybrid autonomous cellular robots". In: *Annual Review of Control, Robotics, and Autonomous Systems* 2 (2019), pp. 205–230.

[77] Christian Peters et al. "Degradable magnetic composites for minimally invasive interventions: Device fabrication, targeted drug delivery, and cytotoxicity tests". In: *Advanced Materials* 28.3 (2016), pp. 533–538.

[78] Salvador Pané et al. "Imaging Technologies for Biomedical Micro-and Nanoswimmers". In: *Advanced Materials Technologies* 4.4 (2019), p. 1800575.

[79] Sylvain Martel et al. "Flagellated magnetotactic bacteria as controlled MRI-trackable propulsion and steering systems for medical nanorobots operating in the human microvasculature". In: *The International journal of robotics research* 28.4 (2009), pp. 571–582.

[80] Michael P Kummer et al. "OctoMag: An electromagnetic system for 5-DOF wireless micromanipulation". In: *IEEE Transactions on Robotics* 26.6 (2010), pp. 1006–1017.

[81] Shuangxi Xie et al. "Controlled regular locomotion of algae cell microrobots". In: *Biomedical microdevices* 18.3 (2016), p. 47.

[82] Tian-Yun Huang et al. "Cooperative manipulation and transport of microobjects using multiple helical microcarriers". In: *Rsc Advances* 4.51 (2014), pp. 26771–26776.

[83] Nicholas C Darnton et al. "On torque and tumbling in swimming Escherichia coli". In: *Journal of bacteriology* 189.5 (2007), pp. 1756–1764.

[84] Ambarish Ghosh and Peer Fischer. "Controlled propulsion of artificial magnetic nanostructured propellers". In: *Nano letters* 9.6 (2009), pp. 2243–2245.

[85] Morgan M Stanton et al. "Biohybrid microtube swimmers driven by single captured bacteria". In: *Small* 13.19 (2017), p. 1603679.

[86] Veronika Magdanz, Samuel Sanchez, and Oliver G Schmidt. "Development of a sperm-flagella driven micro-bio-robot". In: *Advanced Materials* 25.45 (2013), pp. 6581–6588.

[87] Oncay Yasa et al. "Microalga-Powered Microswimmers toward Active Cargo Delivery". In: *Advanced Materials* 30.45 (2018), p. 1804130.

[88] GK Batchelor. "Slender-body theory for particles of arbitrary cross-section in Stokes flow". In: *Journal of Fluid Mechanics* 44.3 (1970), pp. 419–440.

[89] Eric Lauga and Thomas R Powers. "The hydrodynamics of swimming microorganisms". In: *Reports on Progress in Physics* 72.9 (2009), p. 096601.

[90] Knut Drescher et al. "Fluid dynamics and noise in bacterial cell–cell and cell–surface scattering". In: *Proceedings of the National Academy of Sciences* 108.27 (2011), pp. 10940–10945.

[91] Suddhashil Chattopadhyay et al. "Swimming efficiency of bacterium Escherichiacoli". In: *Proceedings of the National Academy of Sciences* 103.37 (2006), pp. 13712–13717.

[92] Somdeb Ghose and R Adhikari. "Irreducible representations of oscillatory and swirling flows in active soft matter". In: *Physical review letters* 112.11 (2014), p. 118102.

[93] Arnold JTM Mathijssen et al. "Upstream swimming in microbiological flows". In: *Physical review letters* 116.2 (2016), p. 028104.

[94] Amin Doostmohammadi, Roman Stocker, and Arezoo M Ardekani. "Low-Reynolds-number swimming at pycnoclines". In: *Proceedings of the National Academy of Sciences* 109.10 (2012), pp. 3856–3861.

[95] Fred Glover, Manuel Laguna, and Rafael Mart´i. "Scatter search and path relinking: Advances and applications". In: *Handbook of metaheuristics*. Springer, 2003, pp. 1–35.

[96] Rafael Mart´i, Manuel Laguna, and Vicente Campos. "Scatter search vs. genetic algorithms". In: *Metaheuristic Optimization via Memory and Evolution*. Springer, 2005, pp. 263–282.

[97] Daniel B Kearns. "A field guide to bacterial swarming motility". In: *Nature Reviews Microbiology* 8.9 (2010), p. 634.

[98] Chengzhi Hu, Salvador Pané, and Bradley J Nelson. "Soft Micro-and Nanorobotics". In: *Annual Review of Control, Robotics, and Autonomous Systems* 1 (2018), pp. 53–75.

[99] Howard C Berg. *E. coli in Motion*. Springer Science & Business Media, 2008.

[100] Marco Polin et al. "Chlamydomonas swims with two "gears" in a eukaryotic version of run-and-tumble locomotion". In: *Science* 325.5939 (2009), pp. 487–490.

[101] Julius Adler. "Chemotaxis in bacteria". In: *Annual review of biochemistry* 44.1 (1975), pp. 341–356.

[102] Benno Liebchen et al. "Viscotaxis: microswimmer navigation in viscosity gradients". In: *Physical review letters* 120.20 (2018), p. 208002.

[103] GE Kaiser and RN Doetsch. "Enhanced translational motion of Leptospira in viscous environments". In: *Nature* 255 (1975), pp. 656–657.

[104] Howard C Berg and Linda Turner. "Movement of microorganisms in viscous environments". In: *Nature* 278.5702 (1979), p. 349.

[105] XN Shen and Paulo E Arratia. "Undulatory swimming in viscoelastic fluids". In: *Physical review letters* 106.20 (2011), p. 208101.

[106] Bin Liu, Thomas R Powers, and Kenneth S Breuer. "Force-free swimming of a model helical flagellum in viscoelastic fluids". In: *Proceedings of the National Academy of Sciences* 108.49 (2011), pp. 19516–19520.

[107] Saverio E Spagnolie, Bin Liu, and Thomas R Powers. "Locomotion of helical bodies in viscoelastic fluids: enhanced swimming at large helical amplitudes". In: *Physical review letters* 111.6 (2013), p. 068101.

[108] Vincent A Martinez et al. "Flagellated bacterial motility in polymer solutions". In: *Proceedings of the National Academy of Sciences* 111.50 (2014), pp. 17771–17776.

[109] James A Sethian. "A fast marching level set method for monotonically advancing fronts". In: *Proceedings of the National Academy of Sciences* 93.4 (1996), pp. 1591–1595.

[110] James Albert Sethian. *Level set methods and fast marching methods: evolving interfaces in computational geometry, fluid mechanics, computer vision, and materials science*. Vol. 3. Cambridge university press, 1999.

[111] Jeannette Yen et al. "Mechanoreception in marine copepods: electrophysiological studies on the first antennae". In: *Journal of Plankton Research* 14.4 (1992), pp. 495–512.

[112] David M Fields and Jeanette Yen. "The escape behavior of marine copepods in response to a quantifiable fluid mechanical disturbance". In: *Journal of Plankton Research* 19.9 (1997), pp. 1289–1304.

[113] David M Fields and Jeanette Yen. "Fluid mechanosensory stimulation of behaviour from a planktonic marine copepod, Euchaeta rimana Bradford". In: *Journal of Plankton Research* 24.8 (2002), pp. 747–755.

[114] Snjezana Rendulic et al. "A predator unmasked: life cycle of Bdellovibrio bacteriovorus from a genomic perspective". In: *Science* 303.5658 (2004), pp. 689–692.

[115] Hossein Jashnsaz et al. "Hydrodynamic hunters". In: *Biophysical journal* 112.6 (2017), pp. 1282–1289.

[116] HL Pécseli and JK Trulsen. "Plankton's perception of signals in a turbulent environment". In: *Advances in Physics: X* 1.1 (2016), pp. 20–34.

[117] T Bullock et al. *Sensory processing in aquatic environments*. Springer Science & Business Media, 2008.

[118] Jeannette Yen et al. "Sensory-motor systems of copepods involved in their escape from suction feeding". In: *Integrative and comparative biology* 55.1 (2015), pp. 121–133.

[119] Lillian J Tuttle et al. "Going with the flow: hydrodynamic cues trigger directed escapes from a stalking predator". In: *Journal of the Royal Society Interface* 16.151 (2019), p. 20180776.

[120] John B Pendry, David Schurig, and David R Smith. "Controlling electromagnetic fields". In: *science* 312.5781 (2006), pp. 1780–1782.

[121] David Schurig et al. "Metamaterial electromagnetic cloak at microwave frequencies". In: *Science* 314.5801 (2006), pp. 977–980.

[122] Mohammad-Reza Alam. "Broadband cloaking in stratified seas". In: *Physical review letters* 108.8 (2012), p. 084502.

[123] Yaroslav A Urzhumov and David R Smith. "Fluid flow control with transformation media". In: *Physical review letters* 107.7 (2011), p. 074501.

[124] Juhyuk Park, Jae Ryoun Youn, and Young Seok Song. "Hydrodynamic Metamaterial Cloak for Drag-Free Flow". In: *Physical Review Letters* 123.7 (2019), p. 074502.

[125] Steven A Cummer et al. "Scattering theory derivation of a 3D acoustic cloaking shell". In: *Physical review letters* 100.2 (2008), p. 024301.

[126] Shu Zhang, Chunguang Xia, and Nicholas Fang. "Broadband acoustic cloak for ultrasound waves". In: *Physical Review Letters* 106.2 (2011), p. 024301.

[127] Shuang Zhang et al. "Cloaking of matter waves". In: *Physical Review Letters* 100.12 (2008), p. 123002.

[128] Sebastien Guenneau, Claude Amra, and Denis Veynante. "Transformation thermodynamics: cloaking and concentrating heat flux". In: *Optics Express* 20.7 (2012), pp. 8207–8218.

[129] Tiemo Bückmann et al. "Mechanical cloak design by direct lattice transformation". In: *Proceedings of the National Academy of Sciences* 112.16 (2015), pp. 4930–4934.

[130] Robert W Boyd and Zhimin Shi. "Optical physics: How to hide in time". In: *Nature* 481.7379 (2012), p. 35.

[131] Sangtae Kim and Seppo J Karrila. *Microhydrodynamics: principles and selected applications*. Courier Corporation, 2013.

[132] Shawn D Ryan et al. "Viscosity of bacterial suspensions: Hydrodynamic interactions and self-induced noise". In: *Physical Review E* 83.5 (2011), p. 050904.

[133] Saverio E Spagnolie and Eric Lauga. "Hydrodynamics of self-propulsion near a boundary: predictions and accuracy of far-field approximations". In: *Journal of Fluid Mechanics* 700 (2012), pp. 105–147.

[134] Shawn D Ryan et al. "A kinetic model for semidilute bacterial suspensions". In: *Multiscale Modeling & Simulation* 11.4 (2013), pp. 1176–1196.

[135] Richard S Sutton and Andrew G Barto. *Reinforcement learning: An introduction*. MIT press, 2018.

[136] Yael Niv, Nathaniel D Daw, and Peter Dayan. "Choice values". In: *Nature neuroscience* 9.8 (2006), p. 987.

[137] Gerald Tesauro. "Temporal difference learning and TD-Gammon". In: *Communications of the ACM* 38.3 (1995), pp. 58–68.

[138] Mattia Gazzola et al. "Learning to school in the presence of hydrodynamic interactions". In: *Journal of Fluid Mechanics* 789 (2016), pp. 726–749.

[139] Gautam Reddy et al. "Learning to soar in turbulent environments". In: *Proceedings of the National Academy of Sciences* 113.33 (2016), E4877–E4884.

[140] Simona Colabrese et al. "Flow navigation by smart microswimmers via reinforcement learning". In: *Physical review letters* 118.15 (2017), p. 158004.

[141] Christopher JCH Watkins and Peter Dayan. "Q-learning". In: *Machine learning* 8.3-4 (1992), pp. 279–292.

[142] Sylvain Martel et al. "MRI-based medical nanorobotic platform for the control of magnetic nanoparticles and flagellated bacteria for target interventions in human capillaries". In: *The International journal of robotics research* 28.9 (2009), pp. 1169–1182.

[143] Eduardo F Camacho and Carlos Bordons Alba. *Model predictive control*. Springer Science & Business Media, 2013.

[144] Damien Ernst et al. "Reinforcement learning versus model predictive control: a comparison on a power system problem". In: *IEEE Transactions on Systems, Man, and Cybernetics, Part B (Cybernetics)* 39.2 (2008), pp. 517–529.

[145] Alberto Bemporad et al. "The explicit linear quadratic regulator for constrained systems". In: *Automatica* 38.1 (2002), pp. 3–20.

[146] Bin Liu, Kenneth S Breuer, and Thomas R Powers. "Helical swimming in Stokes flow using a novel boundary-element method". In: *Physics of Fluids* 25.6 (2013), p. 061902.

[147] Daniela Pimponi et al. "Hydrodynamics of flagellated microswimmers near free-slip interfaces". In: *Journal of Fluid Mechanics* 789 (2016), pp. 514–533.

[148] Ricardo Cortez, Lisa Fauci, and Alexei Medovikov. "The method of regularized Stokeslets in three dimensions: analysis, validation, and application to helical swimming". In: *Physics of Fluids* 17.3 (2005), p. 031504.

[149] Benjamin J Walker et al. "Filament mechanics in a half-space via regularised Stokeslet segments". In: *Journal of Fluid Mechanics* 879 (2019), pp. 808–833.

[150] Constantine Pozrikidis et al. *Boundary integral and singularity methods for linearized viscous flow*. Cambridge University Press, 1992.

[151] Constantine Pozrikidis. *A practical guide to boundary element methods with the software library BEMLIB*. CRC Press, 2002.

[152] David J Smith. "A nearest-neighbour discretisation of the regularized stokeslet boundary integral equation". In: *Journal of Computational Physics* 358 (2018), pp. 88–102.

[153] Meurig T Gallagher and David J Smith. "Meshfree and efficient modeling of swimming cells". In: *Physical Review Fluids* 3.5 (2018), p. 053101.